AN IN VITRO AND IN VIVO EVALUATION OF THE CAPACITY OF THE GENE MMS6 TO BE AN MRI REPORTER GENE

A Dissertation
Presented to
The Academic Faculty

By

Brenda Natalia Robledo

In Partial Fulfillment
Of the Requirements for the Degree
Doctor of Philosophy in
Biomedical Engineering

Georgia Institute of Technology

May 2014

AN IN VITRO AND IN VIVO EVALUATION OF THE CAPACITY OF THE GENE MMS6 TO BE AN MRI REPORTER GENE

Approved by:

Dr. Xiaoping Hu, Ph.D., Advisor
Department of Biomedical Engineering
Georgia Institute of Technology & Emory University

Dr. Hui Mao, Ph.D.
Department of Radiology
Emory University School of Medicine

Dr. Gang Bao, Ph.D.
Department of Biomedical Engineering
Georgia Institute of Technology & Emory University

Dr. Hyunsuk Shim, Ph.D.
Department of Radiology
Emory University School of Medicine

Dr. Shella Keilholz, Ph.D.
Department of Biomedical Engineering
Georgia Institute of Technology & Emory University

Date Approved: February 27, 2014

To my family

ACKNOWLEDGEMENTS

First, I would like to thank my advisor, Dr. Xiaoping Hu, for his support and guidance throughout the years. Also, I would like to thank the members of my dissertation committee for allowing me the opportunity to present my work. I am grateful to any member of the Biomedical Imaging Technology Center (BITC) and the Biomedical Engineering department, past or present, who provided me with quality education, professional assistance, or friendly conversation. I would especially like to thank the few BITC members with whom I worked closely over the years and whose help and advice directly contributed to the work presented in this dissertation: Steven Harris, Xiaoyong Zhang, Katrina Gourdet, Shijun Zhu, and Jason Langley. On a more personal note, I would like to express thanks to Mary Wen, a fellow graduate student, for her friendship and wise counsel. Finally, I would like to give my appreciation to each member of my family for being there for me always.

TABLE OF CONTENTS

ACKNOWLEDGEMENTS ..... **IV**

LIST OF TABLES ..... **VIII**

LIST OF FIGURES ..... **IX**

LIST OF ABBREVIATIONS ..... **XI**

LIST OF SYMBOLS ..... **XIII**

LIST OF UNITS ..... **XVI**

SUMMARY ..... **XVIII**

CHAPTER 1 INTRODUCTION **1**

1.1 Aims **3**

1.1.1 Aim 1: Selection of a gene and creation of positive clones. **3**

1.1.2 Aim 2: *In vitro* MRI and examination of intracellular iron. **5**

1.1.3 Aim 3: Establishment of an animal model and *in vivo* MRI. **5**

1.2 Background **6**

1.2.1 Molecular Imaging and Cell Labeling **6**

1.2.2 Basic Principles of MRI **9**

CHAPTER 2 SELECTION OF A POTENTIAL MRI REPORTER GENE AND CREATION OF STABLE CLONES COMPOSED OF CELLS EXPRESSING THAT GENE **34**

2.1 Background **35**

2.1.1 Molecular Cloning **35**

2.1.2 Reporter Genes **38**

2.1.3 Magnetotactic Bacteria **39**

2.1.4 Transverse and Longitudinal Relaxation **41**

2.2 Approach **46**

2.2.1 Creation of Stable Clones **46**

2.2.2 Selection of a Positive Clone for Further Study **49**

2.3 Methods **53**

2.3.1 Cell Culturing 53
2.3.2 Molecular Cloning 53
2.3.3 Creation of Stable Clones 54
2.3.4 Prussian Blue Staining 56
2.3.5 RT-PCR Analysis 56
2.3.6 Western Blot Analysis 57
2.3.7 *In Vitro* Imaging 57
2.4 Results 59
2.5 Discussion & Conclusion 66
CHAPTER 3 MEASUREMENT OF MRI CONTRAST PRODUCED BY MMS6-POSITIVE CLONES IN VITRO AND CHARACTERIZATION OF CELLULAR IRON UPTAKE 70
3.1 Background 71
3.1.1 The Effects of Iron on Transverse Relaxation 72
3.2 Approach 73
3.2.1 *In Vitro* MRI 73
3.2.2 Prussian Blue Staining 74
3.2.3 Intracellular Iron Measurement 74
3.2.4 Transmission Electron Microscopy 75
3.2.5 Trypan Blue Dye Exclusion Assay 76
3.2.6 MTS Assay 77
3.3 Methods 78
3.3.1 Cell Culturing 78
3.3.2 *In Vitro* MRI at 3 T 78
3.3.3 *In Vitro* MRI at 9.4 T 79
3.3.4 Statistics 80
3.3.5 Prussian Blue Staining 81
3.3.6 Intracellular Iron Measurement 81
3.3.7 Transmission Electron Microscopy 82
3.3.8 Trypan Blue Dye Exclusion Assay 82
3.3.9 MTS Assay 83
3.3.10 Statistics 84

3.4 Results 84

3.5 Discussion & Conclusion 93

CHAPTER 4 ESTABLISHMENT OF TUMORS COMPOSED OF POSITIVE CLONES IN AN ANIMAL MODEL AND MEASUREMENT OF THE MRI CONTRAST PRODUCED BY THE TUMORS 96

4.1 Background 97

4.1.1 Rodents in Biomedical Research 97

4.2 Approach 97

4.2.1 Tumor Animal Model 98

4.2.2 Iron Overload 99

4.2.3 In Vivo MRI 101

4.2.4 *In Vitro* MRI 101

4.2.5 Western Blot Analysis 102

4.2.6 H&E Staining and Prussian Blue Staining 102

4.3 Methods 103

4.3.1 Tumor Animal Model 103

4.3.2 Iron Overload 104

4.3.3 *In Vivo* MRI at 9.4 T 104

4.3.4 *In Vitro* MRI at 9.4 T 105

4.3.5 Western Blot Analysis 106

4.3.6 H&E and Prussian Blue Staining 107

4.3.7 Statistics 107

4.4 Results 108

4.5 Discussion & Conclusion 117

CHAPTER 5 CONCLUSION AND FUTURE DIRECTIONS 121

APPENDIX 128

A.1. Biosafety 128

A.2. Animal Use 128

REFERENCES 129

LIST OF TABLES

Table 1: Systematic selection of an *mms6*-positive 293T clone with the greatest MRI contrast. 63

Table 2: Systematic selection of the *mms6*-positive 9L clone with the greatest MRI contrast. 64

LIST OF FIGURES

Figure 1: **Quantum energy of proton spin states.** 12

Figure 2: **Movement of a magnetic moment vector imperfectly aligned with an external magnetic field.** 18

Figure 3: **Illustration of magnetization vectors in a magnetic field.** 25

Figure 4: **Graphs of the components of magnetization vs. time.** 42

Figure 5: **Transverse decay of the laboratory signal arising from multiple spin echoes.** 44

Figure 6: **Prussian blue staining of transfected cells.** 62

Figure 7: **Analysis of transgene expression in 9L cells and transfected 9L cells.** . 65

Figure 8: **MRI images and corresponding relaxation rates (R_2) of in vitro cells.**. 86

Figure 9: **Relaxation rate (R_2) of cell pellets as a function of the concentration of supplemental iron.**..... 87

Figure 10: **Prussian blue iron staining of 9L and 9L4S whole cells.** 88

Figure 11: **Quantification of iron uptake.** 89

Figure 12: **TEM images of putative iron oxide crystals located in the cytoplasm.**. 90

Figure 13: **Graph depicting cell growth over a period of six days.** 91

Figure 14: **Graph depicting the change in cell viability over a period of six days.**. 92

Figure 15: Graph depicting the effects of iron on cell viability. 93

Figure 16: Relaxation rates (R_2) of flank tumors measured 3 weeks after tumor inoculations with varying numbers of cells. 108

Figure 17: Relaxation rates (R_2) of flank tumors measured over a period of three weeks after tumor inoculations with 2×10^6 cells. 109

Figure 18: Relaxation rates (R_2) of flank tumors in RNU rats measured 2 and 3 weeks after tumor inoculations with 1×10^6 cells. 111

Figure 19: Relaxation rates (R_2) of flank tumors in F344 rats measured 2 and 3 weeks after tumor inoculations with 1×10^6 cells. 112

Figure 20: Analysis of Mms6 expression in 9L4S and 9L tumors. 113

Figure 21: Histological analysis of 9L and 9L4S tumors. 114

Figure 22: Relaxation rates (R_2) of flank tumors in rats that received i.p. iron injections. 115

Figure 23: Relaxation rates (R_2) of cell pellets incubated with media that was replenished every 12 hours. 116

Figure 24: Schematic of molecular cloning and gene expression of an iron-based MRI reporter gene followed by imaging with MRI. 124

LIST OF ABBREVIATIONS

1D	one-dimensional
2D	two-dimensional
3D	three-dimensional
ADC	analog-to-digital converter
BLI	bioluminescence imaging
cDNA	complementary DNA
CEST	chemical exchange saturation transfer
DMEM	Dulbecco's Modified Eagle's Medium
DNA	deoxyribonucleic acid
E. coli	*Escherichia coli*
EDTA	ethylenediaminetetraacetic acid
EHSO	Emory Health and Safety Office
emf	electromotive force
FBS	fetal bovine serum
FOV	field of view
GFP	green fluorescent protein
H&E	hematoxylin–eosin
HCl	hydrochloric acid
HRP	horseradish peroxidase
i.p.	intraperitoneal
i.v.	intravenous
IACUC	Institutional Animal Care and Use Committee
ICP-OES	inductively coupled plasma optical emission spectrometry

LRP	lysine-rich protein
MRI	magnetic resonance imaging
mRNA	messenger RNA
MSME	multi-slice multi-echo
NMR	nuclear magnetic resonance
PBS	phosphate buffered saline
PBST	Tween 20 in PBS
PET	positron emission tomography
rf	radio frequency
s.c.	subcutaneous
RNA	ribonucleic acid
RT-PCR	reverse transcription-polymerase chain reaction
SDS-PAGE	sodium dodecyl sulfate polyacrylamide gel electrophoresis
SPECT	single photon emission computed tomography
SPIO	superparamagnetic iron oxide
TE	echo time
TEM	transmission electron microscopy
TR	repetition time
vs.	versus

LIST OF SYMBOLS

θ, ϕ	angle
ω	angular velocity
$\sim$	approximately
k	Boltzmann constant
°	degree
°C	degree Celsius
°F	degree Fahrenheit
M_0	equilibrium magnetization
$\vec{M}_0$	equilibrium magnetization vector
$\vec{B}$	external magnetic field vector
γ	gyromagnetic ratio
$\vec{\mu}_i$	individual magnetic moment vectors in a small volume
$\vec{\mu}$	magnetic moment vector
$\vec{M}$ or $\vec{M}(\vec{r}, t)$	magnetization vector
S_0	magnitude of the signal at t = 0
$B_{\perp}^{r}$	magnitude of the transverse component of the induced magnetic field per unit current in the receive coil
$-$	negative or minus
$N(\downarrow)$	number of anti-parallel spins
$N(\uparrow)$	number of parallel spins
N	number of samples or subjects in an experiment
N	number of spins
G_x	one-dimensional, linear magnetic field gradient in the *x*-direction

G_y	one-dimensional, linear magnetic field gradient in the y-direction
G_z	one-dimensional, linear magnetic field gradient in the z-direction
%	percent
π	pi
h	Planck's constant
±	plus or minus
$+$	positive or plus
p	p-value
ΔE	quantum energy difference
$\vec{B}_1$	radio frequency field used to create an rf pulse
ω_0	resonance frequency or Larmor frequency
ρ_0	spin density
T_1	spin-lattice or longitudinal relaxation time
T_2	spin-spin or transverse relaxation time
$\vec{B}_0$	static external magnetic field
B_0	static external magnetic field strength
T	temperature
t	time
M_{xy}	transverse magnetization
$\vec{M}_{xy}$ or $\vec{M}_{\perp}$	transverse magnetization vector, equal to $\vec{M}_x + \vec{M}_y$
R_2	transverse relaxation rate
$\hat{x}$	unit vector pointing in the direction of the positive *x*-axis
$\hat{y}$	unit vector pointing in the direction of the positive *y*-axis
$\hat{z}$	unit vector pointing in the direction of the positive *z*-axis
V	volume

V_s	volume of a small sample
M_x	*x*-component of the magnetization
$\vec{M}_x$	*x*-component of the magnetization vector
$\vec{\mu}_y$	*y*-component of the magnetic moment vector
M_y	*y*-component of the magnetization
$\vec{M}_y$	*y*-component of the magnetization vector
$\vec{\mu}_z$	*z*-component of the magnetic moment vector
$\vec{M}_z$ or $\vec{M}_{\|\|}$	*z*-component of the magnetization vector; longitudinal magnetization vector
M_z	*z*-component of the magnetization; longitudinal magnetization

LIST OF UNITS

µg	microgram
µl	microliter
µm	micrometer
µM	micromolar
cm	centimeter
g	gram
hr	hour
Hz	hertz
J	joule
K	kelvin
kb	kilobase
kg	kilogram
M	molar
mg	milligram
MHz	megahertz
min	minute
ml	milliliter
mm	millimeter
ms	millisecond
nm	nanometer
ppm	parts per million
rad	radian
rpm	rotations per minute

s	second
T	tesla
U	units
v/v	volume to volume

SUMMARY

Magnetic resonance imaging (MRI) reporter genes produce MRI signal in response to the molecular environment of the cells in which they are expressed. With an MRI scanner, the signal is detected and used to produce an image of the cells. We hypothesized that the magnetotactic bacterial gene *mms6* has the potential to function as an MRI reporter gene. Magnetotactic bacteria produce magnetic iron oxide crystals in intracellular organelles called magnetosomes. *mms6* encodes an iron-binding, magnetosome membrane protein Mms6, which plays a role in regulating the size and shape of the iron oxide crystals found within the magnetosomes. To test our hypothesis, several mammalian cell lines were transfected with *mms6*, and *mms6*-positive clones were genetically engineered. We then used MRI to image these clones *in vitro*. When the cells were incubated with iron-supplemented culture media, the *mms6*-positive clones produced more MRI image contrast than *mms6*-negative cells. Through a systematic process of elimination, the *mms6*-positive clone that generated the most *in vitro* MRI image contrast was identified. This clone, named 9L4S, was composed of *mms6*-positive rat glioma (9L) cells and was used for intracellular iron studies and *in vivo* imaging. The results of electron microscopy and optical emission spectrometry support the theory that *mms6*-positive clones enhance MRI image contrast due to an increase in intracellular iron. The main objective of this research was to assess the ability of *mms6* to function as an *in vivo* MRI reporter gene, so a flank tumor animal model was created. Without any exogenous iron supplementation, tumors composed of *mms6*-positive cells produced greater negative contrast on an MRI image than *mms6*-negative cells. These results demonstrate that *mms6* can be considered for use in studies requiring an MRI reporter gene.

CHAPTER 1

INTRODUCTION

Magnetic resonance imaging (MRI) is a non-invasive imaging modality that is widely and commonly used in clinical and research settings. In a clinical setting, MRI is most often used by radiologists to image the inside of the human body and by clinicians to diagnose and track the progression of injury and disease in patients. In a research setting, MRI is a powerful piece of equipment used to conduct experiments. Advancements in MRI technology and the development and improvement of MRI-based applications are an ongoing part of MRI research. One such application is called molecular MRI, which is focus of the research presented in this dissertation.

Molecular MRI is the imaging of cellular and molecular events with MRI. One of the current focuses of preclinical research is on examining the limitations and possible applications of molecular MRI. In order for molecular MRI to be effective, it will have to be capable of determining the location, distribution, and long-term viability of an *in vivo* cell population and capable of providing spatial and temporal information on subcellular biological processes such as those involving proteomic, genetic, metabolic, and enzymatic changes (1, 2). In an effort to push the limits of molecular MRI, several methods of labeling cells and tracking them *in vivo* with MRI have been explored—the transfection of cells with an MRI reporter gene is one such method. MRI reporter genes make it possible for cells expressing the gene to enhance their MRI image contrast, or to put it another way, to stand out from the surrounding tissue in an MRI image. An assortment of distinct types of MRI reporter genes have been developed, such as chemical exchange saturation transfer (CEST)-based, iron-based, and enzyme-based

reporter genes (3); however, to date, none of these reporter genes have come into widespread use. In fact, aside from the original studies reporting on the development of novel reporter genes, very few of these studies have led to follow-up research, neither by the group that originally pioneered the work nor by another research group (4). The lack of significant progress is a reflection of the limitations associated with the use of MRI reporter genes (4). Some of disadvantages of using MRI reporter genes are related to the inherent limitations of MRI technology. For example, due to the low sensitivity of MRI, a down-side of using the lysine-rich protein (LRP)-based reporter gene is the need to use high-field magnets for signal detection (5). The low sensitivity of MRI also makes it a requirement for any MRI reporter gene to be able to produce significant amount of MRI signal in order to generate enough image contrast. Some of the limitations are specifically related to the particular design of a specific reporter gene. For instance, iron-based reporter genes require a certain amount of iron to produce contrast—iron that may not be readily available. There are also practical limitations; successfully expressing reporter genes *in vivo* can be very time consuming and technically challenging. As a consequence of these limitations and others not listed here, the development of MRI reporter genes continues to be in its early stages.

Developing an MRI reporter gene is important because MRI reporter genes are powerful tools that could be utilized in a wide variety of applications. Insights into the workings of the human body can be gained by using MRI to visualize and characterize biological processes in living subjects. With MRI reporter genes, biological processes can be studied at the molecular level; so despite all the limitations discussed above, progress in the development of MRI reporter genes will continue as long as the possibility remains that an MRI reporter gene capable of overcoming those limitations can be synthesized or discovered. With a need in the molecular imaging field for a better and novel MRI reporter gene, this dissertation describes our efforts to find such a gene. When we began

our study, we searched for a gene that meets our standards of what constitutes a "good" MRI reporter gene. We agree with Gilad et al. who wrote, "As to what the ideal MRI reporter gene would be, … it would encode endogenous intracellular accumulation of the most sensitive MRI label to date, i.e. superparamagnetic iron oxide (SPIO) particles" (4). With this criterion in mind, we focused our attention on magnetotactic bacterial genes because magnetotactic bacteria have intracellular organelles containing iron oxide. As discussed in more detail in Chapter 2, we ended up selecting the magnetotactic bacterial gene *mms6* for our research. This dissertation delineates the study of the gene *mms6* after it was transfected and expressed in mammalian cells for the purpose of developing and characterizing a new MRI reporter gene.

1.1 Aims

The objective of the research was to assess the possibility of *mms6* functioning as an *in vivo* MRI reporter gene. To make that assessment, *mms6* needed to be expressed *in vivo* to determine whether or not its expression would enhance MRI contrast *in situ*. In order to accomplish this goal, we set out to complete the three aims that are listed below and that are described in greater detail in Chapters 2, 3, and 4 of this dissertation.

1.1.1 Aim 1: Selection of a gene and creation of positive clones.

Because MRI reporter genes encode proteins that are able to enhance MRI contrast, we searched the literature for a gene that encodes a protein that could reasonably be expected to enable cells expressing that protein to take up iron, which is a known negative contrast agent. As mentioned above, we selected a potential MRI reporter gene out of the pool of

genes expressed solely in magnetotactic bacteria. We ended up selecting two genes for analysis, *magA* and *mms6*; the former was thought to encode an iron transport protein and the latter encodes an iron-binding protein. Several mammalian cell lines, which will subsequently be referred to as wild-type cells or negative cells since they do not express the transgene, were transfected with the transgenes and antibiotic resistance genes to create the stable clones. Because we wanted to perform MRI experiments that would last for several weeks, the objective was then to create several stable clones expressing either *magA* or *mms6*, referred to as positive clones. Stable clones are able to express the transfected genes for at least several months. Using standard cell cloning techniques, positive clones were genetically engineered.

After the clones were generated, the main objective was to identify the clone that generated the most *in vitro* MRI contrast because that clone would be the best candidate for *in vivo* MRI studies. Because growing enough cells for imaging is time consuming and requires the use of a lot of media and cell culture dishes, a faster and easier systematic selection process was used to identify the clone that produced the most MRI contrast. We hypothesized that the clone that would produce the most negative contrast would also be the clone with the greatest intracellular iron content, so we used a Prussian blue staining assay, a qualitative technique, as a screen to select the clone with the highest iron content. The clones with the greatest levels of intracellular iron were then tested to confirm that they contained the transgene and that they expressed the protein. Clones that tested positive for the transgene were imaged *in vitro* with MRI at 3 tesla (T). Only *mms6* was found to alter the MRI contrast of the host cell line. As expected, the positive clones generated more MRI contrast than control cells.

1.1.2 Aim 2: *In vitro* MRI and examination of intracellular iron.

Because the creation of a tumor animal model was the main objective of Aim 3, the *in vitro* experiments focused on a positive clone derived from immortalized gliosarcoma cells called 9L cells, a cell line capable of growing tumors *in vivo*. Choosing only from among positive clones derived from 9L cells, the positive clone that generated the most MRI contrast relative to negative cells was named 9L4S. The 9L4S clone was selected for further study. We began by measuring the MRI contrast of the cells at 3 T and 9.4 T. Next, the *mms6*-positive clone 9L4S and its respective wild-type cell line, 9L cells, were sent to a lab that used inductively coupled plasma optical emission spectrometry (ICP-OES), a quantitative technique, to measure their iron contents and to support the results of the Prussian blue staining assay. The results confirmed that the *mms6* positive clone contained significantly more iron and produced more image contrast than the wild-type cells.

1.1.3 Aim 3: Establishment of an animal model and *in vivo* MRI.

Since the *in vitro* results showed that 9L4S cells have faster relaxation rates than 9L cells, we used an animal model to determine whether the 9L4S clone can also enhance contrast *in vivo*. This final objective was important because MRI reporter genes need to be able to create contrast *in vivo* to be versatile research tools. We created a flank tumor model with rats by injecting 9L and 9L4S cells into the flank. As the cells divided, a tumor formed. After 9L and 9L4S tumors were established, the tumors were imaged *in situ* in a small animal 9.4 T MRI scanner. Because 9L4S cells had already been found to have faster relaxation rates than 9L cells *in vitro*, we hypothesized that the relaxation rates of 9L4S tumors would also be faster than the relaxation rates of 9L tumors. The results supported

our hypothesis but only in small tumors. If too many cells were used to inoculate tumors so that the tumor became larger in a shorter amount of time or if too much time was allowed to pass so that the tumors had more time to grow, the opposite of what we expected happened: the relaxation rates of 9L4S tumors were slower than the relaxation rates of 9L tumors. Not only did we expected to see 9L4S tumors produce more contrast, but we also expected them to contain more iron than 9L tumors; so after imaging, the tumors were excised and prepared for histological staining of iron content with Prussian blue. When the 9L4S tumors had faster relaxation rates than 9L tumors, the results indicated that more iron was present in 9L4S tumors than in 9L tumors.

1.2 Background

In this subsection, useful information is provided to enable the reader to obtain a more thorough understanding of the field of molecular imaging and MRI. The knowledge provided here will also allow the reader to better comprehend the basis of the experimental design presented in the subsequent chapters.

1.2.1 Molecular Imaging and Cell Labeling

Molecular imaging is the noninvasive and *in vivo* visualization and characterization of cellular and molecular events involved in biological processes, both biological and pathological (6, 7). A biological process, such as cell division and apoptosis, often involves many types of biomolecules, including genes, ions, enzymes, ligands and receptors, as well as other proteins. Visualization of cellular and molecular events entails visualizing these biomolecules. Any of these molecules may be analyzed, in theory, with

molecular imaging; however, because of the relative novelty of the MRI molecular imaging field as well as the low sensitivity of MRI, in practice, the objective of molecular MRI studies has been not to examine the activity of the biomolecules themselves but to examine the MRI contrast produced by cells. The greater the MRI contrast, the easier it is to visualize and study the cells. To enhance the level of MRI contrast produced *in situ* by a cell type of interest relative to the MRI contrast of the surrounding tissue, the cells can be labeled. For instance, if an oncologist was interested in tracking the metastasization of cancer cells, better visualization of the cancer cells could be achieved if the cells were labeled. In MRI, a label is used to alter the MRI contrast produced by a cell or biomolecule. Although a wide variety of unique methods to label cells have been developed, detection methods of *in vivo* cells can be divided into two major categories depending on their routes of labeling: one is called exogenous labeling and the other is called endogenous labeling, or direct and indirect labeling, respectively. Exogenous labeling is the tagging of cells with a label that originated *ex vivo*. Endogenous labeling is the tagging of cells with a label that originated *in vivo*.

Exogenous labeling often involves the *ex vivo* coupling of a label to a molecule, such as a transfection agent or a positively charged peptide. When the label must be transported into cells in order to function, the molecule facilitates the binding or crossing of the cell membrane. Once the label and the molecule are coupled, the label is ready for transport. To reach the cells of interest, the label must be designed so that when it is administered to a living recipient, the label has the means to reach and bind the target cells (2, 8). For example, a label may be designed to express a specific ligand that is able to bind exclusively to receptors on specific cells; and if that ligand were injected intravenously, it would travel throughout the body until it reached the target cells. When that label reached the target cells, it would bind the cell membranes and would be transported into the target cells. As an alternative to the approach just described, cells may be labeled *in vitro*

instead of *in vivo* by tagging the cells with labels *ex vivo* (2, 8). If that were the case, the pre-labeled cells, instead of the just the label, would be administered to the recipient. Regardless of the specific method used, once labeled, the cells are ready for MRI.

In contrast to the exogenous labeling of cells, endogenous labeling often involves genetic modification of the cells of interest (2). In the case of magnetic resonance imaging, to label them, cells must be transfected with MRI reporter genes. The reporter gene may code for a receptor, a fluorescent protein, an enzyme, or one of several other molecules. When the reporter gene is expressed in a cell, the end result is that the contrast produced by the cell of interest is enhanced such that transfected cells are more easily seen in an MRI image compared to cells that do not express the reporter gene. At the molecular level, the exact chain of events that leads to the production of detectable MRI contrast depends on the specific reporter gene used.

Several different MRI reporter genes have been developed, each with their own unique mode of action. What they all have in common is that once any of the reporter genes are expressed in cells, the gene product, i.e. a protein or functional RNA, either directly produces MRI contrast or sets off a chain of molecular events that result in the activation or accumulation of the label or imaging probe, i.e. the molecule or particle that produces the MRI contrast. Several strategies have been used to enhance the MRI contrast produced by cells. Louie et al. used the enzyme galactosidase to cleave and thus activate a gadolinium-based substrate. Once activated, gadolinium increased the T_1 signal (9). Cohen et al. overexpressed ferritin, an iron-storage gene, in cells to shorten their T_2 relaxation times (10). As a final example, Gilad et al. designed a lysine-rich protein (LRP) reporter, expressed LRP in glioma cells, and then used those LRP-positive cells to establish a brain tumor in a mouse. They then selectively labeled the protons of LRP with radio frequency irradiation. Finally, the labeled protons of the LRP exchange with the

protons of the surrounding water, and due to the process of chemical exchange saturation transfer (CEST), endogenous contrast is produced (5).

1.2.2 Basic Principles of MRI

Several imaging techniques are employed for molecular imaging, including MRI, positron emission tomography (PET), bioluminescence imaging (BLI), fluorescence imaging, single photon emission computed tomography (SPECT), and x-ray and ultrasound based method; and each imaging modality is associated with its own advantages and limitations. MRI, for instance, provides a non-invasive method for deep tissue imaging. MRI can be used to take an image in any orientation in space and to provide two and three dimensional data. Because it provides soft tissue contrast at a reasonably high spatial resolution, it is especially useful in the detection and characterization of solid malignant tumors and other soft tissue pathologies (11). In addition, MRI functions with the use of nonionizing radiation, so it is possible to use MRI to safely track the progression of a disease or treatment over time (12). Along with those advantages, MRI comes with one major limitation: an inherently low sensitivity. Despite this drawback, MRI continues to be one of the most important diagnostic imaging modalities, and that is unlikely to chance considering the advances in MRI technology being made and the increasing number of new clinical applications being developed. Considering that thoroughly covering the subject of MRI is beyond the scope of this text, only a simplified explanation of MRI will be presented here.

1.2.2.1 Nuclear Spin and MRI

All matter in the universe is made up of atoms; and in turn, atoms are composed of three subatomic particles: electrons, protons, and neutrons. These three subatomic particles have characteristic physical properties. In addition to mass and electric charge, these three subatomic particles have an intrinsic physical property called spin. Spin, a quantum-mechanical property, is a type of angular momentum. It comes in multiples of ½, including 0, and can be positive (+) or negative (–). Subatomic particles with non-zero spin also have magnetic properties.

MRI is an imaging modality that takes advantage of the magnetic properties of atomic nuclei to produce images. Only nuclei with non-zero spin have the magnetic property required for MRI. Although workarounds exist, generally speaking, MRI cannot be used to image objects composed of atoms or elements with spin 0. Elements with spin 0 include any element containing an even number of protons and an even number of neutrons, such as ^{16}O and ^{12}C (13). Interestingly, almost every element in the periodic table has an isotope that does have a non-zero spin; however, the natural abundance of each isotope in general and the biological abundance in particular limit the number of nuclei that can be imaged using MRI (14).

MRI of the human body is possible because the human body is composed mostly of fats and water, both of which contain hydrogen atoms. In fact, it turns out that hydrogen makes up approximately 63 percent (%) of all the atoms in the human body (14). Not only is it abundant, hydrogen also has one proton in its nucleus, and that proton has a spin equal to ½. In other words, hydrogen has spin ½. Nuclei with spin produce a nuclear signal that can be detected with an MRI scanner and which can be used to produce an image. From now on, this nuclear signal with be referred to as the nuclear magnetic resonance (NMR) signal. Because the spin of a nucleus produces an NMR signal detectable with an MRI scanner, the presence of hydrogen in large quantities makes the

human body a good candidate for MRI. Even so, MRI cannot be used to image the entire human body because not all tissues are composed of atoms with non-zero spin. As one notable example, MRI cannot be used to image the bones in the human body.

1.2.2.2 Quantum Energy States

So far, it has been established that MRI requires a non-zero spin to produce an MRI image. The key to understanding the relationship between nuclear spin and MRI is knowing that non-zero nuclear spins are able to interact with the external magnetic fields that exist in an MRI scanner. In the discussion that follows, the focus will be on the spin of the hydrogen nucleus, or the proton. Understanding how the proton's spin interacts with external magnetic fields will help elucidate in greater detail how MRI works.

Though magnetic charges do not actually exist, a proton's spin can be better understood if it is likened to a pair of magnetic charges of equal magnitudes but opposite signs. Due to their polarity, the magnetic charges would form a magnetic field. Thus, spin can be pictured as a very small bar magnet with a north pole and a south pole. Normally, spin is randomly oriented in space, and it is free to rotate in any direction. Because it is polarized, when a spin is placed in the magnetic field of a larger, external magnet; the small magnet rotates such that it lines up with the magnetic field. The tiny magnet lines up with the larger magnet in one of two configurations, parallel alignment or anti-parallel alignment (Figure 1) (13). In the parallel alignment, the *north* pole of the smaller magnet faces the same direction as the *north* pole of the larger magnet. When the opposite occurs, the magnets are said to be in an anti-parallel alignment: the *north* pole of the smaller magnet faces the same direction as the *south* pole of the larger magnet. Out of these two possible configurations, a proton contains less energy when its spin aligns itself

parallel to the external field than when its spin aligns itself anti-parallel to the external field. Thus, for nuclei with only two possible quantum spin states, such as protons, spins in parallel alignment are said to be in a low energy state, and spins in an anti-parallel alignment are said to be in a high energy state. When protons are not subject to an external magnetic field, all their spins have only one energy state (Figure 1).

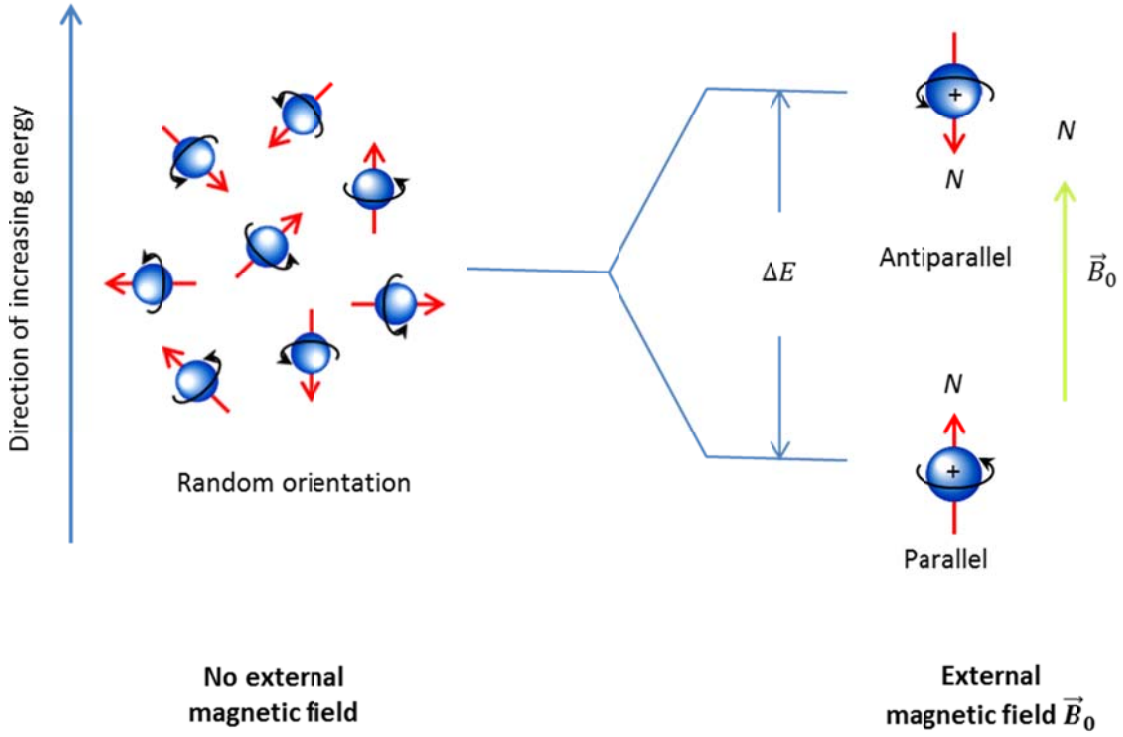

Figure 1: Quantum energy of proton spin states. In the absence of a magnetic field (left), spins move freely in space in random orientation, all of which have the same energy. When a magnetic field ($\vec{B}_0$) is applied (right), the spins line up with the magnetic field either parallel to the field (low energy state) or anti-parallel to the field (high energy state). Blue spheres represent protons. The black arrows indicate the direction in which the proton is spinning. Red arrows point towards to north pole of the magnetic field generated by the spin.

Given a group of proton located in an external magnetic field, not all of the protons will be in the same energy state; some of the protons will have spins in the high energy state, and the remaining protons will have spins in the low energy state (14). Moreover, over time, spins can switch back and forth between energy states. Spin in a low energy state can absorb energy to move into a high energy state, and spin in a high energy state can release energy to move into a low energy state. The amount of energy required by nuclear spins to move between energy states is called the quantum energy difference (ΔE). The relationship between the quantum energy difference of the nuclear spin and the static external magnetic field strength (B_0) is given by the equation:

$$\Delta E = h \frac{\gamma}{2\pi} B_0 \quad (1)$$

where h is Planck's constant (h = ~6.626×10^{-34} J s), and γ is a constant called the gyromagnetic ratio. The unit of energy is the joule (J). The strength of a magnetic field is measured in the unit tesla (T), and the unit of the gyromagnetic ratio is radian/second/tesla (rad/s/T). While it is a constant, the value of the gyromagnetic ratio depends on the nuclei being subject to the external magnetic field. For example, in water, the hydrogen nuclei has a gyromagnetic ratio of approximately 2.68×10^{8} rad/s/T (13). Notice that for a given nucleus, with increasing magnetic field strength, the energy necessary for nuclear spins to change between energy states increases proportionally. Note that Equation (1) and all remaining equations from this chapter are from Reference (13), unless otherwise noted.

1.2.2.3 Nuclear Spin and NMR Signal

So far, it has been established that nuclei have an intrinsic property called spin that can be viewed as a tiny magnet. That tiny magnet can either line up parallel to or anti-parallel to an external magnetic field. Of importance, the strength of the NMR signal detected by an MRI scanner is dependent on the number of spins in each spatial orientation. The exact relationship between the NMR signal and the two possible spin alignments will now be explored.

If $N(\uparrow)$ and $N(\downarrow)$ are the number of spins in a volume parallel to and anti-parallel to the external magnetic field B_0, respectively, then the total number of spins in that volume (N) is given by the following equation:

$$N = N(\uparrow) + N(\downarrow) \tag{2}$$

Furthermore, the spin density (ρ_0) of that volume is defined as the number of spins (N) per unit volume (V):

$$\rho_0 = \frac{N}{V} \tag{3}$$

Given a group of protons inside a homogenous isochromat, or a volume in which all spins inside that volume experience the same external magnetic field, the difference between the number of spins parallel to and anti-parallel to the external magnetic field as a fraction of total number of spins in that volume is given by:

$$\frac{N(\uparrow) - N(\downarrow)}{N} \cong \frac{\gamma h B_0}{4\pi k T} \tag{4}$$

where T is the temperature in kelvin (K), and k is the Boltzmann constant (k = 1.38×10^{-23} J/K). kT is the average thermal energy, a type of energy associated with the temperature of the volume in which the spins are located. Combining Equation (1) with Equation (4), the following equation results:

$$\frac{N(\uparrow) - N(\downarrow)}{N} \cong \frac{\Delta E}{2kT} \tag{5}$$

At human body temperature, the average thermal energy (kT) is millions of times greater than the quantum energy difference (ΔE) (13), which means that the expression on the right hand side of Equation (5) is approximately zero and that Equation (5) reduces to:

$$N(\uparrow) \cong N(\downarrow) \tag{6}$$

According to Equation (6), at human body temperature, the number of spins parallel to an external magnetic field is approximately equal to the number of anti-parallel spins. This fact is significant because the strength of the NMR signal required to form an MRI image is proportional to the relative spin excess, which is the difference between the number of spins in parallel-alignment and the number of spins in antiparallel alignment divided by the total number of spins. The relationship between the relative spin excess and the NMR signal is given by the following equation (14):

$$NMR\ signal \propto \frac{N(\uparrow) - N(\downarrow)}{N} \tag{7}$$

If $N(\uparrow)$ equaled $N(\downarrow)$, then the NMR signal would be zero. Fortunately, the number of spins parallel to the external magnetic field slightly exceeds the number of spins anti-parallel to the external magnetic field at room temperature (14). For example, noting

Equation (4), at 0.3 T and 300 K (~80 ºF), the right hand side of Equation (7) equals ~$1/10^6$. In other words, if the total number of spins equaled 1 million, then $N(\uparrow) - N(\downarrow)$ would equal ~1. Detecting the signal produced by one spin out of a million spins is not as improbable as it sounds because the strength of the NMR signal also depends on the spin density of the sample producing the signal. For instance, N is on the order of 10^{23} spins in just a few grams of body tissue (13).

1.2.2.4 Precession of Nuclear Spin

Although it is not impossible to detect the NMR signal produced by a group of spins at room temperature placed in static (not changing over time) and uniform (not varying in space) external magnetic field, increasing the NMR signal is necessary to produce high quality MRI images. In short, an assortment of magnetic fields is utilized to manipulate nuclear spins such that the spins end up producing a stronger NMR signal. To explain how spins are manipulated to improve NMR signal, it is first necessary to explain how external magnetic fields affect the way spins move.

Spin can be likened to a tiny charge spinning about an axis called the spin axis. Because circulating charges produce an electric current, instead of thinking of spin as a tiny magnet, spin can be thought of as current loop in which the effective electric current is moving around the spin axis (13). As dictated by Ampere's law, an electric current produces a magnetic field; so spin, regardless of whether it is pictured as a tiny spinning charge or a tiny bar magnet, is associated with its own small, magnetic field.

In magnetic resonance imaging, an object is placed in the scanner's magnetic field, which is the same as stating that the nuclei of the atoms that make up that object are placed in an

external magnetic field. The nuclear spins, having a magnetic field of their own, interact with the external magnetic field. To better understand how the two fields interact, it is best to represent external magnetic fields, nuclear spins, and the space in which they interact mathematically. A magnetic field has both a magnitude and a direction; so mathematically, it is represented as a vector quantity. By convention, the magnetic field vector ($\vec{B}$) points from the magnetic field's south pole to its north pole. Because of its magnetic properties, spin is represented by a magnetic dipole moment vector ($\vec{\mu}$), or simply a magnetic moment vector. Using the current loop analogy, imagine that the current loop, whose current revolves around the spin axis, lies entirely in a plane perpendicular to that spin axis. The magnetic moment vector lies perpendicular to and through the center of that loop. In other words, the spin axis and the magnetic moment vector are coincident. To understand in which direction $\vec{\mu}$ points, image the current loop lying in the *x*-*y* plane of a three-dimensional (3D) Cartesian coordinate system with an *x*, *y*, and *z*-axis. If it were viewed from above the positive *z*-axis, then the right-hand rule would dictate that current traveling clockwise would produce a magnetic moment vector pointing in the direction of the positive *z*-axis. Conversely, current traveling counterclockwise would produce a magnetic moment vector pointing in the direction of the negative *z*-axis. Using the bar magnet analogy, just as with the external magnetic field ($\vec{B}$), $\vec{\mu}$ points in the direction of the south pole to the north pole. Since spin and external magnetic fields can be represented mathematically as vectors, the space in which $\vec{B}$ and $\vec{\mu}$ interact can be represented by graphing the vectors in a 3D Cartesian coordinate system.

As discussed previously, when a nuclear spin is placed in an external magnetic field such as the one found in an MRI scanner, the spin orients itself parallel to or anti-parallel to the field. Although the spins do orient themselves with respect to the field, thermal energy prevents nuclear spin from fully aligning with an external magnetic field. Taking

this imperfect alignment into consideration, $\vec{B}$ and $\vec{\mu}$ will now be depicted on a Cartesian coordinate system. As convention dictates, $\vec{\mu}$ points at an angle (θ) to the z-axis, and $\vec{B}$ has a magnitude (B_0) and points in the direction of the positive z-axis (Figure 2a):

$$\vec{B} = B_0\hat{z} \tag{8}$$

In Figure 2, $\vec{\mu}$ lies in the y-z plane, but $\vec{\mu}$ could have been depicted as lying in any plane containing the z-axis.

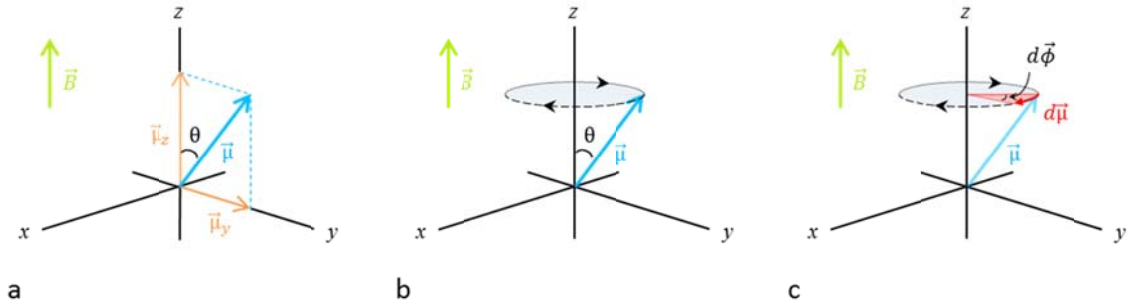

Figure 2: Movement of a magnetic moment vector imperfectly aligned with an external magnetic field. In the presence of an external magnetic field ($\vec{B}$), the magnetic moment vector ($\vec{\mu}$) (a) lies at an angle θ to the z-axis, (b) precesses around the positive z-axis in a clockwise direction, and (c) precesses around the z-axis at a rate of $d\phi/dt$. In (a), $\vec{\mu} = \vec{\mu}_y + \vec{\mu}_z$. In (b) $d\vec{\mu}$ is the very short distance traveled in the very short time dt.

Because an external magnetic field exerts a torque on a magnetic moment vector as described by:

$$\frac{d\vec{\mu}}{dt} = \gamma\vec{\mu} \times \vec{B} \tag{9}$$

when $\vec{B}$ and $\vec{\mu}$ are spatially oriented as shown in Figure 2, the external magnetic field causes the magnetic moment vector to precess around the positive *z*-axis (Figure 2b). Thus, the movement of nuclear spin can be likened to that of a gyroscope (13). If one were to look down from above the positive *z*-axis in the Cartesian coordinate onto the *x*-*y* plane, the magnetic moment vector of a parallel spin (as depicted in Figure 2b, it has a positive *y*-component ($+\vec{\mu}_y$) and a positive *z*-component ($+\vec{\mu}_z$)) would precess clockwise around the positive *z*-axis (Figure 2b). In contrast, the magnetic moment vector of an anti-parallel spin (if it was drawn in Figure 2, it would have a positive *y*-component ($+\vec{\mu}_y$) and a negative *z*-component ($-\vec{\mu}_z$)) would precess around the negative *z*-axis. If one were to look down from above the negative *z*-axis onto the *x*-*y* plane, the magnetic moment vector would precess counterclockwise around the negative *z*-axis.

As the magnetic moment vector precesses, the path taken by the tip of the vector is a circle. In a very short amount of time (dt), the tip travels a very short angular distance around the circle ($d\phi$) (Figure 2c). By definition, the angular velocity (ω) of a magnetic moment vector precessing around the *z*-axis is given by the following equation:

$$\omega \equiv \left|\frac{d\phi}{dt}\right| \tag{10}$$

When placed in an external, static magnetic field of strength B_0, such as the one in the MRI scanner, the precession angular frequency is given by:

$$\omega_0 = \gamma B_0 \tag{11}$$

Recall that γ is a constant called the gyromagnetic ratio and that different nuclei have different gyromagnetic ratios. ω_0 is commonly referred to as the Larmor frequency or the resonance frequency. The dependency of the frequency on the gyromagnetic ratio confirms what is observed in the laboratory: identical nuclei have the same resonance frequency, and distinct nuclei have different resonance frequencies. The unit of frequency is called the hertz (Hz), which is equal to one cycle per second (1/s). In MRI, the resonance frequency ranges from 0.03 to 3×10^4 megahertz (MHz), which are radio frequencies (13). As Equation (11) indicates, the stronger the magnetic field, the faster the precession frequency. For example, a hydrogen proton has a precession frequency of ~128 MHz at 3 T and a precession frequency of ~400 MHz at 9.4 T.

Briefly returning to the topic of quantum energy states, considering Equation (1) and Equation (11), the relationship between the quantum energy difference of the proton spin and the resonance frequency is given by the following equation:

$$\Delta E = \frac{h}{2\pi}\omega_0 \tag{12}$$

In this equation, the unit of resonance frequency (ω_0) is rad/s. As Equation (12) indicates, the energy required by a spin to transition between energy states increases as the resonance frequency increases. In other words, the faster a group of protons are precessing, the larger the difference between the energy of spin parallel to the external magnetic field and the energy of spin anti-parallel to the external magnetic field.

1.2.2.5 Magnetization and NMR Signal

Though a static magnetic field causes nuclear spins to precess, spin movement must be further manipulated to maximize the NMR signal that is used to create MRI images. To briefly elaborate, an MRI image is created using the signal detected by the MRI scanner. The stronger the signal received, the better the image created. The NMR signal is associated with spin movement, so manipulating spin movement affects the NMR signal. Spin movement is altered by changes in the external magnetic field. In an MRI scanner, the external, static field is always turned on, but additional magnetic fields are also used to manipulate spins. During the course of an MRI scan, an assortment of magnetic fields are used and they are not all turned on and off at the same time. When more than one magnetic field is turned on, spins simultaneously feel the combined effects of all the magnetic fields. The first magnetic field to be turned on is the radio frequency (rf) field ($\vec{B}_1$). The use of $\vec{B}_1$ during an MRI scan is usually referred to as an rf pulse because $\vec{B}_1$ is only on for a very short period of time. To explain how the rf pulse is used to manipulate spin movement in order to maximize NMR signal, magnetization vectors need to be introduced.

So far, the precession of nuclear spin in a magnetic field has been described. From now on, the focus will shift to looking at the net movement of a group of nuclear spins, specifically proton spins. To begin, consider an isochromat, which by definition is filled with spins experiencing the same external magnetic field. In practice, instead of a theoretical homogenous isochromat, a voxel refers to a volume element small enough that to a good approximation the external fields are constant over that volume (13). Because each spin in a homogeneous isochromat can be represented as a magnetic moment vector, the sum total of all the individual magnetic moment vectors ($\vec{\mu}_i$) in that small volume (V) is called a magnetization vector ($\vec{M}(\vec{r}, t)$), or $\vec{M}$ for short:

$$\vec{M} = \sum_{\substack{protons \\ in\ V}} \vec{\mu}_i \tag{13}$$

Magnetization, or the magnitude of $\vec{M}$, is the local magnetic moment vector per unit volume. The magnetization is proportional to the relative spin excess, $(N(\uparrow) - N(\downarrow))/\,N$ (14). Considering that $\vec{M}$ is the sum of all the precessing magnetic moment vectors and that parallel spins outnumber anti-parallel spins, $\vec{M}$ also precesses clockwise around an external magnetic field pointing in the direction of the positive *z*-axis at the resonance frequency. Furthermore, considering that each magnetic moment vector is associated with a tiny magnetic field, the magnetization vector is also associated with its own magnetic field.

Notably, the precession of the magnetization vector produces the signal detected in the laboratory during an MRI scan. In short, during an MRI scan, as the magnetization vector precesses in response to the external magnetic field acting on it, its own internal magnetic field moves along with it. As dictated by Faraday's law of induction, that changing magnetic field will induce a current in any nearby coil. That being known, every MRI scanner is fitted with a coil that surrounds the object being scanned. Once current runs through a coil, a voltage is produced, and a device called an analog-to-digital converter (ADC) can be used to measure that voltage. The actual signal detected in the laboratory during an MRI experiment comes from electromotive force (*emf*), i.e. a voltage, induced by the flux changes due to the precession of the magnetization vectors (13). The coil used in MRI scan is called a receive coil because its function is to "receive" the NMR signal of the object being scanned.

Because of the relationship between the magnetization vector and NMR signal, instead of explaining how the rf pulse is used to manipulate the movement of individual spins in order to maximize the NMR signal, the focus will be on explaining how the rf pulse is used to manipulate a group of spins represented by the magnetization vector. To do just that, a 3D Cartesian coordinate system will be used to examine the magnetization vector. To begin, it is useful to separate the magnetization vector into its component parts:

$$\vec{M} = M_x\hat{x} + M_y\hat{y} + M_z\hat{z} \tag{14}$$

Alternatively, the magnetization vector can be represented as the sum of only two vectors:

$$\vec{M} = \vec{M}_{xy} + \vec{M}_z \tag{15}$$

where the transverse vector ($\vec{M}_\perp$ or $\vec{M}_{xy}$) lies in the *x*-*y* plane, and the longitudinal vector ($\vec{M}_{||}$ or $\vec{M}_z$) is parallel to the *z*-axis:

$$\vec{M}_{xy} = \vec{M}_\perp = M_x\hat{x} + M_y\hat{y} \tag{16}$$

$$\vec{M}_z = \vec{M}_{||} = M_z\hat{z} \tag{17}$$

The transverse vector ($\vec{M}_\perp$ or $\vec{M}_{xy}$) is perpendicular to $\vec{B}$, and the longitudinal vector ($\vec{M}_{||}$ or $\vec{M}_z$) is parallel to $\vec{B}$.

At the start of an MRI experiment, an object containing hydrogen nuclei, i.e. protons, is placed in the static external magnetic field of the MRI scanner ($\vec{B}_0$). $\vec{M}$ lines up with the magnetic field and begins to precess clockwise around the positive *z*-axis at the resonance

frequency. While in the static external magnetic field, the magnetization vector is said to be in equilibrium because the precession remains unchanged as long as the external magnetic field remains unchanged. For a proton, the magnetization at the start of an MRI experiment (M_0) is approximately:

$$M_0 \cong \frac{1}{8\pi}\rho_0\frac{\gamma^2 h^2}{kT}B_0 \tag{18}$$

Equation (18) indicates that the equilibrium magnetization of proton is directly proportional to the spin density and the external magnetic field. In terms of the component vectors, $\vec{M}_{xy}$ rotates clockwise in the *x*-*y* plane at the resonance frequency, while $\vec{M}_z$ stays motionless and coincident with the *z*-axis. It turns out that the oscillations of the transverse magnetization vector induce a much greater *emf* in the receive coil than any contribution to the signal due to the longitudinal magnetization vector. In fact, the transverse magnetization's contribution to the signal is so much greater than the longitudinal magnetization's contribution that the contribution of the longitudinal component to the signal will be ignored in the remaining discussion.

To further simplify things, suppose the *x*-axis and *y*-axis are also rotating clockwise at the resonance frequency around the positive *z*-axis. While in a rotating reference frame, $\vec{M}$ does not precess. In terms of the component vectors, $\vec{M}_{xy}$ is motionless and coincident with the *y*-axis, and $\vec{M}_z$ is motionless and coincident with the *z*-axis. For the sake of simplicity, even though thermal energy prevents $\vec{M}$ from perfectly lining with $\vec{B}_0$, in the remaining discussion $\vec{M}_{xy}$ will be assumed to equal zero at equilibrium, which means that $\vec{M} = \vec{M}_z$ as dictated by Equation (15) (Figure 3a).

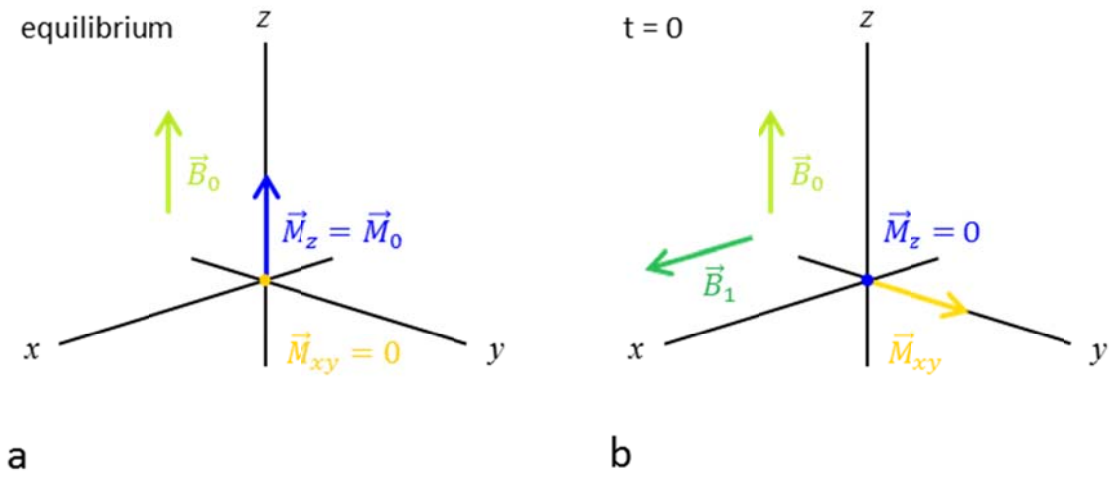

Figure 3: Illustration of magnetization vectors in a magnetic field. The static external magnetic field ($\vec{B}_0$) points in the direction of the positive *z*-axis. (a) The equilibrium magnetization ($\vec{M}_0$) points in the same direction as $\vec{B}_0$. The components of magnetization $\vec{M}_z$ and $\vec{M}_{xy}$ equal $\vec{M}_0$ and 0, respectively. (b) At t = 0, the rf magnetic field ($\vec{B}_1$) rotates the magnetization entirely in the direction of the positive *y*-axis. $\vec{M}_{xy}$ has some initial value ($\vec{M}_{xy}(0)$) and $\vec{M}_z$ = 0. A rotating reference frame is used, so the precession of the transverse magnetization vectors are understood but not pictured.

It has just been established that the magnitude of the transverse magnetization vector is almost zero at equilibrium. Recall that the laboratory signal is mostly due to the *emf* induced by the oscillating transverse magnetization. The strength of the NMR signal decreases as the transverse magnetization vector decreases in magnitude. Thus, when the magnetization vector is in equilibrium, the vector induces almost no *emf* in the receive coil, so the signal can be very difficult if not impossible to detect. During an MRI scan, the signal received in the laboratory can be increased by manipulating the transverse magnetization. One way to increase the strength of the signal is to maximize the magnitude of $\vec{M}_{xy}$ using an rf pulse. An rf pulse is a magnetic field whose direction rotates or oscillates at a radio frequency, specifically at the resonance frequency (15). The word "pulse" refers to the fact that the magnetic field is only turned on for a very short

period of time. Of note, an rf pulse is not a burst of radio waves (16, 17). When hydrogen nuclei (in a sample) are located in a static magnetic field (in an MRI scanner), the oscillation frequency of the oscillating magnetic field (also in the MRI scanner) is matched to the precessional frequency of the spins of those atomic nuclei (13). As you will recall from Equation (11), spins subject to a magnetic field will naturally precess at what is referred to as the resonance frequency or the Larmor frequency. To match the precessional frequency of a group of spins, the frequency of the oscillating magnetic field in the MRI scanner must be set such that it equals the resonance frequency of those spins. The oscillating magnetic field, or the rf pulse, applies torque to the magnetization vector. The main purpose of the rf pulse now becomes clear: it is used to rotate the magnetization vector. A magnetization vector in equilibrium and pointing in the direction of the positive *z*-axis is tipped 90° by the rf pulse, which explains why an rf pulse is also commonly called a 90° or π pulse. Once it is rotated 90°, $\vec{M}$ lies entirely in the *x*-*y* plane which means that the longitudinal component of magnetization is now zero while the transverse component is no longer zero (Figure 3b).

In an MRI experiment, the moment in time when the rf pulse tips the magnetization vector and scanning begins is referred to as t = 0. Since the static external magnetic field is always on, immediately after the rf pulse is turned off, the magnetization vector moves back into its equilibrium position. As the magnetization vector returns to equilibrium, in the laboratory reference frame, i.e. not the rotating reference frame, if one were to look down from about the positive *z*-axis, the transverse magnetization vector would appear to spiral clockwise around the *z*-axis toward the origin. In contrast, in the laboratory reference frame, the longitudinal magnetization vector would not move from its position along the *z*-axis, but it would appear to grow in length from zero to its original equilibrium magnitude.

Following an rf pulse, while the magnetization vector is returning to its equilibrium position, the signal is being received and stored by the MRI scanner. In practice, the signals due to the components of the transverse magnetization ($\vec{M}_x$ and $\vec{M}_y$) are received separately, each by a different coil. Due to the clockwise movement of the transverse magnetization as the magnetization vector precesses back to its equilibrium position, the magnitudes of the $\vec{M}_x$ and $\vec{M}_y$ laboratory signals graphed versus time each look like an oscillating wave. Mathematically, each oscillating wave is composed of simple sine and cosine waves. Although no further details will be given, it is useful to note that because the transverse magnetization vector is rotating in the *x*-*y* plane, the signal can be written as a sum of complex waves.

Given a homogenous sample, homogenous static and rf fields, and no relaxation effects, the amplitude of the signal would be given by the following equation:

$$|signal| = \omega_0 M_0 B_\perp^r V_s \tag{19}$$

where V_s is the volume of the sample. V_s must be small enough to satisfy the given conditions to a good approximation. In this equation, a new magnetic field is introduced. As governed by Ampere's law, when the precession of a magnetization vector induces a voltage in the receive coil, the resulting current flowing in the coil induces another magnetic field. $B_\perp^r$ is the magnitude of the transverse component of the induced magnetic field per unit current. Equation (19) confirms that the signal strength is dependent on the magnetization vector, including its resonance frequency, its initial magnitude, and its *emf*-inducing precession. Under the same conditions as before, Equation (19) can be combined with Equation (11) and Equation (18) to express the magnitude of the signal as follows:

$$|signal| \cong \frac{1}{8\pi}\rho_0 \frac{\gamma^3 h^2}{kT} B_0^2 B_\perp^r V_s \quad (20)$$

Thus, the signal is also directly proportional to the spin density (ρ_0) and the square of the static external magnetic field (B_0^2) (or equivalently the square of the resonance frequency (ω_0^2)). The signal is also indirectly proportional to the temperature of the sample.

1.2.2.6 Magnetic Field Gradients and Creation of an MRI Image

Within a uniform and static magnetic field, all identical nuclei have the same resonance frequency, and distinct nuclei have different resonance frequencies. For example, at the magnetic field strength of 3 T, the resonance frequency of all hydrogen nuclei are the same, but it is different from the resonance frequencies of the sodium (^{23}Na) and phosphorous (^{31}P) nuclei (13). If the strength of the magnetic field changes, so does the resonance frequency of each nucleus. For example, the resonance frequency of the hydrogen nucleus is ~128 MHz at 3 T, but it is ~400 MHz at 9.4 T. Significantly, even when the strength of the magnetic field changes; the hydrogen nucleus, the sodium nucleus, and the phosphorous nucleus continue to have unique resonance frequencies.

So far it has been established that if a group of nuclei, say for example the hydrogen nuclei, was placed in a uniform magnetic field and if the frequency of an rf pulse was matched to the protons' resonance frequency, the nuclei would give off an NMR signal detectable with an MRI scanner. The frequency of the rf pulse used during an MRI scan needs to be adjusted depending on the nuclei being analyzed and the strength of the external magnetic field of the MRI scanner. For example, in a 3 T scanner, the rf pulse would have to be set to 128 MHz in order to image the hydrogen nuclei. Importantly, every nucleus with the same resonance frequency, which in this example would be all the

hydrogen protons, would contribute to the laboratory signal. In other words, at any given time, the laboratory signal is the sum of all the individual NMR signals produced by each magnetization vector precessing in the object being imaged. Furthermore, the laboratory signal itself would have a frequency that was (approximately) the same as the resonance frequency of the hydrogen protons. Since the specific signal of the hydrogen nuclei is known and different from the signal of other nuclei, the collected laboratory signal would indicate that hydrogen was present in the group of nuclei that was scanned.

Significantly, with only the static external magnetic field and the rf pulse, the laboratory signal cannot be used to determine the location of the nuclei within the magnetic field; and without knowing spatial information, it is impossible to create an image. MRI and NMR spectroscopy are both based on the principles of nuclear magnetic resonance (NMR). Although NMR spectroscopy can be used to obtain useful information about the chemical and physical properties of atoms and molecules, it was not until methods were developed to spatially localize the atoms and molecules that the first MRI images could be created. To obtain spatial information in the *x*-, *y*-, and *z*-directions, additional magnetic fields are needed.

For starters, picture an object divided into slices, similar to a sliced loaf of bread. When scanning an object, an MRI scanner images one slice at a time. To select one slice, the rf pulse is used to systematically tip all the magnetization vectors in a slice, one slice at a time. As you will recall, any magnetization vector that is not tipped 90° will not produce an NMR signal and thus will not contribute any information to the laboratory signal. Slice selection occurs by turning on a third magnetic field at the same time that the rf pulse is on. This third magnetic field is called the slice selection gradient. The slice selection gradient is a one-dimensional (1D), linear magnetic field gradient, which means that the strength of its magnetic field increases linearly with respect to its position in

space. For example, the magnetic field strength of a 1D linear magnetic field gradient in the *x*-direction (G_x) increases linearly along the *x*-direction. Considering Equation (11), by linearly varying the strength of the magnetic field in space, the resonance frequencies of the magnetization vectors also linearly vary over that space. This occurs because each magnetization vector experiences a different magnetic field strength and precesses at the resonance frequency corresponding to the magnetic field it is experiencing. The frequency of the rf pulse determines which magnetization vectors are flipped 90°. Any magnetization vectors whose resonance frequencies do not match the frequency of the rf pulse will not be flipped and thus will not contribute any NMR signal to the laboratory signal. In the remaining discussion, assume G_z is the slice selection gradient; in which case, the slice that is selected is parallel to the *x*-*y* plane.

After the rf pulse and slice selection gradient are turned off and a slice has been selected, the signal from the precessing protons needs to be collected in such a way that spatial information of the slice can be ascertained from the NMR signals. Two-dimensional (2D) information is obtained by employing two other 1D linear magnetic field gradients. If G_z is the slice selection gradient, then the other two gradients are G_x and G_y. The first of these two magnetic field gradients is called the phase encoding gradient. As mentioned earlier, the tip of the magnetization vector travels in a circular path. Looking down from above the *z*-axis, the transverse magnetization vector moves just like the hand of a clock. The vector rotates at the resonance frequency, and the angle formed by the vector and some reference axis such as the *y*-axis is called the phase angle. Stated another way, the movement of the magnetization vector is mathematically represented as an oscillating wave and thus has both a frequency and a phase. Immediately before the phase encoding gradient is turned on, all of the magnetization vectors in the slice are precessing at the same resonance frequency and with the same phase. The phase encoding gradient is then turned on. Assuming that the phase encoding gradient is G_y, the resonance frequencies

vary linearly in the *y*-direction. In other words, the magnetization vectors are precessing at increasing speeds along the *y*-direction. When the phase encoding gradient is turned off shortly after it is turned on, the magnetization vectors all return to spinning at the same resonance frequency; however, their phases are no longer the same. Due to the phase encoding gradient, the phases of the magnetization vectors vary in space. Once the phase encoding gradient is turned off, the second of the two linear magnetic field gradients used to obtain spatial information from the 2D slice is turned on. It is called the frequency encoding gradient. Recall that the resonance frequencies of the magnetization vectors increase linearly in a single direction in space when a 1D linear magnetic gradient is turned on. Because the magnetization vectors were already out of phase before it was turned on, the result of applying the frequency encoding gradient is that each magnetization vector in the 2D slice now precesses with a unique combination of frequency and phase. Since each unique combination of frequency and phase corresponds to a particular location within a slice, spatial information is said to be encoded in the frequency and phase of the laboratory signal (18). Fortunately, a mathematical tool called the inverse Fourier transform can decode the spatial information. Recall that the laboratory signal (an oscillating wave) is the mathematical sum of the NMR signals (also an oscillating wave) emitted by all the precessing protons in the field. To obtain spatial information regarding the location of all the protons in the 2D slice, the laboratory signal must be decomposed into its simple, component waves. The inverse Fourier transform is used to deconstruct the data obtained from the laboratory signal into the spatial information necessary to create an image.

When the frequency encoding gradient is on, the signal is "sampled" and the raw data is stored by the MRI scanner. This completes one cycle of an rf pulse sequence. The rf pulse sequence is the sequence in which all the magnetic fields are turned on and off and the signal is sampled by the ADC. Though there are more complicated rf pulse

sequences, the rf pulse sequence that was described in this text began with the rf pulse and the slice selection gradient, was followed by the phase encoding gradient, and ended with the frequency encoding gradient and the ADC.

Because the magnitude of the signal begins to decay over time just as soon as the rf pulse is turned off, the signal can only be sampled for a given period of time. Furthermore, for mathematical reasons, more data is required to create an image than the amount of data that can be collected from one rf pulse sequence. Thus, the rf pulse sequence must be repeated many times, usually 128 or 256 times, in order to collect enough raw data to produce an image of the slice. Each repetition time the sequence in which the magnetic fields are turned on is the same, but the magnitude of the phase encoding gradient is systematically increased in a stepwise fashion.

1.2.2.7 MRI Hardware and Creation of an MRI Image

An MRI scanner consists mainly of a large magnet to generate a strong and static magnetic field, radio frequency (rf) coils to transmit and/or receive magnetic fields, gradient coils to produce variations in the static magnetic field, and a computer to reconstruct the NMR signals into an image (19). Once an object is placed in the bore of the MRI scanner, it lies in the static magnetic field created by the large magnet. The hydrogen nuclei in the object align with that magnetic field, thus becoming temporarily magnetized. The transmit coil generates an rf pulse through the object. After the rf pulse is turned off, the gradient coils create time-varying magnetic field gradients in space in order to manipulate the precession of the hydrogen nuclei. The receive coil collects the signal produced by the precessing hydrogen nuclei. The computer takes the laboratory signal and separates it into its component parts. Thus, the computer is able to calculate

the number of hydrogen nuclei present at each location within the object. Finally, the computer forms a black and white image of the object, where the intensity of a particular location on the image is proportional to the number of hydrogen nuclei located in the corresponding location in the actual 3D object.

As just described, once the ADC has finished sampling the laboratory signal, it generates 2D images of the 3D object. To understand how a 2D MRI image relates to the 3D object, imagine that a very thin cross-section of the object is taken. In the field of MRI, the cross-sections of the object being imaged are called slices. The cross-section has a thickness, so like the object, it too is three-dimensional. Using a grid, the cross-section is then further divided into very small, equally-sized volumes called voxels. Each voxel has the same thickness as that of the cross-section. Using a grid, the image is divided into very small, equally-sized areas called pixels. Pixels are two-dimensional, so they do not have a thickness. By overlaying the two grids, voxels line up with pixels, such that the location of a small volume in the object corresponds to a particular location on the image. To create a black and white image, the magnitude of the signal emitted from one voxel is proportional to the intensity of its corresponding pixel on the image.

Often, MRI images of animals or humans are of slices parallel to the transverse, sagittal, or coronal planes of their bodies. Even so, once an object is placed in the scanner to be imaged, MRI can produce images of slices spatially oriented in any direction. This ability is just one of the advantages of using MRI.

CHAPTER 2

SELECTION OF A POTENTIAL MRI REPORTER GENE AND CREATION OF STABLE CLONES COMPOSED OF CELLS EXPRESSING THAT GENE

In the beginning, we did a literature search to identify a gene that could *potentially* enable cells expressing that gene to produce greater image contrast. We focused our attentions on magnetotactic bacteria, since these bacteria are able to produce intracellular organelles containing iron oxide crystals. Iron affects the magnetization of neighboring atoms thereby creating a change in the NMR signal that can be visualized with MRI. Iron is a known negative contrast agent. When a negative contrast agent is scanned, it appears dark, as opposed to white or bright, on an MRI image. Cells carrying negative contrast agents appear darker on an MRI image as compared to cells that do not contain the negative contrast agent.

Selection of a gene and production of cell clones was of upmost importance because without labeled cells, the experiments described in Chapter 3 and Chapter 4 could not be attempted, much less completed. From amongst genes found in magnetotactic bacteria, two genes, *mms6* and *magA*, were selected for further study. These two genes were selected because we hypothesized that they would encode proteins that would enable cells expressing one or both of the genes to produce negative contrast by increasing intracellular iron stores. Once we selected a potential MRI reporter gene, we transfected cells with the gene and create stable clones. Stable clones allow for the long term imaging of cells. Before continuing, we confirmed that *mms6* and *magA* were expressed and that the Mms6 and MagA proteins were produced in the transfected cells. Because several

clones expressed the genes, a systemic selection process was used to isolate the clone that was best able to take up iron and produce changes in MRI contrast. This selection process included imaging the positive clones *in vitro* with MRI. Imaging the positive clones also served to test the hypothesis that *mms6*-positive and *magA*-positive clones generate MRI contrast and thus have the potential to function as MRI reporter genes *in vivo*.

2.1 Background

The genes *mms6* and *magA* are both native to magnetotactic bacteria; however, we wanted to study an MRI reporter gene in mammalian cells. Molecular cloning is the laboratory technique used to transfer a gene into cells where that gene is not normally expressed. Once the gene has been transfected into the cells, the cells are said to be positive clones or positive cells, while the original host cells, which of course do not express the gene, are referred to as negative cells or wild-type cells. Our first aim was to select a positive clone that was able to produce image contrast. On a T_2-weighted MRI image, image contrast is based on differences in transverse relaxation times. A more detailed discussion on molecular cloning, reporter genes, magnetotactic bacteria, and relaxation times can be found immediately below.

2.1.1 Molecular Cloning

Based on the principles of molecular biology, molecular cloning is a method used to engineer recombinant deoxyribonucleic acid (DNA), to insert the recombinant DNA into a host organism, and to direct its exact replication in that host organism (20). Recombinant DNA is DNA that has been created in the laboratory, either to recreate

DNA molecules that are found naturally in the wild or to piece together new DNA molecules that are not found in nature, out of synthetic DNA pieces or out of a combination of DNA molecules naturally found in more than one organism. For example, a piece of DNA that is naturally found in a bacterium may be cloned into a mammalian or plant cell. The host organism used for molecular cloning is also a type of cell, such as mammalian or bacterial cells. Molecular cloning is possible because cells belonging to different organisms contain DNA with the same chemical structure. Because of the way in which it is engineered, the recombinant DNA molecule, once inside the host cell, is replicated and the progeny of the host organism receives a copy of the recombinant DNA molecule. In this manner, a large population of cells all containing the recombinant DNA can be obtained. Not only is the DNA molecule replicated by the host cell, it is also expressed, in other words, it is transcribed into messenger RNA (ribonucleic acid) and translated into a protein. The resulting protein is called a recombinant protein.

In some cases, the sole purpose of molecular cloning is to multiply the number of recombinants in order to multiply the number or recombinant DNA molecules. In this case, the host organism used is typically a bacterium that can multiply quickly. For example, *E. coli* (*Escherichia coli*), a common bacterium used for molecular cloning, has a doubling time of approximately 16 minutes (min) (21). Once the large batch of cells expressing the recombinant DNA, also known as recombinants, is made, the foreign DNA may be expressed and its protein product may be isolated for study or for use. As an example, insulin and growth factors can be manufactured in this manner (22). Instead of isolating the protein, the recombinant DNA can be extracted from the host organism; and the DNA can be, for instance, commercially sold or can be used for further biological experiments. In the latter case, molecular cloning is again employed but not for the purpose of amplifying the DNA. Instead, one possibility is that the recombinant DNA is

cloned into a cell because, when that piece of DNA is expressed in the cell, the DNA molecule will confer a new trait to its host cell.

Because proteins perform numerous and diverse biological functions, the host organism expressing foreign DNA can, depending on the particular recombinant DNA molecule it expresses, perform one of many novel functions. As the first of three examples, *E. coli* expressing the *inv* gene, which is naturally found in a bacterium called *Yersinia pseudotuberculosis* but not in *E. coli*, induces the invasion of mammalian cell lines expressing β1-integrin, a transmembrane protein located on the cell surfaces of several types of cells (23). The ability to invade mammalian cells could then be further engineered to allow the recombinants to selectively invade and thus kill cancer cells. To prevent pests from damaging crops, plants such as tobacco and tomato have been engineered to make a biological pesticide. The plants gain the ability to make their own insecticide by expressing genes normally found in the bacterium *Bacillus thuringiensis* (24). The green fluorescent protein (GFP) from the jellyfish *Aequorea Victoria* is used as a biomarker in a diverse set of cells and organisms. As a reporter gene, GFP has been used to observe physiological processes, localize subcellular proteins, and monitor gene expression (25).

The trait that is conferred to the recombinant depends not only on what the function of the protein was in its native organism, but also on the endogenous environment of the host organism (26). For instance, the recombinant protein may require other proteins to function correctly, but those other proteins may not be present in the host organism as they were in its native organism. Unlike in its native cell, after it is expressed, a recombinant protein may not function correctly in the host cell because it is not taken to its correct location. As another example, the protein may not function as it did in its native cell because the host organism recognizes the recombinant DNA as foreign and

may take steps to prevent its expression. In the case of synthetic DNA, which is designed in a laboratory and not naturally expressed in any organism, the DNA may not function as expected within the host organism because the biological system in which the synthetic DNA molecule is designed to function is complex and not always completely understood (27). In other words, the synthetic DNA molecule may function in theory but not necessarily in practice.

2.1.2 Reporter Genes

A reporter gene makes cells expressing the reporter gene visible either with the naked eye or with the use of an imaging modality. A reporter gene functions by expressing a protein or functional RNA that ends up producing a phenotype that makes the cells visible. In the case of the green fluorescent protein, GFP produces green fluorescence when it is activated with ultraviolet light. In the case of MRI, whatever the phenotype gained by cells expressing an MRI reporter gene, it must result in the enhancement of the cells' MRI image contrast.

With any MRI reporter gene, it is possible to genetically engineer the reporter gene and its regulatory units such that it is possible to produce tightly-controlled contrast. For instance, a reporter gene construct may be designed such that the reporter gene is upregulated or downregulated only in certain tissues or only in response to a specific biological events, such as proteomic or metabolic changes (2). It is also possible to design the reporter gene such that it can be turned on and off at will by placing it under the control of a gene regulatory protein (28). The expression of the gene would then be controlled by restricting its contact with that protein which, depending on the protein, either promotes or prevents the expression of the gene. For strict control, the regulatory

protein should not be present in the cells expressing the reporter gene, but it should be easily delivered to the cells as needed. In contrast, the reporter gene may instead be constitutively expressed so that there is no need for a regulatory protein. An MRI reporter gene which is constitutively active encodes its protein constantly, so cells expressing a constitutively active reporter gene generate MRI contrast every time they are imaged with MRI.

2.1.3 Magnetotactic Bacteria

As the name indicates, magnetotactic bacteria are capable of magnetotaxis, which is the ability to detect, orient, and navigate along the Earth's geomagnetic field (29, 30). They are able to migrate along magnetic field lines because the bacteria synthesize and intracellularly align a number of organelles called magnetosomes that act like compass needles. In our search for a gene which have the potential to enable cells to enhance MRI contrast, we directed our attention to genes unique to magnetotactic bacteria not simply because they are capable of magnetotaxis but because it was discovered that the reason they are capable of magnetotaxis is because their specialized organelles, or magnetosomes, contain magnetic, iron-bearing crystals. These nano-sized crystals are comprised of biominerals, either the magnetic iron oxide magnetite, Fe_3O_4 or, less commonly, the magnetic iron sulfide greigite Fe_3S_4 (31). To form the crystals, the bacteria must transport iron into the magnetosome, which is enveloped by an organic membrane, a protein-containing lipid bilayer called the magnetosome membrane (32). Specific proteins are required for the uptake and transport of iron from the extracellular space across the cell membrane and the magnetosome membrane and into the magnetosome. Once inside the cell, the iron goes through a process of biomineralization to convert it to magnetite or greigite (31).

magA was discovered in a study where five non-magnetic magnetotactic bacteria were generated by the insertion of transposon Tn5 into the genome of a strain of magnetotactic bacteria named *Magnetospirillum* sp. AMB-1 (33). Because the transposon caused a mutation in the genome that resulted in a change in phenotype, it was deduced that the mutated DNA fragment was required for synthesis of magnetic particles. Researchers sequenced that DNA fragment and ended up isolating a 1.3 kilobase (kb) gene which they named *magA*. When they compared its sequence to other bacterial DNA, they found that *magA* is homologous to cation efflux proteins and concluded that *magA* likely encodes an iron transporter involved in the synthesis of magnetic particles in the magnetotactic bacteria (34). Furthermore, intracellular localization of the *magA* protein was examined using a MagA–luciferase fusion protein. The results indicate that this protein is a membrane bound protein localized in both the cell membrane and magnetosome membrane (35). However, recent evidence argues that *magA* is neither necessary for the biomineralization process nor an iron transporter and suggests that it is also not a magnetosome membrane protein (36, 37).

Unlike *magA*, *mms6* is a 411 base pair magnetotactic bacteria-specific gene. In other words, it has no homology to other proteins in non-magnetic organisms (38). It was first discovered when researchers isolated and analyzed magnetosome membrane proteins. One of the proteins that was extracted was a low molecular mass protein bound tightly to the magnetosome membrane of the magnetotactic bacteria *Magnetospirillum* strain AMB-1 (39). This protein was named Mms6. To study its function, the same researchers also created a recombinant Mms6 protein in *E. coli* which they used in an iron-binding assay and found that recombinant Mms6 was able to bind iron. In a separate study, recombinant Mms6 was also found to bind iron and was shown to play a role in the *in vitro* formation of uniform 30 nanometer (nm)-sized, superparamagnetic magnetite

crystals (40). In a more recent study, *mms6* was deleted from the magnetotactic bacteria *Magnetospirillum magneticum* AMB-1. Electron micrographs revealed that the mutant strain synthesized smaller and irregularly shaped magnetite crystals as compared to the wild-type strain (41). Together, these results characterize Mms6 as an iron-binding protein that regulates the size and shape of growing magnetite crystals.

2.1.4 Transverse and Longitudinal Relaxation

2.1.4.1 Longitudinal and Transverse Relaxation

Recall that the magnetization vector is the sum of the dipole moment vectors in a homogenous isochromat. When the external, static magnetic field B_0 points in the direction of the positive *z*-axis, the magnetization vector also points in the direction of the positive *z*-axis. It remains in equilibrium until the rf pulse flips the magnetization vector to the *x*-*y* plane at t = 0. Once the magnetization vector is flipped, the longitudinal magnetization is at its minimum value (i.e. zero), and the transverse magnetization is at its maximum value ($M_{xy}(0)$). Starting at t = 0, the longitudinal component of magnetization is given by:

$$M_z(t) = M_0\,(1 - e^{-t/T_1}) \tag{21}$$

where M_0 is the magnitude of the magnetization vector at equilibrium. This equation corresponds to the situation where the rf pulse experiment begins at t = 0 and not at some other arbitrary starting point. T_1 is called the spin-lattice relaxation time or the longitudinal relaxation time. As expected, the equation describes the regrowth of the longitudinal magnetization, starting from zero and returning to its equilibrium value

(Figure 4a). For some initial value of transverse magnetization ($M_{xy}(0)$), the transverse component of magnetization is given by:

$$M_{xy}(t) = M_{xy}(0)\, e^{-t/T_2} \tag{22}$$

The equation describes the decay of the transverse magnetization, starting from $M_{xy}(0)$ and decaying to zero (Figure 4b). T_2 is called the spin-spin relaxation time or the transverse relaxation time, and it is measured in milliseconds (ms).

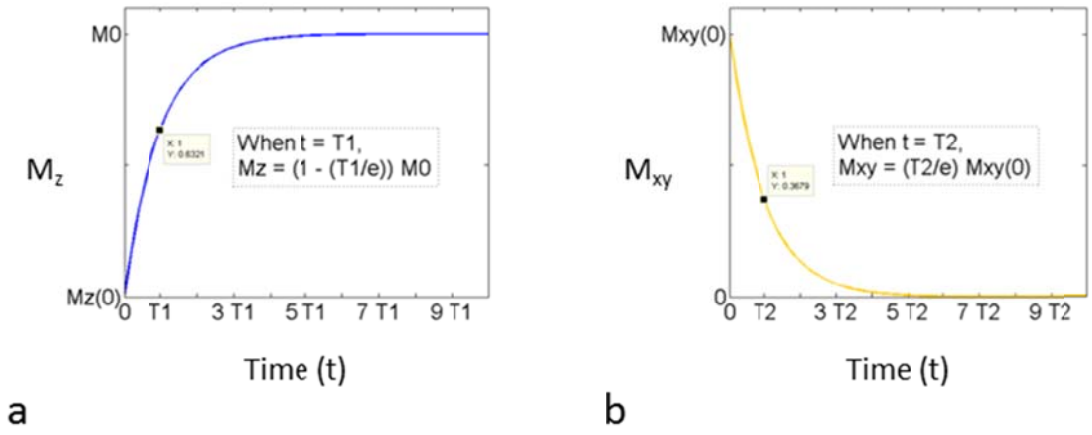

Figure 4: Graphs of the components of magnetization vs. time. (a) The longitudinal magnetization (M_z) begins at zero and recovers over time until it reaches the equilibrium magnetization (M_0). (b) The transverse magnetization (M_{xy}) begins at an initial value ($M_{xy}(0)$) and decays over time until it reaches zero.

2.1.4.2 The Effects of Transverse Relaxation on the Signal

Recall from Chapter 1 that the signal detected in the laboratory during an MRI experiment comes from the voltage induced in the receive coil by changes in magnetic

flux. The changes in magnetic flux are caused by the precession of the magnetization vectors. Since the signal is closely linked to the transverse magnetization, it is not surprising that as the transverse magnetization decays so does the laboratory signal. If the signal decays too quickly, the ADC will not be able to collect enough data to produce a good MRI image. During an MRI scan, additional magnetic fields can be added to the rf pulse sequence to lengthen the time it takes for the signal to decay, thus giving the ADC enough time to collect the data needed to form a good image. For example, in a spin echo sequence, several 180° pulses, also called π pulses, are applied at regular intervals to regrow the signal each time it decays.

When the rf pulse is turned off at t = 0, the magnitude of the signal (S_0) is at a maximum. It immediately begins to decay. When the 180° pulse is applied, the magnitude of the signal will regrow until it reaches a peak and begins to decay once again. Every time the signal decays, another 180° pulse can be applied. 180° pulses cannot be applied infinitely because each time the signal peaks, its magnitude is only a fraction of what it used to be (Figure 5a). By tracking only the magnitude of the signal when it peaks, a mathematical curve can be used to describe the manner in which the signal decays. As illustrated in Figure 5b, the signal decays exponentially ($S_0 e^{-t/T_2}$). As expected, the laboratory signal of a multiple spin echo sequence is limited by the transverse relaxation time of the magnetization vector (T_2). The signal of an object will decay slower if it has a long T_2 and will decay faster if it has a short T_2.

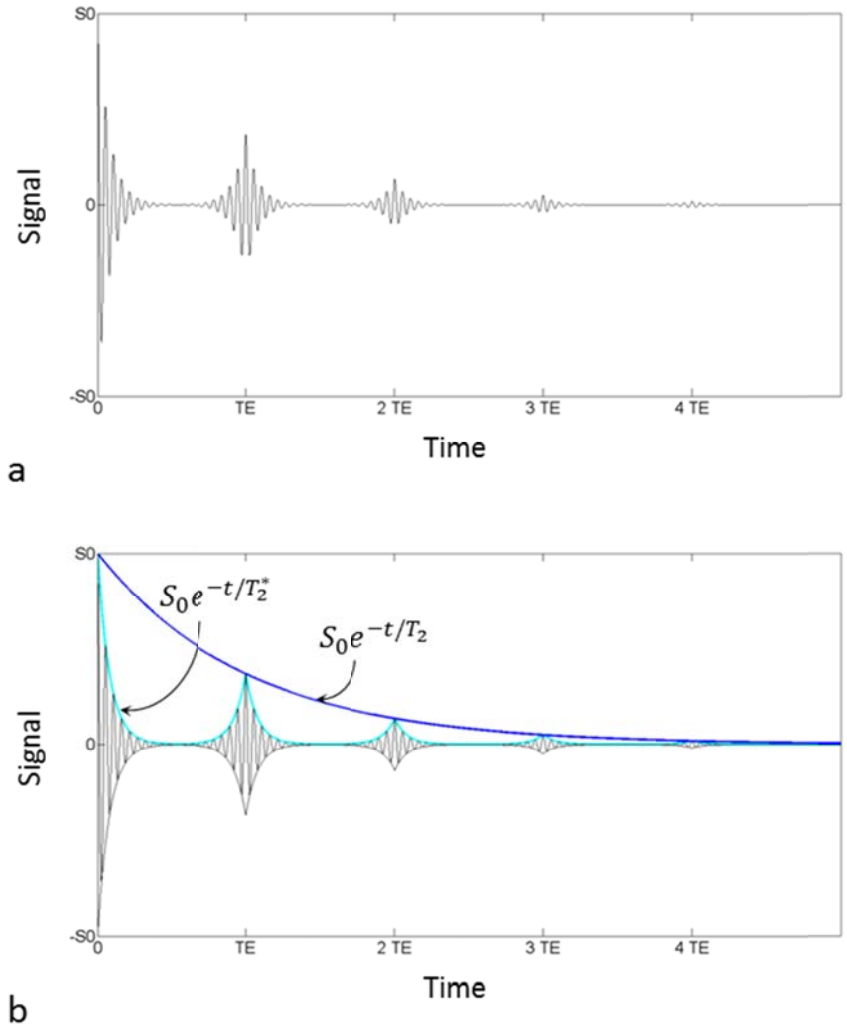

Figure 5: Transverse decay of the laboratory signal arising from multiple spin echoes. S_0 is the magnitude of the signal at t = 0. The signal decays over time. The time between the application of the rf pulse and the peak of the signal is called the echo time (TE). (a) The emf signal, i.e. the laboratory signal, measured over time. (b) The signal strength is limited by two envelopes (blue curves), both of which decay exponentially.

2.1.4.3 T_1 and T_2-weighted MRI Imaging

MRI is an imaging technology that generates an image by taking advantage of the physical principles of nuclear magnetic resonance. When an object or subject lies in an MRI scanner, a strong magnet aligns all the unpaired dipole moments in the atoms of that object. Then, a radio frequency pulse, or a magnetic field oscillating with a radio frequency, is applied to the object causing the dipole moments to rotate. Once the rf pulse is turned off, the dipole moments of the atoms return to their original position. Because the dipole moments of different atoms do not return, or relax, to their original position at the same rate, an MRI image of the object can be created after the MRI scanner records the time it takes the dipole moments in the object to relax and mathematically translates that information into an image (42, 43). If the protons in two adjacent objects have different relaxation times, image contrast between the two objects can be generated by making the different relaxation times correspond to different signal intensities in the final MRI image.

There are two different relaxation times that are measured and used to produce an image, the longitudinal (T_1) and transverse relaxation (T_2) times. The image contrast between two objects or two tissues can be increased if the difference between their T_2 relaxation times is greater than the difference between their T_1 relaxation times, or vice versa. In that case, T_1-weighted or T_2-weighted MRI can be used to emphasize one relaxation time over the other. In T_2-weighted images, short T_2 relaxation times produce hypointensities on the image and long T_2 relaxation times produce hyperintensities. The opposite is true in T_1-weighted images; short T_1 relaxation times produce hyperintensities on the image and long T_2 relaxation times produce hypointensities. Hyperintensities appear as bright areas in an MRI image, while hypointensities appear as dark areas.

2.2 Approach

2.2.1 Creation of Stable Clones

After we made the decision to examine the possibility that *mms6* and *magA* could be used as MRI reporter genes, the first objective was to generate stable, single cell clones. A single cell clone is a group of cells comprised entirely of the progeny of a single cell so all the cells are identical. Using the same clone for all experiments in a study is ideal because using different clones could potentially introduce a confounding variable into an experimental design. A stable single cell clone is simply a single cell clone that has been transfected with a gene whose expression levels remain stable, often over a period of months or even years. The creation of stable single cell clones, which from now on will be referred to simply as a clone, saves time by making it unnecessary to have to transfect cells often. Because the clonal cell line can be expanded, all experiments can be conducted with the same clone.

We obtained the genetic sequences for *magA* and *mms6* from Genbank, an online database, and custom-ordered the genes from a commercial vendor. Because *magA* and *mms6* are native to bacterial genes, the nucleotide sequences were optimized for expression in mammalian cells. In other words, the nucleotide sequence was altered slightly from the sequence published online to ensure that the Mms6 protein being expressed in the mammalian cells would be identical to the one being expressed in the magnetotactic bacteria. Once we received the two plasmids, we used standard subcloning methods to transfer the genes to a vector of our choosing. Basically, we used restriction enzymes to excise each gene from its parent vector, i.e. the vector in which it came, and used a ligase to clone each gene into a vector called pBudCE4.1. With pBudCE4.1, a 4.6

kb vector, two genes can be simultaneously, constitutively expressed in mammalian cell lines and clones can be generated. We chose a constitutively active vector to regulate our genes because an inducible vector requires the presence of a regulatory protein to turn gene expression on or off. Since we wanted to express our genes *in vivo*, we preferred not to face the challenge of assuring that the regulatory protein was reaching the vector. The vector contains the regulatory sequences that will flank the gene once it is ligated into the vector. The regulatory sequences control the expression of the gene in the host cell. In addition, pBudCE4.1 adds an epitope tag to the C-terminal end of the recombinant protein. We chose to add unique tags to MagA and Mms6 because the epitope tag can be used for the detection and purification of the recombinant protein (44).

Once each gene was in its own destination vector, we wanted to confirm that the genes had not been mutated during the subcloning process. The genes, now cloned into a vector of our choosing, were sent to an outside vendor for sequencing. We compared the sequences of the genes cloned into pBudCE4.1 with the optimized sequences we had ordered and confirmed that the two sequences were identical.

Next, we needed to choose the cell lines that we would be transfecting. We wanted to test more than one type of adherent, mammalian cell line, so we chose rat gliosarcoma cells called 9L cells, human kidney epithelial cells called 293T cells, and mouse hepatoma cells called Hepa 1-6 cells. 9L cells were chosen because they could be used in future rat *in vivo* experiments, and the 293T cells were chosen for their high transfectability. Hepa 1-6 cells were chosen because they could be used in future mouse *in vivo* experiments.

To transfect our cell lines, we chose a lipid-based transfection technique called lipofection. Lipofection is a technique used to transfer genetic material into a cell. First, DNA is coupled with liposomes to form a DNA-lipid complex (45, 46). The method by

which the complex is then internalized and transported into the nucleus is not well understood, but there evidence suggests that the complex enters the cell via endocytosis and that the liposome then enters the nucleus either by directly fusing with the nuclear envelope or by depositing the DNA-lipid complex into the cytoplasmic matrix where it is transported to the nucleus (47). Despite the fact that not much is known about the pathway of this transfection method, we chose to use lipofection because it is an established transfection technique that is widely used, inexpensive, easy to use, and suitable for transient, stable, and co-transfection of mammalian cells (45).

Lipofection is not 100% efficient, so after the reagent is used to transfect a group of cells, cells that are successfully transfected are mixed with cells that are not. Cells that are transfected need to be separated from cells that are not transfected. Because the gene construct included an antibiotic resistance gene, standard cell cloning techniques were used to kill negative cells, i.e. cells that do not express the gene of interest, while leaving alive the positive cells, i.e. cells that contain the gene of interest. Briefly, once we transfected the cells, the antibiotic Zeocin was added to the cell culture medium. After a few days, only cells expressing the Zeocin resistance gene, cells which also express *mms6* or *magA*, survived. At this step in the process, adding Zeocin to the cell culture medium served a dual purpose: it not only killed the negative cells, it also began the process of selecting stably transfected cells. Transiently transfected cells lose the transgene and their antibiotic resistance genes over time. If Zeocin were no longer added to the growth medium after the death of all the cells that had not been successfully transfected, over time, the remaining cells would once again become a mix of positive and negative cells. Zeocin must always be added to the medium to kill any cells that lose the transgene. The antibiotic is thus used to create a stably transfected cell line.

During transfection, a transgene integrates into the genome randomly, and the site of integration can mutate native genes as wells as affect transgene expression. Even if two different cells were the progeny of the same transfected negative cell line, were transfected with the same gene, and were transfected in the same manner; the cells would not be identical. Stably transfected positive clones must thus be created. To do this, a single positive cell and its progeny needs to be separated from the other stably transfected cells. This occurs at the end of the antibiotic selection process. When Zeocin was added to the cells in order to kill the cells that were not transfected, the remaining positive cells were subcultured into cell culture dishes such that only a limited number of cells were grown on each dish. After the cells attached to the cell culture plate, a single cell had enough room to divide without it or its progeny ever nearing any other cells. To isolate positive clones, a single cell and its progeny were transferred to their own culture dish. The end result was the successful creation of a positive clone. To increase the probability that the selected clones were indeed pure, we repeated the last part of the cell cloning process: single cell cloning. In other words, the clonal cells were subcultured into cell culture dishes such that only a limited number of cells were grown on each dish. Single cells and their progeny were once again isolated.

2.2.2 Selection of a Positive Clone for Further Study

Once *magA*-positive and *mms6*-positive clones were created, we decided to screen the newly created clones to determine which of the clones could produce the most *in vitro* contrast. We did this for two reasons. First, not all clones necessarily produce the same amount of contrast, even if they are clones originating from the same host cell line and expressing the same gene. The difference arises because every time a cell is transfected with a gene, the gene integrates in random parts of the genome; and the particular

integration site will affect gene expression (48). Second, the clone able to produce the most *in vitro* NMR signal is probably the best candidate for *in vivo* imaging because the higher the NMR signal produced by a clone *in vitro*, the more likely that its signal will be distinguishable *in vivo* from the signal produced by surrounding biological tissue and thus the more likely the cells will be visible on an MRI image. In other words, the detection of the NMR signal produced by cells surrounded by animal tissue is significantly more difficult than the detection of that signal when those same cells are collected in a tube and are surrounded by air, as is the case in the *in vitro* imaging of the cells. Thus, given the low sensitivity of MRI, it was essential that we selected cells that were the strongest *in vitro* producers of contrast—the stronger the better considering the threshold for *in vivo* detection of cells is high.

The goal of the selection process was to identify the positive clone whose MRI image contrast increased the most compared to wild-type cells, presumably due to the expression of the recombinant reporter. We could have just imaged all of the clones to directly find the one that was able to produce the most image contrast; however, growing up the number of cells necessary for imaging is expensive and requires lots of materials and reagents. Instead, we wanted a faster and easier process to eliminate the clones with the least potential to produce contrast. In the magnetotactic bacteria, we believed at the time that *magA* expressed a protein that was a putative iron transporter, and *mms6* expresses an iron binding protein, so we thought there was a good chance that both recombinant proteins would increase intracellular iron storage. If we were right, then the iron stores would be visible by histological staining of whole cells growing on a cell culture dish.

When ferrocyanide comes in contact with iron, the Prussian blue dye is formed *in situ*. Under a microscope, blue deposits indicate the presence of iron. Prussian blue staining

requires only one plate of cells and does not take too long to complete. We thus used Prussian blue staining as a high throughput way to identify the clones that were able to take up more iron than host cells. The iron pool from which they could take iron was present in the culture growth media. Before being stained, that media and any iron that had not been taken up by the cells were removed from the plate.

The selection process occurred as follows: First, all clones were stained with Prussian blue. The number of blue deposits was visually assessed, and each clone was given a score of 1 to 4. A score of 1 was assigned to any clone that had approximately the same number of blue deposits as the host cells. In other words, these cells contained approximately the same amount of iron as the negative cells. The greater the number of blue deposits observed under the microscope, the higher the score the clone was given. Clones that received higher scores were then analyzed for transgene expression. The remaining clones were eventually discarded.

The clones that were created should have been, in theory, stable single cell cells; however, we wanted to confirm that the clones not only expressed the transgenes but also expressed the recombinant proteins. After a few days of growth and division, we took each clone and used RT-PCR (reverse transcription-polymerase chain reaction) and Western blot analysis to confirm that the transgenes were being transcribed and translated, respectively.

RT-PCR is used to detect the presence of the recombinant messenger RNA (mRNA) in a process that involves the use of two custom-made primers. When the total mRNA of a genome is mixed with the primers, the primers selectively anneal to the mRNA of interest, one at each end of the nucleotide sequence. Through the process of reverse transcription, cDNA is made using the piece of mRNA flanked by the primers as a

template. If the mRNA of interest is not located in the genome being analyzed with RT-PCR, then the two primers would have nowhere to bind, and the cDNA would not be made. RT-PCR was used to confirm that the transgenes were transcribed in the positive clones.

A Western blot is used to detect the presence of a protein of interest in a process that involves antibodies. The total protein of a clonal cell line is separated by size with gel electrophoresis. The total protein is transferred to a membrane and stained with antibodies that will selectively bind the protein of interest. The antibody is linked to a reporter enzyme with a chemiluminescent substrate. When the enzyme acts on its substrate, the luminescence can be detected with spectrophotometric methods. If the antibody is not detected, then the protein of interest was not expressed in the clonal cell line. A Western blot was used to confirm that the recombinant protein was present in the positive clones.

As the final step of the selection process, the clones were imaged with MRI. To measure the MRI contrast, the T_2 values of the cell pellets were measured at 3 T. We quickly discovered that without supplementing the cell culture medium with iron, the positive clones did not produce a significant change in contrast. We chose the experimental conditions of the imaging study based on *magA* research that had previously been completed in our laboratory (49). Basically, cells were cultured in a culture dish with medium supplemented with iron. Specifically, we cultured 9L and 9L4S cells for three days with cell culture media containing 200 micromolar (μM) of ferric citrate because a previous study found that when their positive clones are grown in medium with this concentration of iron and for these number of days, their positive clones produce maximum *in vitro* contrast (49). Then, the cells were transferred to a 1.5 milliliter (ml) tube and allowed to settle by gravity. Instead of letting the cells settle by gravity, the cells

could have been suspended in an agarose gel or could have been centrifuged. We found that the relaxation times of the cell samples differed depending on which of these three techniques were used. The cell samples are then scanned at 3 T with a T_2-weighted spin echo sequence.

2.3 Methods

2.3.1 Cell Culturing

Three types of adherent, mammalian cells were transfected: 9L cells (generously donated by Dr. Hyunsuk Shim (Emory University, Atlanta, GA, USA)), Hepa 1-6 cells (ATCC, Rockville, MD, USA), and 293T cells (ATCC). Cells were grown in 100 millimeter (mm) cell culture plates containing 10 ml of cell culture medium. The cell culture medium was 90% volume to volume (v/v) DMEM (Dulbecco's Modified Eagle's Medium) and 10% (v/v) of non-heat inactivated FBS (fetal bovine serum), supplemented with 100 units (U)/ml of penicillin and 100 U/ml of streptomycin. According to the manufacturer, the DMEM (ATCC) contained 0.00010 milligrams (mg)/ml of ferric nitrate ($Fe(NO_3)_3 \cdot 9H_2O$). Cells were grown at 37 degrees Celsius (°C) in an incubator containing 5% carbon dioxide (CO_2) and 95% air. The cell culture media used to culture positive clones was supplemented with 0.5 mg of Zeocin per ml.

2.3.2 Molecular Cloning

We selected both *mms6* and *magA* for our molecular MRI studies. The genetic sequences of the genes *mms6* and *magA*, both native to the magnetotactic bacterial, were obtained from GenBank and NCBI (National Center for Biotechnology Information) (50). Because the genetic sequences of *mms6* and *magA* vary slightly between species, gene sequences from three magnetotactic bacterial species were ordered. The *mms6* genes from *Magnetospirillum magneticum* strain AMB-1 and *Magnetospirillum gryphiswaldense* strain MSR-1 were ordered. The accession number for the former is NCBI Reference Sequence NC_007626.1 and for the latter is GenBank AM085146.1. The *magA* genes from *Magnetospirillum magneticum* strain AMB-1 and *Magnetospirillum magnetotacticum* strain MS-1 were ordered. These genes were synthesized in the form of complementary DNA (cDNA) from several commercial vendors, including Addgene (Cambridge, MA, USA), Bio Basic (Markham, ON, Canada), and GenScript (Piscataway, NJ, USA). Following the manufacturer's instructions that accompanied the vector, standard subcloning techniques were used to clone each gene into its own pBudCE4.1 vector (Invitrogen, Carlsbad, CA, USA), a constitutively active expression vector that comes with a Zeocin-resistant gene, an EF-1α promoter, and a polyhistidine-tag (V5-His). Of note, the gene was ligated into the cloning site after the vector was linearized with the restriction enzymes *Kpn* I and *Bgl* II.

2.3.3 Creation of Stable Clones

Following the manufacturer's instructions, Lipofectamine™ 2000 (Invitrogen) was used to transfect 9L cells, Hepa 1-6 cells, and 293T cells with *mms6*-positive vectors. We did the same with *magA*-positive vectors. Cells were not transfected with more than one gene. For transfection, cells were grown on a 100 mm plate and transfected with 24 micrograms (μg) of plasmid and 60 microliters (μl) of Lipofectamine.

After transfection, stable clones were created following the manufacturer's instructions that came with the pBudCE4.1 vector. In summary, transfected cells were seeded in seven 100 mm cell culture plates, 5.5×10^5 cells per plate, with fresh cell culture medium containing no Zeocin. The following day, the cell culture media of the seven plates was replaced with media supplemented with varying concentrations of Zeocin to determine the minimum amount of Zeocin necessary to kill the untransfected host cells. The seven concentrations of Zeocin were 0, 50, 125, 250, 500, 750, and 1,000 μg of Zeocin per ml of media. The selective medium was replaced every 3-4 days. By observing the cells under the microscope, the minimum concentration of Zeocin necessary to kill the untransfected host cells between seven and ten days was determined to be 500-750 μg/ml. These cells were discarded because they could not be used to select single cell stable clones. Instead, the process of single cell cloning began. Another batch of host cells was transfected with Lipofectamine following the manufacturer's instructions. 48 hours (hr) after transfection, 5.5×10^5 cells were seeded in a 100 mm plate with cell culture media containing no Zeocin. A few hours later, the cells had attached; and the cell culture media was supplemented with 750 μg of Zeocin per ml of media. Over the next few weeks, the media and the Zeocin were replenished every 3-4 days. During that time, the cells were observed under a microscope. Any single cells that expanded into colonies were isolated by washing the cells with phosphate buffered saline (PBS) and adding trypsin EDTA (Ethylenediaminetetraacetic acid) directly on the colony. Trypsin detaches cells from the plate. The colony was carefully transferred to a cell culture plate containing cell culture medium supplemented with 500 μg of Zeocin per ml of media. The cells in the colony, i.e. stable single cell clones, were given time to grow to confluency before being subject to another round of single cell cloning. The end result was the creation of *magA*-positive and *mms6*-positive stable clones.

2.3.4 Prussian Blue Staining

The clonal cells and host cells were each incubated with culture media containing 0 and 200 μM of iron (ferric citrate (Sigma-Aldrich, St. Louis, MO, USA)) at 37 °C for a period of three day. The cells were then washed with PBS and fixed with 4% paraformaldehyde. Iron staining assays were performed following the manufacturer's instructions accompanying the Prussian Blue Stain Kit (English Scientific, Clifton, NJ, USA). The assay entails treating cells with a 1:1 mixture of 5% potassium ferrocyanide and 5% hydrochloric acid (HCl) acid for 30 min and then staining them with Nuclear Fast Red for 10-15 s. After staining the cells, the cells were viewed under an Olympus IX71 epifluorescence microscope equipped with a digital color CCD camera. Clones with the greatest amount of blue deposits, an indication of the presence of iron, were then subject to RT-PCR analysis and Western blot analysis.

2.3.5 RT-PCR Analysis

Following the manufacturer's instructions, TRIzol® Reagent (Invitrogen) was used to isolate the total mRNA from the positive clones and the host cells. Also following the manufacturer's instructions, SuperScript™ III First-Strand Synthesis System for RT-PCR (Invitrogen) was used to synthesize the cDNA of the recombinant mRNA. The sequences of the two primers used in the RT-PCR reaction to detect the expression of *mms6* were 5′-GCGTGCCGGTTGGTACGAAA-3′ and 5′-AGTTCCACCTCTTCGTCGGACTGGG-3′ (GenBank accession number AB096081.1), and the primers for β-actin were 5′-GACAGGATGCAGAAGGAGAT-3′ and 5′-TGCTTGCTGATCCACATCTG-3′ (GenBank accession number X00351 and NM_031144.3). 35 cycles of PCR were performed: denatured at 94 °C for 30 s, annealed at 60 °C for 30 s, and extended at 72 °C

for 30 s. The PCR products were separated by electrophoresis, stained with ethidium blue, and viewed with a transilluminator. A 1.5% agarose gel was used to resolve the PCR products by electrophoresis.

2.3.6 Western Blot Analysis

M-PER Mammalian Protein Extraction Reagent (Thermo Fisher Scientific, Rockford, IL, USA) was used for the extraction of total protein from 1×10^7 cells. The protein was then quantified using the Pierce BCA® Protein Assay Kit (Thermo Fisher Scientific). The protein samples (30 μg/lane) were resolved with gel electrophoresis using a 12% SDS-PAGE (sodium dodecyl sulfate polyacrylamide gel electrophoresis) gel. The proteins were then electrophoretically transferred to a nitrocellulose membrane (Thermo Fisher Scientific). After blotting, the membrane was blocked with 5% (v/v) fat-free milk in 0.1% (v/v) Tween 20 in PBS (PBST). To detect the protein, membranes were incubated overnight at 4 °C with either anti-V5 mouse monoclonal antibody (1:1,000; Invitrogen, Carlsbad, CA, USA) or anti-β-actin mouse monoclonal antibody (1:5,000; Sigma, St. Louis, MO, USA). Recombinant Mms6 had a V5-His tag, and β-actin was used as a loading control. Membranes were washed three times with PBST before being incubated with the secondary antibody, a horseradish peroxidase (HRP)-conjugated antibody (1:10,000; Sigma-Aldrich).

2.3.7 *In Vitro* Imaging

Each stable clone was subcultured into 24 100 mm plates. The host cells served as the control cells and were also subcultured into 24 plates. The cells grew under one of two conditions. The cell culture media in half of the plates (12 of them) was not supplemented

with iron, and the cell culture media in the other half of the plates was supplemented with enough ferric citrate to make the concentration of iron in the media 200 μM. The iron used to supplement the media was ferric citrate. Once the complete growth media was added to the plates, the cells were left to grow undisturbed for three days in the incubator. After three days, the cells had grown to ~90-95% confluency. The culture media was removed from the plates, and the cells were washed with PBS. To detach the cells, 1 ml of trypsin EDTA was added to each plate. After five min, 3 ml of cell culture medium was added to each plate. For each experimental condition, the 12 plates were divided into four groups of three plates. The cells from each group were combined and put into separate 10 ml tubes. The cell solution was centrifuged for 5 min at 1,000 rotations per minute (rpm). The supernatant was removed, and the cell pellets were resuspended in 1 ml of PBS and placed into separate 1.5 ml tubes. The cells were then given time to settle by gravity for two to three hr at 4 °C. The cell pellet was then imaged with MRI. Since each cell pellet is considered one sample, in the end, there were four samples per experimental condition.

As a preliminary study, some cells were imaged immediately following transfection. These cells were only transiently transfected. Cells that were growing on a 100 mm cell culture plate with 15 ml of cell culture medium and that were ~90-95% confluent were transfected with Lipofectamine according to the manufacturer's instructions, with one exception: After the vector and Lipofectamine were added to the culture medium in the 100 mm cell culture plate, iron was also added. Enough ferric citrate was added to the cell culture medium to make the concentration of iron in the medium 133 or 400 μM. The cells were placed in the incubator for 23 or 48 hr. The cells from the plate were collected in a 1.5 ml tube and centrifuged at 5,000 rpm for one min at room temperature. With such a small number of cells in the tube, the supernatant might affect the T2 measurements, so

the supernatant was removed. The tubes were tapped to loosen the cell pellets and were taken to the scanner for imaging at 3 T.

The cell pellets were imaged in a 3 T MRI scanner (Siemens Magnetom Trio TIM® 3 T whole body MRI scanner, Siemens Medical Solutions, Malvo, PA, USA) with a multi-slice multi-echo (MSME) spin echo sequence. The following imaging parameters were used: repetition time (TR) = 2,000 ms, echo time (TE) = 10-200 ms in increments of 10 ms, echoes = 20, and slice thickness = 1 mm. The transverse relaxation times (T_2) of the cell pellets were calculated by fitting signal decay curves produced from the MSME sequence. The T_2 values of all the cell samples prepared under the same experimental condition were averaged. The results are sometimes reported in the form of the T_2 percent change:

$$T_2\ percent\ change = 100 \times \frac{T_2\ of\ cells\ (iron\ supplemented) - T_2\ of\ cells\ (not\ iron\ supplemented)}{T_2\ of\ cells\ (not\ iron\ supplemented)} \quad (23)$$

where "T_2 of cells" is the average T_2 value of cells incubated with or without iron supplemented medium, and "cells" refers to cells of the same cell line, either positive clones or control cells. Image processing and analysis were performed using MATLAB and Excel 2010. For *in vitro* experiments, three measurements were made, and error bars are ± standard deviation.

2.4 Results

From amongst the magnetotactic bacteria genes, two genes whose protein products were believed to be involved in the regulation of iron in the magnetotactic bacteria were chosen at potential MRI reporter genes. The first gene, *mms6*, binds iron and has a role in regulating the size and shape of the iron oxide crystals found within specialized organelles of the magnetotactic bacteria. When it was selected for this project, the second gene, *magA*, was considered a putative iron transporter. These two genes were transfected into three mammalian cell lines, 9L cells, Hepa 1-6 cells, and 293T cells. Because the nucleotide sequences of *mms6* and *magA* in three different strains of magnetotactic bacteria, MSR-1, AMB-1, and MS-1 are not identical; four different genes were used for transfection: the MSR-1 *mms6* gene, the AMB-1 *mms6* gene, the MS-1 *magA* gene, and the AMB-1 *magA* gene. As a preliminary study, Hepa 1-6 cells were transiently transfected with the AMB-1 *mms6*-positive pBudCE4.1 vector and the MSR-1 *mms6*-positive pBudCE4.1. The cells were incubated for 23 hr with 133 μM iron. As hypothesized, the *mms6*-positive cells had a smaller T_2 value than the host cells grown under the same conditions. The T_2 values of the host cells, of the cells transiently transfected with the AMB-1 *mms6*-positive pBudCE4.1 vector, and of the cells transiently transfected with the MSR-1 *mms6*-positive pBudCE4.1 vector were 144 ms, 88 ms, and 84 ms, respectively. Interestingly, Hepa 1-6 cells grown for 23 hr *without* any iron supplement had a T_2 value of 117 ms. Because iron decreases T_2 values, we did not expect the T_2 value of Hepa-1 cells grown without an iron supplement (117 ms) to be smaller than the T_2 value of the Hepa 1-6 cells grown with an iron supplement (144 ms).

293T cells were transiently transfected with the AMB-1 *magA*-positive pBudCE4.1 vector and the MS-1 *magA*-positive pBudCE4.1 vector. The cells were incubated for 48 hr with 400 μM iron. Based on the results of previous research (49), we expected the *magA*-positive cells to have a smaller T_2 value than the host cells grown under the same conditions; but there was no statistical difference between the values. The T_2 values of

the host cells, of the cells transiently transfected with the AMB-1 *magA*-positive pBudCE4.1 vector, and of the cells transiently transfected with the MS-1 *magA*-positive pBudCE4.1 vector were 211 ms, 204 ms, and 200 ms, respectively.

Using molecular cloning techniques, several dozen *magA* and *mms6*-positive clones were created out of the different combinations of genes and host cells. Because we started working with *magA* long before we started working with *mms6*, *magA*-positive clones were not subject to an elimination process. Instead, newly created stable clones were immediately imaged at 3 T. Despite repeated attempts, no difference in T_2 values was measured (data not shown). RT-PCR and Western blot analysis confirmed that the *magA* was expressed in the clones (data not shown), yet the clones did not produce statistically significant changes in T_2. The imaging results of the stable clones are consistent with the imaging results of the transient transfection of 293T cells with *magA*.

Because a few dozen *mms6*-positive clones had been created, we focused our attentions on 9L clones and 293T clones. This decision was made because the 9L cells could be used to create the animal model we eventually wanted to create and because the 293T cells had been successfully used to test an MRI reporter gene in a previous study (49). Thus, the Hepa 1-6 clones were frozen in liquid nitrogen for long term storage.

Only the *mms6*-positive 9L and 293T clones were subject to the elimination process. First, 28 *mms6*-positive 9L clones and 11 *mms6*-positive 293T clones were analyzed with Prussian blue staining. The number of blue deposits observed in the clones was compared to the number of blue deposits in the host cells. The number of blue deposits was visually evaluated and assigned a score of 1 to 4 (Figure 6).

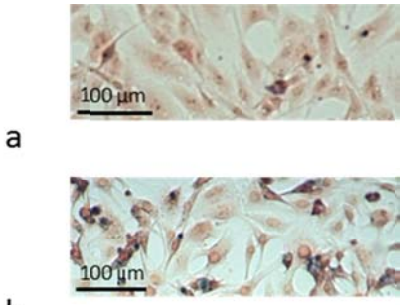

Figure 6: Prussian blue staining of transfected cells. (a) Transfected cells were screened for the presence of iron with Prussian blue staining. The amount of blue stain was visually evaluated and assigned a score of 1 to 4. Clones were assigned a score of 1 if they showed the same level of staining as control cells. A score of 4 was assigned to the transfected cells with the greatest amount of staining. (a) Control cells (9L) stained with Prussian blue and assigned a score of 1. (b) Transfected cells stained with Prussian blue and assigned a score of 4.

Clones were assigned a score of 1 if they showed the same level of staining as control cells. A score of 4 was assigned to the transfected cells with the greatest number of blue deposits. Table 1 contains a summary of the scores given to *mms6*-positive 293T clones, and Table 2 contains a summary of the scores given to *mms6*-positive 9L clones.

Table 1: Systematic selection of an *mms6*-positive 293T clone with the greatest MRI contrast. After transfection with *mms6*, 293T single cell clones were isolated and then put through the following selection process: First, 293T clones were stained with Prussian blue. The amount of blue stain was visually evaluated and assigned a score from 1 to 4. Clones were assigned a score of 1 if they showed the same level of staining as control cells (293T cells). Clones that showed the greatest level of blue staining were then analyzed for *mms6* expression with RT-PCR and Western blot. Then, *mms6*-positive 293T clones were imaged with MRI. The percent decrease in the value of T_2 was used as a measure of MRI contrast. The larger the decrease, the greater the contrast.

293T Cells Transfected with mms6				
Clone Number	Prussian Blue Staining	RT-PCR	Western Blot	MRI
1	1			
2	3	Y	N	
3	3	Y	Y	34.0%
4	3	Y	Y	
5				
6	1			
7	3	Y	Y	25.9%
8	2	Y	N	
9	3	Y	Y	
10	3	Y	Y	20.2%
11	3	Y	Y	19.1%
12	2			
13	1			
14	1			
15	1			
16	2			
17	1			
18	3	Y	Y	23.1%
19	3	Y	Y	18.2%
20	1	Y	N	
21	1			
22	1			
23	2			
24	2			
25	3	Y	Y	25.0%
26	1			
27	1			
28	1			
29				
30	2	Y		

Table 2: Systematic selection of the *mms6*-positive 9L clone with the greatest MRI contrast. After transfection with *mms6*, 9L single cell clones were isolated and then put through the following selection process: First, 9L clones were stained with Prussian blue, an iron stain. The amount of blue stain was visually evaluated and assigned a score from 1 to 4. Clones were assigned a score of 1 if they showed the same level of staining as control cells (9L cells). Clones that showed the greatest level of blue staining were then analyzed for *mms6* expression with RT-PCR and Western blot. Then, *mms6*-positive 9L clones were imaged with MRI. The percent decrease in the value of T_2 was used as a measure of MRI contrast. The larger the decrease, the greater the contrast. The positive clone number 4, whose row in the table has been highlighted yellow, was named 9L4S and was used for further study.

9L Cells Transfected with mms6				
Clone Number	Prussian Blue Staining	RT-PCR	Western Blot	MRI
1	1	N		
2	3	Y	Y	32.1%
3	1	N		
4	4	Y	Y	37.5%
5	1	N	N	
6	3	Y	Y	30.9%
7	2	Y	N	
8	2	Y	Y	24.6%
9	2	Y	N	
10				
11	1	Y	Y	
12	2	N		

24 clones with the highest amount of Prussian blue staining, a stain that indicates the presence of iron, were analyzed for gene expression with RT-PCR. RT-PCR analysis confirmed that 20 out of 24 clones were expressing *mms6* and that the wild-type cells were not (Table 1 and Table 2). Western blot analysis confirmed that 14 out of 20 clones were expressing the recombinant protein Mms6 and that the wild-type cells were not

(Table 1 and Table 2). For example, 9L cells do not contain the mRNA of the *mms6* gene nor do they express the Mms6 protein, while one of the clone transfected with the *mms6*-positive vector expresses both the *mms6* mRNA and the Mms6 protein (Figure 7).

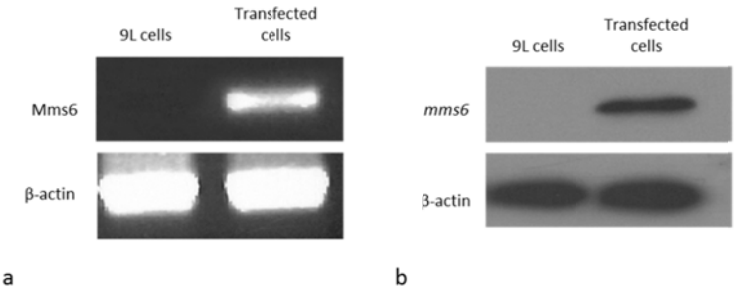

Figure 7: Analysis of transgene expression in 9L cells and transfected 9L cells. (a) RT-PCR analysis of *mms6* gene expression in wild-type 9L cells and transfected 9L cells. A dark band indicates the presence of *mms6* or β-actin. (b) Western blot analysis of Mms6 protein expression in wild-type 9L cells and transfected 9L cells. A dark band indicates the presence of Mms6 or β-actin. β-actin was used as a loading control.

The 11 clones that were growing well in the cell culture dishes, that seemed to have the most intracellular iron, as indicated by the results of Prussian blue staining, and that were expressing Mms6, as confirmed by RT-PCR and Western blot analysis, were subject to the last step of the selection process: magnetic resonance imaging at 3 T. The T_2 percent changes of all the *mms6*-positive clones, including both 9L and 293T positive clones, were greater than 18% (Table 1 and Table 2). Since the Prussian blue staining results indicated that all the positive clones that were imaged with MRI had increased amounts of intracellular iron relative to their respective wild-type cells, the imaging results supported the hypothesis that the iron in the cells shortened the T_2 values of the cells relative to their respective wild type cells. With a value of -37.5%, the *mms6*-positive 9L clone number 4 had the greatest T2 percent change. In comparison, the 9L cells, which are *mms6*-negative, had a T2 percent change of ~-10%. The *mms6*-positive 9L clone

number 4 was named 9L4S and selected for further study. The 9L4S clone expresses the 474 kb AMB-1 *mms6* gene. The 9L4S cell line was expanded for use in subsequent experiments.

2.5 Discussion & Conclusion

Our primary objective was to create stable clones expressing *mms6* and *magA*. Using standard molecular cloning techniques, we succeeded in making several dozen clones. We selected Prussian blue staining as the screen we would use to identify *mms6*-positive clones that showed increased levels of intracellular iron stain compared to wild-type cells. We selected Prussian blue staining because it is a sensitive, high-throughput, quick, and inexpensive assay, especially when compared to *in vitro* imaging, which we could have used to search directly for the clones that produce the most *in vitro* contrast. When we viewed the cells under a microscope, we expected to see both the positive and negative cells stained blue because all cells naturally take up iron because they need it to live (51). Relative to the wild-type cells, we also expected the positive cells to be stained more intensely because that would be consistent with our hypothesis that Mms6 enables cells to take up more iron than the wild-type cells. After staining the cells, we visually inspected the cells under the microscope and selected the clones that looked like they had been stained the most, both in terms of the number of cells that were stained and of the intensity of the iron stain. Though Prussian blue is a qualitative technique, relative differences in the intensity of the stain were significant enough that we were able to see that some clones were stained more than others, which indicated to us that they were able to take up more iron than the others. The fact that we were able to find evidence that at least some of the positive clones were able to take up more iron than the wild-type cells

alleviated a major concern. We knew that there existed a possibility that the transgene would not retain its ability to produce a functioning protein in a host cell or that it would express a protein that did not produce the phenotype in the cells that we expected, i.e. the uptake of iron. This is always a risk when expressing a transgene, especially if the gene is taken from one species and transferred to another.

After RT-PCR and Western blot analysis, our next objective was to determine whether the clones could produce MRI image contrast. We found that *magA*-positive clones could not produce any contrast, and that *mms6*-positive clones could. Importantly, *mms6*-positive clones required cell culture media that was supplemented with iron in order to produce contrast. That posed a potential problem because we planned to image the positive clones *in vivo.* We were concerned that the clonal cells would not have access to enough iron *in situ* to produce image contrast.

Multiple different cell lines were transfected with *magA*, and several dozen *magA* clones were made. Because there were slight differences in their nucleotide sequences, the *magA* genes from two different magnetotactic species were used for transfection. RT-PCR and Western blot analysis confirmed that the *magA* was indeed expressed in the clones. Despite repeated transfection attempts and careful examination of our cell culturing technique and imaging protocol, no statistically significant difference between the average T_2 value of *magA*-positive clones and the average T_2 value of the host cells was found. These results are not consistent with previous research which found that *magA*-positive cells produce MRI contrast (49, 52). We concluded that *magA* was not able to function as an MRI reporter gene in 9L cell, 293T cells, and Hepa 1-6 cells. Because no *magA*-positive clone was used for further study, from this point forward, this dissertation will only focus soley on the study of *mms6*-positive clones.

Both transiently transfected *mms6*-positive cells and stable *mms6*-positive clones produced MRI contrast, as measured by comparing the T_2 percent change of the clones with the T_2 percent change of the host cells. Through a process of elimination, we successfully identified one clone with the greatest T_2 percent change. That clone, which we named 9L4S, is an *mms6*-positive 9L clone. The T_2 percent change of the 9L4S cells was -37.5%. In comparison, the T_2 percent change of the 9L cells, which are *mms6*-negative, was approximately -10%. We concluded that *mms6*-positive clones could produce MRI contrast. The 9L4S cell line was expanded for use in subsequent experiments.

The maintenance of stable clones presents a challenge that could impact any future experimental use of 9L4S cells. The concern is that stable clones are only genetically stable for a limited amount of time, becoming less stable with each round of cellular division (53, 54). As the cells gain a growing number of mutations, the instability manifests itself in various forms, such as changes in cell morphology, in growth rate, in gene expression levels, and in chromosomal number. Some changes can be monitored under the microscope but unfortunately others cannot. Because experiments should not be performed with unstable cells, we took precautions to ensure that the cells we were working with had not been passaged for too long (55). These precautions consisted of keeping track of how times the cells being used for experimentation had been passaged, or subcultured. Clones that had been passaged for several months were discarded. Because we wanted to avoid having to make new clones, immediately after creating a clone, we took a fraction of the zero-passage cells and stored them in liquid nitrogen for future use. After expanding the remaining zero-passage cells, we also froze early-passage cells. If we had run out of clonal cells, we would have had to create more stable clones. As another precaution, the cells were visually inspected under the microscope every few days to make sure their morphology had not changed.

The transfection process itself could also have altered the normal function of the cell, for example, by causing the methylation of genes adjacent to the transgene or by mutating a native gene during the random insertion of the transgene into the host genome (56-59). Thus, soon after the clones were isolated, we discarded any clone that had a significantly different replication rate than that of the wild-type cells, as well as any clones that showed significant morphologically changes. To clarify, we only excluded clones that were *significantly* different from wild-type cells because we cannot assume that Mms6 does not itself cause a change in replication rate or a change in morphology. In fact, since we know that iron is toxic to cells and causes cell damage (51, 60) and because we have evidence that positive clones take up more iron than wilt-type cells, it is within reason to assume that the clones' morphology and growth rate might be altered due to the expression of *mms6*.

When lipofection is used to transfect a batch of wild-type cells, the lipofection does not transfect 100% of the cells. This is a concern because the MRI signal produced by a heterogeneous group of positive cells, i.e. composed of a mix of positive and negative cells, is weaker than the signal produced by a homogenous group of positive cells. Moreover, though our objective was to measure the NMR signal produced by transfected cells, due to MRI's low sensitivity, we did not expect to be able to detect the MRI signal produced by single cells. Since we wanted the positive clones to produce as much contrast as possible, we needed to create and maintain a homogenous group of positive cells. As explained in the methods section of this chapter, to create a homogenous group of cells, transfected cells were subject to two rounds of single cell cloning. To maintain a homogenous group of positive cells, the positive cells were engineered to express an antibiotics resistance gene.

CHAPTER 3

MEASUREMENT OF MRI CONTRAST PRODUCED BY MMS6-POSITIVE CLONES IN VITRO AND CHARACTERIZATION OF CELLULAR IRON UPTAKE

After we succeeded in detecting contrast produced by our positive cells at 3 T, we conducted a series of *in vitro* studies on a single *mms6*-positive clone. Even though our goal was to determine whether positive clones can enhance MRI contrast *in vivo*, the *mms6*-positive clone was first studied *in vitro* for the following reasons: First, the *in vitro* experimental designs were easier to carry out, cheaper to achieve, and faster to complete than the *in vivo* experimental design. Second, detecting contrast produced by cells *in vitro* is much easier than detecting contrast produced by cells growing in a biological tissue. Third, it is easier to execute a controlled experiment *in vitro*. Cells growing inside a living creature respond to and are affected by physical, chemical, and biological changes in its local environment, changes that are often beyond the control of the researcher but that may affect the outcome of the imaging experiment. In contrast, it is much easier to control the cell growth conditions *in vitro*.

For the *in vitro* experiments, we chose to focus our attention on only one positive clone. Because we planned to establish a tumor animal model using the same positive clones used for the *in vitro* studies, only positive clone derived from 9L cells were considered for further study. 9L cells were chosen from among the other options because they had already been used successfully by other researchers to make the same tumor animal model we were interested in making (61). Not only are 9L4S capable of producing tumors *in vivo*, 9L4S cells produced the most image contrast out of all the positive clones

that were created,. The *mms6*-positive 9L cells used for the studies described in Chapter 3 and Chapter 4 is a positive clone named 9L4S.

During the screening process described in Chapter 2, 9L4S was identified as an *mms6*-positive clone that produced MRI image contrast when imaged in a 3 T scanner after being grown for three days in cell culture medium supplemented with 200 μM of iron. For Aim 2, the 9L4S cells were used in additional *in vitro* imaging studies. For instance, the 9L4S cells were imaged in a 9.4 T scanner. Several batches of 9L4S cells were also imaged in a 3 T scanner after each batch of cells was cultured in cell culture medium containing a different concentration of iron.

Although Mms6 was an iron-binding protein in magnetotactic bacteria, we could not be certain how the recombinant protein would interact with iron in the cells that we had transfected. Even so, the possibility existed that if Mms6 could bind iron in the 9L4S cells, the amount of intracellular iron might increase in those cells. 9L4S cells were used to test the hypothesis that the change in MRI image contrast produced by 9L4S cells compared to the contrast produced by 9L cells might be due to a corresponding change in intracellular iron levels. An electron microscope was used to search for evidence of increased intracellular iron stores, and emission spectroscopy was used to measure the intracellular iron storage capacity of 9L4S cells.

3.1 Background

As discussed in Chapter 2, if the protons in two adjacent tissues have different T_2 relaxation times, contrast between the tissues on an MRI image can be generated by

making the different relaxation times correspond to different signal intensities in a T_2-weighted MRI image. If the expression of an MRI reporter gene in one of those two tissues changes the transverse relaxation time of that same tissue such that the numerical difference between its relaxation time and the relaxation time of the adjacent tissue increases, then the contrast between the two tissues on a T_2-weighted MRI image also increases. To change the transverse relaxation time of a tissue in which an MRI reporter gene is expressed, the MRI reporter gene must express a protein whose function within the cells leads to a change in transverse relaxation. In the case of *mms6*, we hypothesized that the difference between the T_2 value of 9L4S cells and the T_2 value of 9L cells was due to an increase in intracellular iron brought about by the expression of *mms6*. A brief discussion on the effects of iron on the transverse relaxation of neighboring protons will now be presented:

3.1.1 The Effects of Iron on Transverse Relaxation

MRI detects the magnetic perturbations of magnetic nuclei of specific elements (62). Because of its relatively high sensitivity, its magnetic properties, and its natural abundance in living organisms; hydrogen is the element whose magnetic dipole moment is most frequently manipulated and measured (7). Because iron is a superparamagnetic element, when it is found in an object, iron atoms will become a local source of magnetic field variation (13). Since local magnetic fields alter the magnetic dipole moments of atoms, including hydrogen, located within that field, magnetic elements are able to alter the NMR signal and the image contrast. Because iron is one such magnetic element, iron has been used as an MRI contrast agent in tissue-specific imaging and molecular imaging (63). Iron-based contrast agents can be characterized by their T_2 relaxation times because the local field variations produced by iron shorten the T_2 relaxation times of adjacent

atoms, including hydrogen. In T_2-weighted images, iron particles produce areas of hypointensities, or negative contrast, and are called negative contrast agents.

3.2 Approach

3.2.1 *In Vitro* MRI

After the 9L4S clone were chosen for all future experimentation, we began by more thoroughly investigating the MRI contrast generated by the 9L4S cells. When the 9L4S cells were imaged during the selection process described in Chapter 2, cells were incubated for three day with media containing 200 μM of iron. A total of four cell samples (N = 4) were imaged, and the imaging study was not repeated. To make sure that the imaging results were reproducible, the same imaging experiment was repeated 6 times over the course of 15 days. Please refer to the Approach section in Chapter 2 for more details. The experimental design of the imaging study is based on methods previously established by other members of our lab (49). The T_2 values of all the cell samples were averaged (N=24). For dosing studies, we varied the concentration of iron in the cell culture media to determine how much *in vitro* contrast the cells would produce when incubated with iron concentrations less than 200 μM of iron. This was important because when we used the 9L4S cells to establish an animal model, the cells would be exposed to a pool of iron with significantly less than 200 μM of iron, i.e. the iron in the blood (64, 65).

3.2.2 Prussian Blue Staining

Since the 9L4S cells produced changes in the relaxation rates, we wanted to investigate the intracellular iron content of the cells. We began by confirming that 9L4S cells stained with Prussian blue had a greater number of blue deposits than the host cells, which are the 9L cells. Prussian blue staining is a standard technique used to stain for iron presence in fixed, whole cells. Prussian blue staining involves fixing the cells on a culture dish and treating the cells with potassium ferrocyanide and with hydrochloric acid to release ferric ions from iron binding protein. A histochemical reaction occurs when any ferric iron (Fe^{3+}) present in the cells combines with ferrocyanide and results in the formation of ferric ferrocyanide, a blue pigment called Prussian blue that is visible under a microscope (66). Blue deposits seen in the cells indicate that iron is present; the more deposits that are seen, the more iron that is present. Even though Prussian blue is a qualitative technique, from experience we knew that a difference in the number of blue deposits in the positive cells and the number of blue deposits in the control cell, i.e. 9L cells, was clearly visible.

3.2.3 Intracellular Iron Measurement

To support the results of the Prussian blue staining, we wanted obtain a qualitative measure of the amounts of iron stored in 9L4S cells and 9L cells; so we cultured 9L and 9L4S cells for three days with media containing 200 μM iron, which was the same amount of time and the same concentration of iron that was used in the imaging studies. The cells were collected in a tube and sent to a chemical analysis laboratory. A type of emission spectrometry technique called ICP-OES was used to measure the iron content of our cell samples. ICP-OES uses inductively coupled plasma to heat the sample to

temperatures high enough to excite atoms and ions in the sample and causing each element in that sample to emit light. Since each element emits light of a particular wavelength, an element's presence in the sample can each be identified when its wavelength is detected. In addition, the concentration of an element in the sample can be calculated by measuring the intensity of the light emitted at that element's characteristic wavelength (67, 68). ICP-OES measures the relative concentration of trace elements in a sample. Specifically, it is used to measure how many μg of an element are found in every gram (g) of sample, i.e. parts per million (ppm). For instance, in our case, after drying the cell samples we sent them, they used ICP-OES to measure how many μg of iron were found in every g of dried cells.

3.2.4 Transmission Electron Microscopy

Because we had evidence that the 9L4S cells contained more iron than the control cells, we wanted to look at the distribution of iron within the cells. After being cultured with 200 μM iron for three days, we sent 9L and 9L4S cells to an electron microscopy laboratory where a technician prepared the clones for viewing under a transmission electron microscopy. Transmission electron microscopy (TEM) is a microscopy technique used to view the ultrastructure of a specimen after it has been sliced down to a thickness of approximately 70 nm. When an electron beam of uniform current density is transmitted through the specimen, the electrons interact with atoms in the specimen and scatter (69). An image is then captured of the electrons as they pass through to the other side of the sample. After our cells were prepared for viewing, we searched both the 9L4S cells, or *mms6*-positive cells, and the 9L cells, or *mms6*-negative cells, for evidence of intracellular iron under the microscope.

3.2.5 Trypan Blue Dye Exclusion Assay

The integration of a transgene into the host genome and the expression of a foreign protein in the host cell can sometimes alter cell viability and cell growth. We thus wanted to track cell growth and cell viability of the 9L4S clones over the course of 6 days and compare them to the cell growth and cell viability of the 9L cells. From amongst several options (70), we selected the Trypan blue dye exclusion test. The Trypan blue dye exclusion assay involves counting the number of cells that prevent the Trypan blue dye from passing through their cell membranes and into their cytoplasms. The assay entails adding the Trypan blue to a suspension of cells and counting the number of blue and clear cells. Since live (viable) cells possess intact cell membranes that prevent the dye from crossing their cell membranes and dead (non-viable) cells do not, tracking the number of blue and clear cells over a period of time is used to measure cell viability (71).

For the Trypan blue dye exclusion assay, a small number of cells were seeded on a plate and given time to replicate until the cells were confluent. To track how fast the cells were replicating, the number of cells growing on the plate was counted periodically. In summary, cells were seeded such that the cells, if they were allowed to grow for 6 day period, would be confluent on day 6 day. To track cell growth, every day for a period of 6 days, the cells were exposed to trypan blue dye. Using a hemocytometer, the cells were visually examined under a microscope. The number of blue cells and the number of clear cells were counted. Cell growth was examined with a graph of the number of live cells (clear cells) present on the cell culture plate vs time. The cell growth of both the 9L and 9L4S cells was monitored. The percent cell viability could also be calculated using the same data. The percent cell viability was calculated by dividing the total number of live cells (clear cells) by the total number of cells (blue plus clear cells) and multiplying that number by 100. The percent cell viability for both the 9L and 9L4S was calculated for

each of the 6 days. We then graphed the percent cell viability of the cell samples for each of the 6 days.

3.2.6 MTS Assay

Iron overload can lead to cell toxicity. Since our studies involve culturing cells with iron, it was important to determine how iron affects the viability of the cells and to determine if iron affected the cell viability of 9L cells more than 9L4S cells, or vice versa. Several viability assays exist, each of which measures cell viability on the basis of different biological principles (70). The viability assay we chose is called the MTS (3- (4,5-dimethylthiazol-2-yl)- 5-(3-carboxymethoxyphenyl)- 2-(4-sulfophenyl)-2H-tetrazolium) assay. The assay involves tracking the mitochondrial activity of a group of cells. Specifically, dehydrogenase enzymes located in the mitochondria convert MTS into formazan crystals, and the assay is used to measure the amount of formazan crystals produced by the enzymes. Since the detection of mitochondrial activity is indicative of cell viability, the detection of formazan crystals made by a group of cells is used as a measure of cell viability. Because enzymes require time to form the formazan crystals, the number of formazan crystals produced by live cells increases over time (72). The MTS assay entails spectrophotometrically measuring the number of formazan crystals produced by cells growing in a culture dish over a period of 1 to 4 hr.

We assayed 9L and 9L4S cultured in media with five different iron concentrations, for a total of 10 different samples. The samples were prepared in triplicate, bringing the total number of samples to 30. We began by plating enough 9L and 9L4S cells such that the cells became ~90% confluent after a period of three days. After three days, MTT was added directly to the cell culture medium and then left for a few hours in order to give the

mitochondrial enzymes time to convert the MTT to formazan. After the formazan was solubilized in the culture medium, the concentration of formazan was determined by measuring the absorbance of the culture medium.

3.3 Methods

3.3.1 Cell Culturing

Please refer to the methods section of Chapter 2, subsection *2.3.1 Cell Culturing*.

3.3.2 *In Vitro* MRI at 3 T

9L cells were seeded in 24 plates, and 9L4S cells were seeded in another 24 plates. For each cell line, 12 of the plates contained cell culture media supplemented with enough ferric citrate to make the concentration of iron in the media 200 μM. In the other 12 plates, the cell culture media contained no iron supplement. After three days in the incubator, the cells had grown to ~90-95% confluency in 100 mm plates. The culture media was removed from the plates, and the cells were washed with PBS. To detach the cells, 1 ml of trypsin EDTA was added to each plate. After five min, 3 ml of cell culture medium was added to each plate. The 12 plates were divided equally into 4 groups, 3 plates per group. The cells from each group were combined and put into separate 10 ml tubes. The cell solution was centrifuged for 5 min at 1,000 rpm. The supernatant was removed, and the cell pellets were resuspended in 1 ml of PBS and placed into separate 1.5 ml tubes. The cells were then given time to settle by gravity for two hr and 20 min at

4 °C. The cell pellets were imaged at 3 T. For details about the 3 T MRI scanner and the imaging parameters, please refer to the methods section of Chapter 2, subsection *2.3.7 In Vitro Imaging*. Once the T_2 values were measured, the transverse relaxation rates or relaxivity (R_2) of the cell pellets were calculated using the following equation:

$$R_2 \equiv \frac{1}{T_2} \tag{24}$$

In total, 16 samples were imaged at once: 4 samples of 9L cells cultured with an iron supplement, 4 samples of 9L cells cultured without an iron supplement, 4 samples of 9L4S cells cultured with an iron supplement, and 4 samples of 9L4S cells cultured without an iron supplement. After imaging, the 16 cell pellets, or samples, were stored at -20 °C. This imaging experiment was repeated 6 separate times on 6 separate days such that number of samples (N) per experimental condition was 24.

For the iron dosing experiment, 9L cells were seeded in 144 plates, and 9L4S cells were seeded in another 144 plates. For each cell line, the 144 plates were divided into 6 groups of 24 plates. Each of the 6 groups contained cell culture media with a different concentration of iron: 0, 50, 100, 150, 200, or 250 μM. The cells were prepared as described above. Since the cells from 3 plates are combined to make one sample, each group of 24 plates resulted in 8 samples (N = 8). The relaxation rates of the 8 samples were averaged. Data are represented in a bar graph as means, and error bars are ± standard error of the means.

3.3.3 *In Vitro* MRI at 9.4 T

8 plates of 9L cells and 8 plates of 9L4S cells were cultured with cell culture media supplemented with ferric citrate such that the concentration of iron in the media was 200 μM. Another 8 plates of 9L cells and 8 plates of 9L4S cells were cultured with cell culture media with no iron supplement. After three days in the incubator, the cells had grown to ~90-95% confluency in the 100 mm plates. The cells were detached from the plate with trypsin. The cells from each plate were collected and placed into separate tubes. The cell solution was centrifuged for 5 min at 1,000 rpm. The supernatant was removed, and the cell pellets were resuspended in 1 ml of PBS and transferred to separate 1.5 ml tubes. The cells were then given two hr to settle by gravity at room temperature. The cell pellets were imaged at 9.4 T. The number of samples (N) per experimental condition was 8. In total, 32 samples were imaged: 8 samples of 9L cells cultured with an iron supplement, 8 samples of 9L cells cultured without an iron supplement, 8 samples of 9L4S cells cultured with an iron supplement, and 8 samples of 9L4S cells cultured without an iron supplement.

The cell pellets were imaged in a 9.4 T Bruker BioSpec® 94/20 small animal scanner (Bruker, Billerica, MA, USA) with an MSME spin echo sequence. The following imaging parameters were used: TR = 4,000 ms, TE = 9.3-111.6 ms, Echoes: 12, and slice thickness = 1 mm. The transverse relaxation times (T_2) of the cell pellet were calculated by fitting a decay curve to the signal produced from the MSME sequence. The transverse relaxation rate (R_2) of a cell pellet was calculated using Equation (24). Image processing and analysis were performed using MATLAB and Excel. For in vitro experiments, three measurements were made, and error bars are ± standard error of the means.

3.3.4 Statistics

Statistical analyses were performed in Microsoft Excel 2010. An unpaired, two-tailed Student's t-test was used to calculate a *p*-value. A *p*-value of less than 0.05 was considered to be statistically significant.

3.3.5 Prussian Blue Staining

Please refer to the methods section of Chapter 2, subsection *2.3.4 Prussian Blue Staining*.

3.3.6 Intracellular Iron Measurement

The day after the final day of imaging at 3 T, all cell pellets were thawed, and all cells that had been cultured under the same growth conditions were combined in the same tube. Four tubes each contained one of the following: 24 imaging samples of 9L cells cultured with an iron supplement, 24 imaging samples of 9L cells cultured without an iron supplement, 24 imaging samples of 9L4S cells cultured with an iron supplement, and 24 imaging samples of 9L4S cells cultured without an iron supplement. Recall that every imaging sample was a mix of cells that had been cultured in three 100 mm cell culture plates, so each tube contained cells cultured in 72 cell culture plates. The four tubes were packed with ice bags and shipped overnight to the Chemical Analysis Laboratory at the University of Georgia (UGA, Athens, GA, USA) for ICP-OES analysis. The cells in each tube made up a single sample for intracellular iron measurement. First, the four cell samples were freeze dried. 0.25 g of dried cells was weighed out into crucibles and ashed at 500 °C for 4 hr. After they cooled, 2 ml of aqua regia was added to each cell sample, and the four samples were analyzed with ICP-OES.

3.3.7 Transmission Electron Microscopy

9L and 9L4S cells were cultured each cultured for three days with cell culture media supplemented with enough ferric citrate to make the iron concentration of the media 200 μM. The cells, still attached to the cell culture plate, were then sent for viewing under a transmission electron microscope located in the Robert P. Apkarian Integrated Electron Microscopy Core of Emory University. Whole cells were prepared by a microscopy core technician as follows: For examination under the electron microscope, monolayer cells cultured on glass coverslips were fixed overnight with 2.5% glutaraldehyde in 0.1 molar (M) cacodylate buffer (pH 7.4) at 4 °C. Cells were then washed with the same buffer and post-fixed with 1% buffered osmium tetroxide, dehydrated through a graded ethanol series to 100%, and embedded in Eponate 12 resin (Ted Pella, Redding, CA, USA). Ultrathin sections were cut on a Leica UC6rt or UltraCut ultramicrotome (Leica Microsystems, Bannockburn, IL, USA) at 70 nm and counter-stained with 4% aqueous uranyl acetate and 2% lead citrate. Sections were examined using a JEOL JEM-1400 (JEOL USA, Peabody, MA, USA) transmission electron microscope equipped with Gatan US1000.894 Ultrascan and SC1000.832 Orius CCD cameras (Gatan, Pleasanton, CA, USA).

3.3.8 Trypan Blue Dye Exclusion Assay

The Trypan blue dye exclusion assay was used to measure cell growth and cell viability of 9L and 9L4S cells incubated in cell culture media with no iron supplementation. For each cell line, 24 plates were seeded with 2.5×10^5. Enough cells were seeded such that the cells in each plate, if given the time, would be ~95% confluent in 6 days. 1 day later, the cells from 3 plates were trypsinized and re-suspended in culture medium. A small

volume of the cell solution was mixed with an equal volume of trypan blue (Invitrogen). The cells from the 3 plates were prepared and counted separately. Using a hemocytometer (Hausser Scientific, Horsham, PA, USA) and a brightsfield microscope, the number of blue stained cells and the number of unstained cells in each of the three plates were calculated and averaged. For each cell line, cell viability was calculated using the following equation:

$$Cell\ Viability\ (\%) = 100\ \times \frac{Average\ number\ of\ clear\ cells}{Average\ total\ number\ of\ cells} \qquad (25)$$

This procedure was repeated every day for an additional five days. Because the number of living cells, i.e. the number of unstained cells, was counted every day for a period of 6 days, cell growth was evaluated by graphing the number of living cells measured on a given day vs. the day on which the number of cells was counted. The data are presented as means ± standard deviation of the means.

3.3.9 MTS Assay

The CellTiter 96® AQueous Cell Proliferation Assay (Promega, Madison, WI, USA) was used to evaluate the cell viability of 9L4S and 9L cells using the manufacturer's instructions. In short, cells were cultured in a clear 96-well plate. Each well was seeded with 10^3 cells cultured with 100 µl of medium. The cell culture media was supplemented with enough ferric citrate such that the concentration of iron in the media was 0, 50, 100, 200, or 400 µM. These five concentrations of iron constitute the 5 experimental conditions. Because two cell lines were being assayed, there were a total of 10 different cell samples. To obtain an average, 3 of each of these unique cell samples were prepared, with one sample per well. After 3 days of incubation, 20 µl of CellTiter 96® AQueous

reagent (Promega, Madison, WI, USA) was added to each well and incubated for an additional 2 h at 37 °C. The absorbance at 490 nm was measured using the plate reader. Each of the 30 samples was measured 4 times. The data are presented as normalized means ± standard deviation of the measurements. For each of the 10 different cell samples, the cell viability of each of the 10 different cells samples was calculated using the following equation:

$$Cell\ Viability\ (\%) = 100\ \times \frac{Mean\ absorbance\ of\ a\ cell\ sample}{\begin{matrix} Mean\ absorbance\ of\ 9L\ cells \\ incubated\ with\ 0\ \mu M\ iron \end{matrix}} \qquad (26)$$

3.3.10 Statistics

Statistical analyses were performed in Microsoft Excel 2010. An unpaired, two-tailed Student's t-test was used to calculate a *p*-value. A *p*-value of less than 0.05 was considered to be statistically significant.

3.4 Results

As described in Chapter 2, 9L4S was chosen as the *mms6*-positive 9L clone that would be used in all future studies. It was the clone that was able to produce the most *in vitro* contrast, as gauged by T_2 measurements. In the *in vitro* experiments described in this chapter, 9L cells served as the negative control cells. The results of the RT-PCR assay and the Western blot assay confirmed that 9L cells do not express *mms6*.

9L and 9L4S cells were cultured for three days with culture media supplemented with enough iron to make the concentration of iron in the media 0 or 200 μM. The cell pellets were then imaged at 3 T with MRI. Another group of 9L and 9L4S cells were also cultured for three days with and without 200 μM of iron in the media. They were imaged at 9.4 T with MRI. We measured the average R_2 value of 9L cells to the average R_2 value of 9L4S cells at both 3 T and 9.4 T (Figure 8). Comparing 9L4S cells cultured with and without iron, there was a 56.8% increase in R_2 at 3 T and a 123.0% increase in R_2 at 9.4 T (both with $p < 0.0001$). In contrast, comparing 9L cells cultured with and without iron, a similar percent increase in R_2 was not observed; the iron supplementation led only to a 7.7% increase in R_2 at 3 T and an 18.6% increase in R_2 at 9.4 T. When the cells were cultured in media that had not been supplemented with iron, 9L4S cells showed only a 0.3% decrease in R_2 at 3 T and a 1.4% increase in R_2 a 9.4 T compared to the R_2 values of the 9L cells. In contrast, when cultured in media supplemented with iron, 9L4S cells showed a 47.5% increase in R_2 at 3 T and an 87.6% increase in R_2 at 9.4 T compared to the R_2 values of the 9L cells (both with $p < 0.0001$). As a negative contrast agent, iron increases he relaxation rates of the local pool of protons. The finding that 9L4S cells cultured with iron have a greater R_2 value than 9L cells cultured with iron is consistent with the previous results which indicate that 9L4S cells are able to take up more iron than control cells.

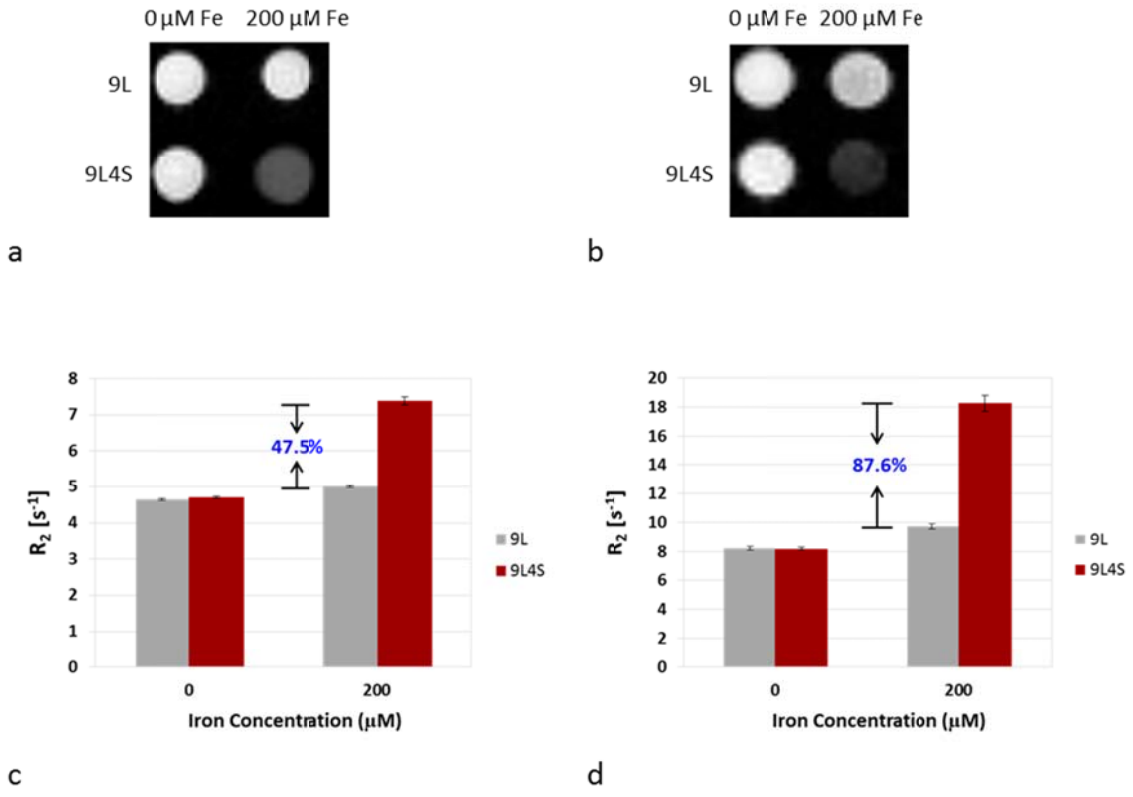

Figure 8: MRI images and corresponding relaxation rates (R_2) of in vitro cells. T_2 maps of four representative 9L and 9L4S cell pellets incubated for three days with or without iron and then imaged at (a) 3 T and (b) 9.4 T. Graphs of the average relaxation rate of 9L and 9L4S cells incubated for three days with or without iron and then imaged at (c) 3 T and (d) 9.4 T. The relaxation rates of the cell samples in (a) and (b) are included in the averaged relaxation rates graphed in (c) and (d), respectively. The number of samples (N) in (c) equals 12 and in (d) equals 8. Error bars indicate ± standard error of the means.

So far, all the experiments were conducted with media containing 200 µM of iron because a previous study had shown that the relaxation rate of cells incubated with iron reaches a maximum when the concentration of the iron in the cell culture media is 200 µM (49). In the final *in vitro* imaging study, we wanted to measure the R_2 values of cells cultured with media containing less iron. We repeated the same procedure as that used in the previous 3 T imaging experiment except this time the cells were cultured with media containing 0 µM, 50 µM, 150 µM, or 200 µM of iron. After three days, the cell pellets

were imaged at 3 T. The results of the iron dosing experiment show that the R_2 values of both the 9L and 9L4S increased as iron concentrations increased from 0 to 200 μM; however, the increase in R_2 over that range was more pronounced for the 9L4S cells (Figure 9). At each iron concentration, the average relaxation rate of the 9L4S cells was statistically different than the average relaxation rate of the 9L cells (all $p \leq 0.0007$).

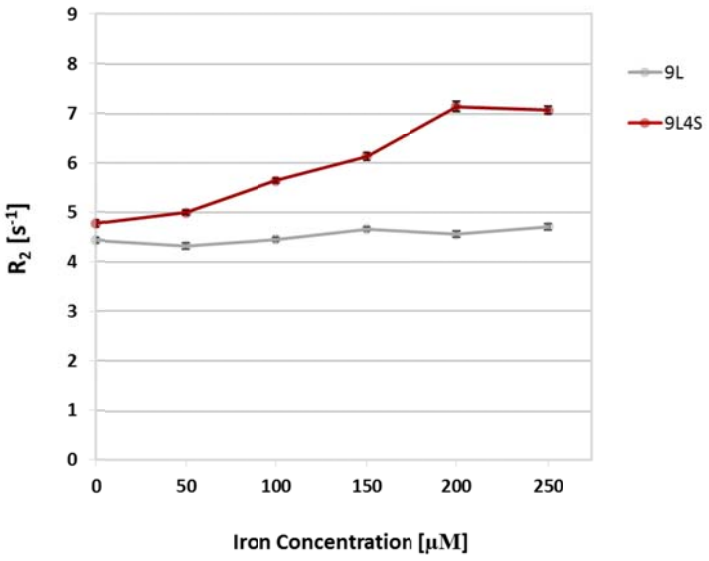

Figure 9: Relaxation rate (R_2) of cell pellets as a function of the concentration of supplemental iron. 9L and 9L4S cells were imaged at 3 T after being cultured in culture media supplemented with 0 to 200 μM iron. N = 8. Error bars indicate ± standard error of the means.

Since the imaging data showed that 9L4S cells have a faster relaxation rate than 9L cells, an investigation on the iron content of the same two cell lines was conducted. 9L and 9L4S cells were cultured in culture medium containing 200 μM of iron for a period of three days. Prussian blue staining of the cells showed greater iron staining in 9L4S cells compared to control cells (Figure 10). This finding is consistent with our hypothesis that *mms6* enables cells to take up more iron than wild-type cells.

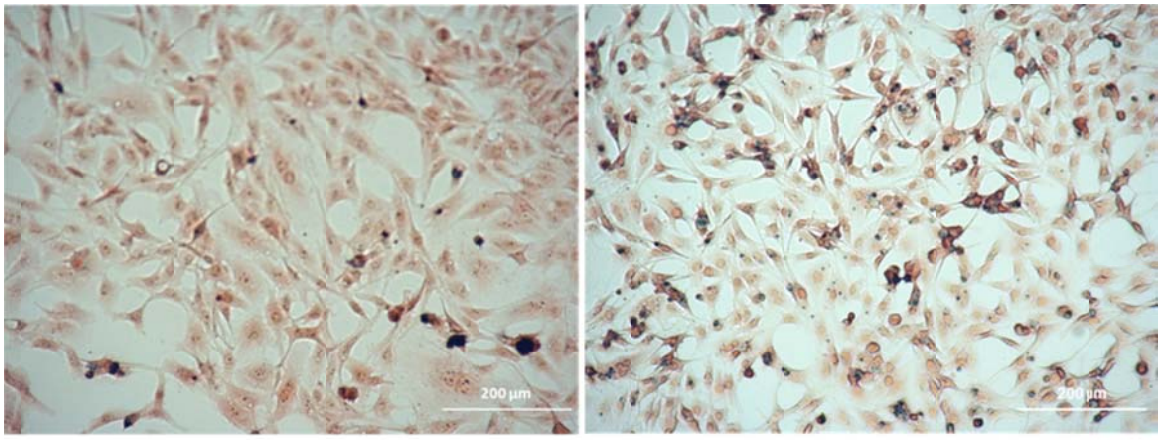

Figure 10: Prussian blue iron staining of 9L and 9L4S whole cells. Prior to Prussian blue staining, (a) 9L cells and (b) 9L4S cells had been incubated for three days with media supplemented with iron. The color blue indicates the presence of iron. 20X magnification.

9L and 9L4S cells were cultured with culture media supplemented with enough iron to make the concentration of iron in the media 0 or 200 µM. After a period of three days, the cells were collected and sent to a separate laboratory for elemental analysis. There, they used the freeze-drying and dry ashing method to prepare the samples for ICP-OES. The ICP-OES results were as expected; the 9L4S cells had significantly more intracellular iron than 9L cells (Figure 11). The spectrometry results showed that 9L cells that had been cultured with iron contained an 8.5-fold increase in iron compared to 9L cells that had not been cultured with iron. In contrast, 9L4S cells that had been cultured with supplemental iron contained a 24.7-fold increase in iron compared to 9L4S cells that had not been cultured with iron. To put it another way, when incubated with media supplemented with iron, 9L4S cells contained 2.8 times more iron than 9L cells. This

finding is consistent with both the Prussian blue staining results and the hypothesis that *mms6* enables cells to take up more iron than wild-type cells.

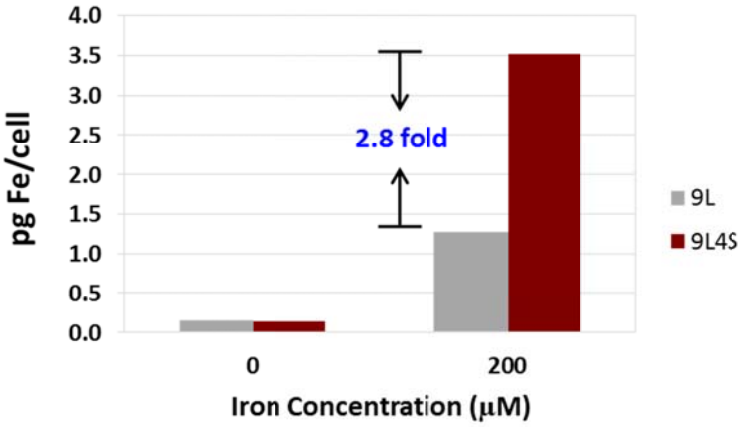

Figure 11: Quantification of iron uptake. Iron content of 9L and 9L4S cells that were cultured with either 0 or 200 µM of supplemental iron in the culture media. N = 1.

9L and 9L4S cells were cultured for three days with culture medium supplemented with enough iron to make the concentration of iron in the media 200 µM. Once the cells were fixed, they were taken to an electron microscopy laboratory. After our cells were prepared for viewing, we searched both the 9L4S cells and the 9L cells for evidence of intracellular iron under the electron microscope. We found black particles roughly 5 nm in size in both cell lines, but we found many more of them in the 9L4S cells than in the 9L cells (Figure 12). It is important to note that this finding is based simply on what we observed under the microscope; TEM cannot be used to measure the number of nanoparticles that are in the cell nor can it be used to determine the chemical composition of the nanoparticles. We postulate that the nanoparticles are iron oxide particles. If we are correct, then the microscopy results confirm that 9L4S cells contain more intracellular iron than 9L cells. If that were the case, the results would be consistent with the Prussian

blue staining results as well as the mass spectroscopy results. The results would also support the hypothesis that *mms6* enables cells to take up more iron than wild-type cells.

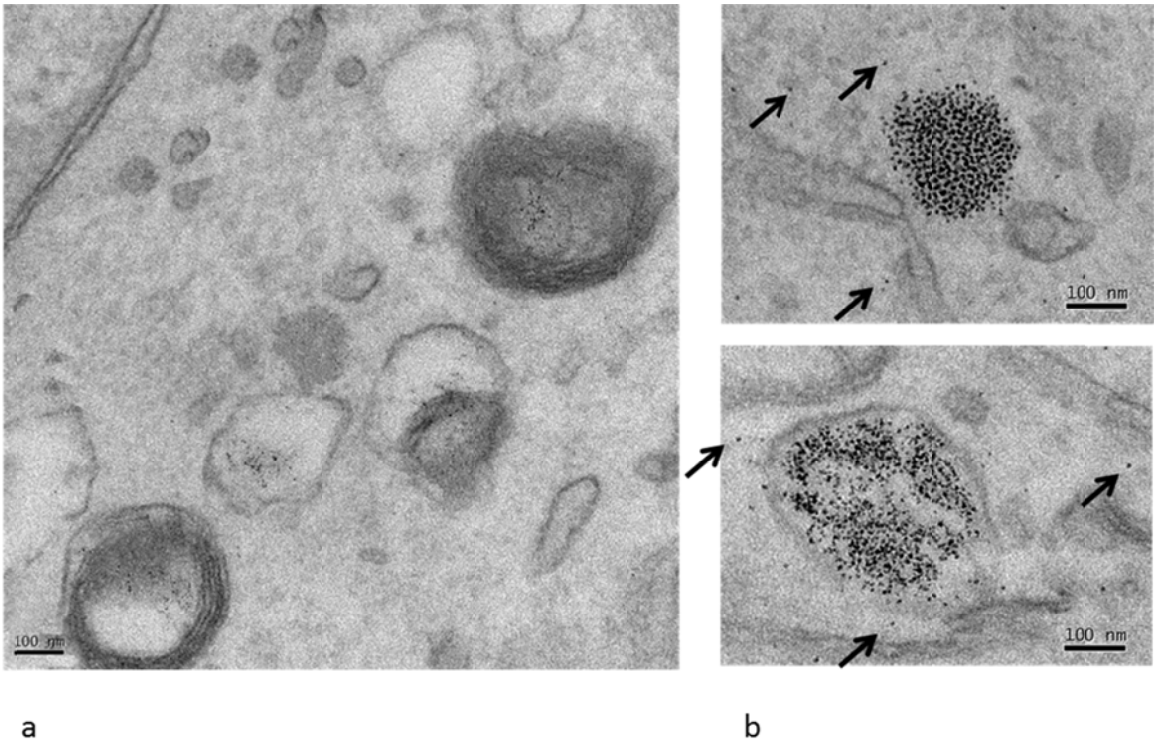

Figure 12: TEM images of putative iron oxide crystals located in the cytoplasm. Ultrastructure of (a) 9L cells and (b) 9L4S cells incubated for three days with media supplemented with iron. Nanoparticles were found (bottom right) within and (top right) outside of membrane-enclosed vesicles. Arrows indicate single nanoparticles.

The results of the Trypan blue dye exclusion assay showed that the 9L and 9L4S cells grew at almost identical rates over a period of 6 days and that the cells doubled approximately every 24 hr (Figure 13). As expected, the number of cells grew exponentially.

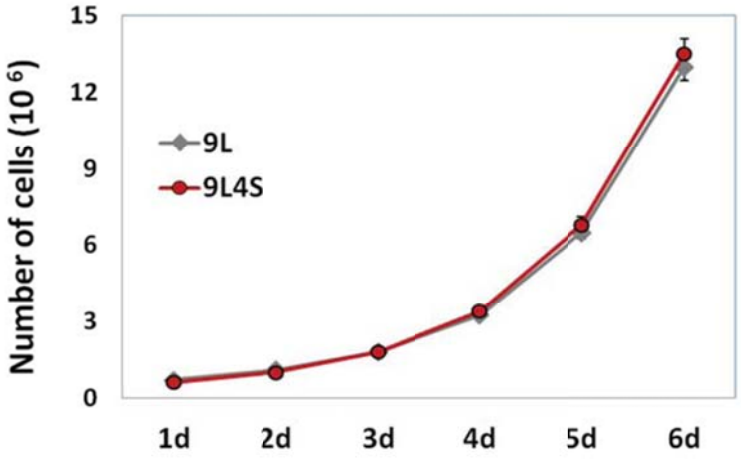

Figure 13: Graph depicting cell growth over a period of six days. The number of live cells growing on cell culture plates was measured daily for a period of 6 days. Error bars indicate ± standard deviation.

There was no significant difference between the cell viability of the 9L cells and the cell viability of the 9L4S cells over a period of 6 days (Figure 14). On average, the cell viabilities of 9L and 9L4S cells were between 96% and 98%. The average cell viability was always less than 100%, which signifies that some non-viable cells were always present in the cell culture plates.

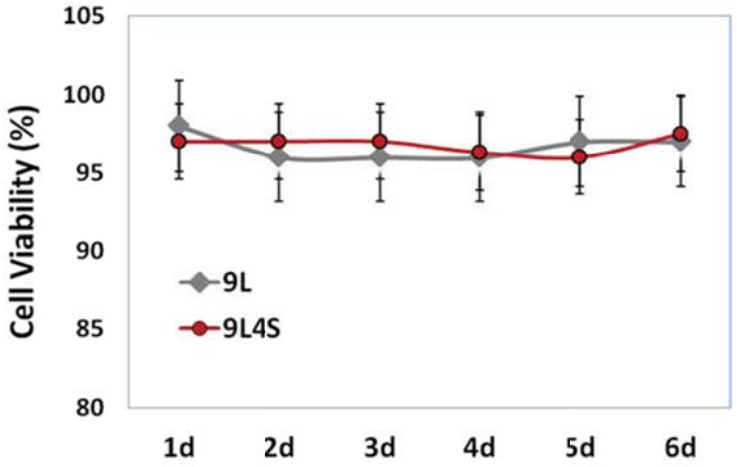

Figure 14: Graph depicting the change in cell viability over a period of six days. The cell viability of cells incubated with media with no iron supplement was calculated every day for 6 days. Cell viability is a measure of the number of cells that remain alive on a plate compared to the total number of cells on the plate. Error bars indicate ± standard deviation.

Iron is toxic to cells, so it is not surprising that when cells are incubated with increasing amounts of iron, the cell viability of the cells decreases, regardless of the cell line (Figure 15). Recall that 200 μM of iron is the concentration of iron used in the imaging experiments. When cells were cultured for three days in media containing 200 μM or less of iron, no difference was found between the cell viability of 9L cells and the cell viability of 9L4S cells. At an iron concentration of 400 μM, the cell viability of the 9L4S cells was greater than the cell viability of the 9L cells, suggesting that the 9L4S cells were better able to tolerate higher concentrations of iron.

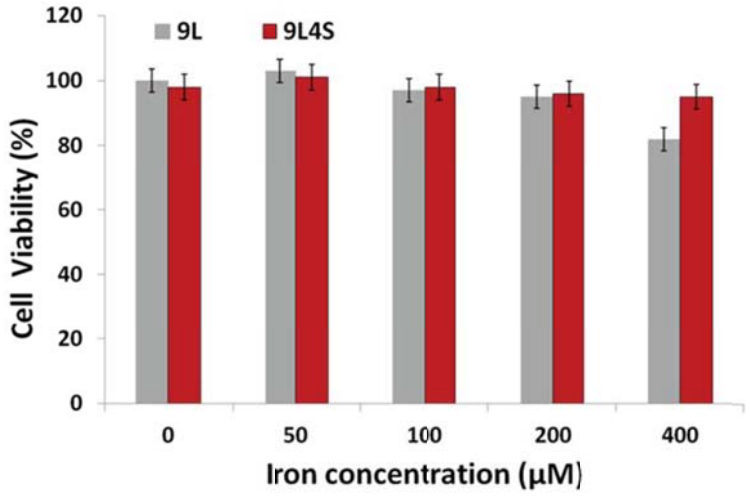

Figure 15: Graph depicting the effects of iron on cell viability. The cell viability of cells incubated with media supplemented with iron for three days was calculated. The concentration of iron in the media is graphed on the *x*-axis. Cell viability is a measure of the number of cells that remain alive on a plate after being cultured with iron for three days compared to the number of cells that remain alive on a separate plate after three days of not being cultured with iron. Error bars indicate ± standard deviation.

3.5 Discussion & Conclusion

The primary objective was to confirm whether the 9L4S clone that we had selected for future studies, which included animal studies, was in fact able to produce reproducible changes in image contrast, and our secondary objective was to test the hypothesis that 9L4S cells hold more iron than 9L cells. When we chose *mms6* as a gene with the potential to function as an MRI reporter gene, we based our decision on the fact that Mms6 binds iron in magnetotactic bacteria. We knew that as a recombinant protein, Mms6 could also be able to bind iron. Because iron is a negative contrast agent, cells that store greater amounts of iron should have a faster relaxation rate than cells that cannot store as much iron. MRI imaging of 9L4S and 9L cells showed that the relaxation rate of the 9L4S cells was indeed faster than the 9L cells. Since 9L4S cells express *mms6* and

have a faster relaxation rate than 9L cells, we had reason to believe that the changes in relaxation rates were accompanied by changes in intracellular iron. It is important to note that when 9L and 9L4S cells are incubated with iron in the range of 0 to 50 μM, the R_2 values of the 9L and 9L4S cells did not differ much (Figure 9). This is significant because when the 9L4S cells were used to establish an animal model (see Chapter 4), the cells were exposed to an iron pool, i.e. the iron in the blood, with significantly less than 50 μM of iron (64, 65). This topic will be revisited in Chapters 4.

We wanted to know whether the production of contrast we were able to detect on an MRI image could be due to Mms6 binding iron and thereby enhancing the iron storing capacity of the *mms6*-positive cells. Importantly, we were not so much interested in researching the specific mechanism by which Mms6 could potentially be affecting the uptake, storage, or transport of iron; we were mostly interested in detecting whether or not the changes in contrast could be correlated to changes in intracellular iron levels. The results of the Prussian blue staining, mass spectroscopy, and electron microscopy confirm that 9L4S cells take up more iron then 9L cells. According to the mass spectroscopy measurements, 9L4S cells can take up 2.8 times more iron than the 9L cells. The results of the imaging and iron studies are consistent with the hypothesis that the recombinant protein Mms6 enables cells to take up more iron than wild-type cells. The MTS assay and the Trypan blue dye exclusion assay led us to conclude that the cell viability and cell growth of the 9L4S cells were no different than the cell viability and cell growth of the 9L cells. The Trypan blue assay also showed that incubating cells with iron less than 200 μM of iron decreases the cell viability of both the 9L and 9L4S cells to the same extent. At an iron concentration of 400 μM, the cell viability of the 9L4S cells was greater than the cell viability of the 9L cells—perhaps the 9L4S cells were better able to tolerate higher concentrations due to the ability of Mms6 to bind iron.

With the MTS cell proliferation assay, we expected to see a small decrease in cell viability when the cells were cultured with iron; of course, the greater the concentration of iron supplemented in the culture medium and the more days the iron is left in the medium, the greater the toxic effects on the cells. These are exactly the results that we observed. The results were also consistent with what we had hypothesized: that 9L4S cells would be less sensitive to the iron than the 9L cells because the toxic effects of the iron on the 9L4S cells would be mitigated by Mms6. If Mms6 were able to bind and chelate the iron, in theory, it should prevent the iron from decreasing the cell viability.

The concern of genomic instability became more pronounced as we completed the work outlined in this chapter. We needed growing and dividing cells for our experiments, so we could not halt chromosomal instability by keeping the clones preserved in liquid nitrogen. As mentioned before, with every passage, cells become more unstable and may begin to produce phenotypic changes due to the instability. On occasion, we noticed that positive clones that had been passaged and imaged for many weeks began producing less image contrast, a phenomenon which we attribute to genomic instability. Our solution to this problem was to periodically image the clones to confirm that the MRI signal has not decreased. If it had, we discarded the cells and took a new batch from out of the liquid nitrogen.

CHAPTER 4

ESTABLISHMENT OF TUMORS COMPOSED OF POSITIVE CLONES IN AN ANIMAL MODEL AND MEASUREMENT OF THE MRI CONTRAST PRODUCED BY THE TUMORS

The ability of *mms6* to enhance the contrast produced by a particular cell is an ability that it must have in order for it to be considered an MRI reporter gene. With that in mind, we transfected cells with *mms6*, developed positive clones, and measured the T_2 relaxation time of one of those *mms6*-positive clones, 9L4S. The MRI results at both 3 T and 9.T showed that *in vitro*, 9L4S cells produced more contrast than 9L cells; however, the overall purpose of our project was to examine the possibility that *mms6* can be used as an MRI reporter gene *in vivo*. Based on the *in vitro* results, we then hypothesized that Mms6 may also enable 9L4S cells to produce more image contrast *in vivo* than 9L cells, which do not express *mms6*. To test our hypothesis, we established tumors with different amounts of 9L and 9L4S cells in two different strains of rats. Once the tumors were established, we imaged the tumors with MRI once a week for up to three weeks. We discovered that tumors that developed from 9L4S cells do produce more negative contrast than tumors developed from 9L tumors, but only when the tumors are small. We also confirmed that the tumors developed from 9L4S cells had more iron deposits than the tumors developed from 9L cells. Finally, we found that giving the rats iron supplementation (10 mg of iron per 200 g of body weight) decreased the difference between the relaxation rates of the two tumors.

4.1 Background

The final aim of our research was to determine whether *mms6* would enable 9L4S cells to produce more MRI image contrast *in vivo* than 9L cells. In order to image the cells *in vivo*, the cells had to be introduced into an animal. We chose rats as the animal we would be using for our research. A brief description of the use of rodents in biomedical research now follows:

4.1.1 Rodents in Biomedical Research

Mammalian animals are used in biomedical research because of their close proximity to humans in terms of genetics, anatomy, and physiology. Among other things, they are used to study diseases and medical conditions, to develop treatments and vaccines, to find cures, and to test medical procedures before they are used on humans. Although monkeys, dogs, cats, cows, sheep, and even pigs have been used for research purposes, the rodent is the most commonly and widely used animal. Rodents are small in size and easy to handle, so it is relatively inexpensive to purchase and house them. Rodents breed quickly so large populations of rodents can be created, making rodents readily available for research. In addition, inbreeding has led to the creation of genetically homogenous populations of rodents, which is an added benefit to researchers who want to execute a controlled experiment. Although mice are by far the most commonly used animal model in general, rats, guinea pigs, and hamsters have also been used in biomedical research.

4.2 Approach

4.2.1 Tumor Animal Model

At the cellular level, MRI reporter genes enable cells located inside a living organism to be visible via MRI. Because we wanted to determine whether *mms6* can be used as an MRI reporter gene *in vivo* and because we had confirmed that 9L4S cells have greater image contrast than 9L cells *in vitro*, we implanted 9L4S cells inside an animal to determine if 9L4S are also able to produce more contrast than 9L cells *in vivo*. In particular, we established tumors that grew out of inoculations of 9L and 9L4S cells. We chose to use a tumor model for a few reasons. For starters, it is a model created with established techniques. In addition, when cells form tumors, they stay together as a group. Together the cells can produce more contrast than they can apart, so the tumor is more likely to stand out in an MRI image from among the endogenous tissue which surrounds the tumor. As an added benefit, the location of the tumor could be controlled simply by grafting the cells at the exact location where we wanted the tumor to grow. Since we knew where we had implanted the cells, we were able to easily find the tumors during imaging.

To create a tumor model, a tumor composed of *mms6*-positive clones is established in an animal via injection of the clone at the desired location of tumor formation. Though we had several clones, we used 9L4S cells for tumor inoculations not only because 9L4S cells had the highest average relaxation rate *in vitro*, but also because 9L4S is an *mms6*-positive 9L clone. 9L cells and clones derived from 9L cells are tumorigenic. If they were not, 9L and 9L4S cells would not form tumors once they were grafted in an animal. 9L cells are a gliosarcoma cell line. Gliosarcoma is a rare type of glioma; and a glioma is a type of malignant brain tumor that arises when glial cells mutate and become cancerous. When 9L cells were selected as host cells for transfection with *mms6* at the start of the research project, 9L cells had already been used to grow brain and flank tumors (61, 73).

With all that in mind, we chose to begin our animal studies with the creation of a flank tumor animal model. Establishing subcutaneous flank tumors involved an easy and quick procedure whereby the animal were first anesthetized and then injected subcutaneously with a cell suspension into the flank. Both 9L and 9L4S cells were implanted into the flank of a single rat, with 9L cells on one side and 9L4S cells on the other, thereby reducing the total number of animals required for experimentation by half.

Our species of choice was rats. We chose rats over mice mainly because of their larger size. Bilateral injections were easier to perform because of the rat's larger size. According to the experimental guidelines to which we had to abide (refer to the Appendix, section A.2 Animal Use), animals had to be euthanized if a tumor grew too large relative to its body size. The rat's larger body size allowed tumors to grow larger before they hindered the rat's movements or affected the rat's health. At the time, we wanted to grow larger tumors because we thought that the larger tumors would produce better image contrast than the smaller tumors. In addition, larger tumors required additional time to grow, giving us the opportunity to track any changes in MRI contrast for a longer period of time. We also reasoned that small tumors would require a higher spatial resolution in order to be visible on an MRI image than larger tumors would require. We elected to work with male rats not only because they are less expensive to purchase but also because we were advised by an experienced colleague that male rats are easier to handle than female rats.

4.2.2 Iron Overload

In vitro, we found that 9L4S cells required supplemental iron in order to increase their average relaxation rate. We later discovered that under specific circumstances, tumors

that grew from inoculations with 9L4S cells, or 9L4S tumors, also had faster relaxation rates than tumors that grew from inoculation with 9L cells, or 9L tumors. In these experiments, the flank tumors were exposed only to the endogenous iron located inside the body of the rat. Serum iron concentrations of rats are very low compared with the supplemental iron concentrations of our *in vitro* experiments (64, 65). We hypothesized that if rats received an iron supplement, the difference between the average relaxation rate of 9L4S tumors and the average relaxation rate of 9L tumors would increase compared to the difference between their relaxation rates when rats were not given any iron supplement.

Iron overload in rats is often achieved via the administration of iron dextran. There are several methods used by other researchers to produce iron overload in rats using iron dextran. For instance, some researchers have administered i.p. (intraperitoneal) injections containing either 250 or 500 mg of iron per kilogram (kg) every other week for 22 weeks (a total of 900 mg of iron) (74, 75). Other researchers instead administered single doses containing 500 mg of iron per kg via i.v. (intravenous) or i.p. injections or 1,200 mg of iron per kg via s.c. (subcutaneous) injections (76-79). We chose to modify the experimental methods of a group of researchers who administered daily i.p. injections of 100 mg of iron per kg for seven day to male F344 rats (80, 81). Using their method, the serum iron levels in the blood were 1032.3± 209.68 μM (80). Based on a preliminary study, we found that the rats did not tolerate such high doses of iron for that number of days. We also found that the relaxation rates of 9L and 9L4S tumors were basically identical. We thus chose to modify their experimental method. We would inject only 50 mg of iron per kg for a period of five days.

The animals were tumor inoculated as normal and then given 9 days to grow. On day 9, the animals were hand held and given up to 10 mg of elemental iron per 200 g of body

weight. The iron dextran was injected i.p. once a day for five days. The iron dextran solution came in a concentration of 100 mg/ml, so we would have injected a 130 g rat with 65 µl of iron dextran solution. The injections were given for five days so that the tumors had several days to take up iron from the blood stream. Based on a preliminary study, we knew that if the tumors took up too much iron, the relaxation rates of the 9L and 9L4S tumors would be the same; so we waited 24 hr after the last injection to image the tumors. The rats were imaged by MRI on day 14.

4.2.3 In Vivo MRI

Once tumors were established in the rats, the tumors were given two weeks to grow before being imaged with MRI. The animals were then imaged once a week for up to three weeks. The animals were scanned in a Bruker 9.4 T small animal MRI scanner with a T_2-weighted spin echo sequence. To take advantage of magnetic susceptibility difference created by the iron, we could have used T_2*-weighted gradient echo imaging. Both types of imaging have been used for imaging iron oxide labeled cells (10, 49, 82). We chose to use a T_2-weighted spin echo sequence not only because the sequence can produce images with less image distortion and image artifacts (82), but also because we wanted to compare our imaging results to the results of a previously completed *magA* study (49). After we imaged our tumors, we used ParaVision 5.1, Bruker's imaging software, to calculate the T_2 relaxation times of the tumors. As with the *in vitro* imaging data, we converted the T_2 values to R_2 values and compared the average relaxation rates of the 9L tumors to the average relaxation rates of the 9L4S tumors.

4.2.4 *In Vitro* MRI

At 3 T and *in vitro*, when the cells were incubated for three days with 50 μM of iron, the percent change in the relaxation rates of 9L and 9L4S cells was modest, only 15.5%. The iron in the blood of a rat is less than 50 μM, so we initially wondered whether we would be able to detect any differences in the relaxation rates of 9L and 9L4S tumors even if the tumors were imaged at a higher magnetic field strength (9.4 T). To determine whether the percent change in the relaxation rates of 9L and 9L4S cells would be significantly bigger when imaged at 9.4T, the *in vitro* imaging study of 9L and 9L4S cell pellets was repeated. The cells were incubated for three days with only 40 μM of iron instead of 50 or 200 μM, and they were imaged at 9.4 T instead of at 3 T. In addition, to better mimic the conditions in the body of the rat, where the iron in the blood is replenished every time it eats, some of the cells were also incubated with 40 μM iron that was periodically replenished over the course of three days.

4.2.5 Western Blot Analysis

The rats were not given Zeocin, which was the antibiotic used to prevent *mms6*-negative cells from growing on cell culture plates containing 9L4S cells. Once the animals were inoculated with the cells, Zeocin would no longer maintain a pure cell line. After the cells were given a couple of weeks to replicate and form tumors and after the animals were imaged with MRI, we wanted to determine whether the tumor cells were still expressing *mms6*. Once the animal had been euthanized, whole flank tumors were excised. Western blotting was used to determine whether Mms6 was still present in the 9L4S tumor and to confirm that it was absent in the 9L tumor.

4.2.6 H&E Staining and Prussian Blue Staining

When the relaxation rates of the tumors had been measured, we found that the average relaxation rate of the 9L4S tumors was faster than the average relaxation rate of the 9L tumors under certain conditions. We then wanted to determine whether the difference in relaxation rates between the 9L tumors and 9L4S tumors coincided with a difference in their intracellular iron contents. We also wanted to compare the morphology of the two tumors. We accomplished both of these goals with histological staining. Immediately after their last imaging sessions, the rats were euthanized, and their tumors were excised, fixed, sectioned, and stained. The tissue sections were then either stained with hematoxylin–eosin (H&E) to observe the morphology of the tumor cells or with Prussian blue to observe the iron in the tumor cells.

4.3 Methods

4.3.1 Tumor Animal Model

We established flank tumor models in 5-7 week old male rats: 14 male RNU Rats (Crl:NIH-*Foxn1*^{rnu}) (Charles River, Wilmington, MA, USA) and 13 male F344 (SAS FISCH) Rats (F344/NCrl) (Charles River). First, 9L and 9L4S cells were collected from the cell culture plates and were each resuspended in 100 μl of PBS containing 10% Matrigel (BD Biosciences, San Jose, CA, USA). Rats were anesthetized by an intraperitoneal injection of ketamine (85 mg/kg)/xylazine (10 mg/kg). The hair on the lateral sides of the flank was shaved, and the injection site was disinfected with betadine and 70% alcohol. The cell solutions were then injected with a 23-gauge needle subcutaneously in the flank, immediately above the hind legs. All rats were tumor inoculated with 9L cells in the right flank and 9L4S cells in the left flank. 3 RNU rats

were tumor inoculated with 2×10^6 cells in each side of the flank, and another 3 RNU rats were tumor inoculated with 5×10^6 cells in each side of the flank. 8 RNU rats were tumor inoculated with 1×10^6 cells in each side of the flank. All 13 F344 rats were tumor inoculated with 1×10^6 9L cells in the right flank and 1×10^6 9L4S cells in the left flank. The animals were imaged with MRI for the first time two weeks later, after which time they were imaged with MRI once a week. The rats were imaged a maximum of three times.

4.3.2 Iron Overload

9 days after tumor inoculations, 4 of the F344 rats received 10 mg of elemental iron per 200 g of body weight in the form of i.p. iron dextran injections (Vedco, St. Joseph, MO, USA) every day for a period of five days. The last day they received iron injections occurred 13 days after tumor inoculations. Starting the next day, i.e. 2 weeks after tumor inoculations, the rats were imaged with MRI for four consecutive days.

4.3.3 *In Vivo* MRI at 9.4 T

After the rats were given 2, 3, or 4 weeks to grow, anesthesia was induced with 5% isoflurane/95% oxygen and was maintained with 1.5-2% isoflurane. The small animal Model 1025 Monitoring and Gating System (SAII, Stony Brook, NY, USA) was used to monitor heart rate, body temperature, and respiratory rate during imaging. Rats were imaged on a heated cradle in a 9.4 T Bruker BioSpec® 94/20 small animal scanner (Bruker). After localization, a set of high-resolution T_2*-weighted images were acquired for tumor delineation using fast low-angle shot (FLASH) with TE = 6.0 ms, TR = 50 ms, FOV = 256 mm × 256 mm, in-plane resolution = 88 micrometers (μm), and slice

thickness = 0.450 mm. To create a T_2-weighted image, an MSME spin echo sequence was applied with the following imaging parameters: TR = 4,000 ms, TE = 9.3-111.6 ms, Echoes: 12, FOV = 60 mm × 60 mm, in-plane resolution = 0.5 mm, and slice thickness = 1 mm. The image from the first echo was included in the figures as an anatomical map. Image processing and analysis were performed using MATLAB.

During imaging, enough slices of the tumor were obtained to span the entire length of the tumor. We collected data from each rat, one tumor at a time, as follows: using a software called ParaVision 5.1 (Bruker), we obtained the average T_2 value of each tumor slice and subsequently averaged those values to get the T_2 value of the whole tumor. The transverse relaxation times (T_2) are calculated by exponential fitting of a decay curve to the signal produced from the MSME sequence. Next, we averaged the T_2 values of the individual 9L4S tumors and averaged the T_2 values of the individual 9L tumors to obtain the average T_2 value of the 9L4S tumors and the average T_2 value of the 9L tumors. Finally, using Equation (24), the average T_2 values of the tumors were converted to average R_2 values of the tumors in Microsoft Excel 2010. The relaxation rates of the tumors were compared. The data are presented as means of the R_2 values of the tumors ± standard error of the means.

4.3.4 *In Vitro* MRI at 9.4 T

9L cells were seeded in 27 plates, and 9L4S cells were seeded in another 27 plates. For each cell line, 18 of the plates contained cell culture media supplemented with enough ferric citrate to make the concentration of iron in the media 40 μM. In the remaining 9 plates, the cell culture media contained no iron supplement. Out of the 18 plates that contained media with iron supplementation, the media in 9 of them was discarded and

replaced with fresh media containing 40 μM of iron every 12 hr. After three days in the incubator, the cells had grown to ~90-95% confluency in 100 mm plates. The culture media was removed from all the plates, and the cells were washed with PBS. To detach the cells, 1 ml of trypsin EDTA was added to each plate. After five min, 3 ml of cell culture medium was added to each plate. The 9 plates which had their cell culture media replaced every 12 hr were divided equally into 3 groups, 3 plates per group. The same was done with the 9 plates containing media with no iron supplementation and the 9 plates containing media with iron supplementation that was not replaced every 12 hr. The cells from each group were combined and put into separate 10 ml tubes. The cell solution was centrifuged for 5 min at 1,000 rpm. The supernatant was removed, and the cell pellets were resuspended in 1 ml of PBS and placed into separate 1.5 ml tubes. The cells were then given time to settle by gravity for two hr and 20 min at 4 °C. The cell pellets were imaged at 9.4 T.

For details about the 9.4 T MRI scanner and the imaging parameters, please refer to the methods section of Chapter 3, subsection 3.3.3 *In Vitro MRI at 9.4 T*. Once the T_2 values were measured, the transverse relaxation rates (R_2) of the cell pellets were calculated using Equation (24). In total, 18 samples were imaged at once. For both 9L and 9L4S, 3 samples of cells cultured with an iron supplement, 3 samples of cells cultured with an iron supplement that was replenished every 12 hr, 3 samples of cells cultured without an iron supplement. The data are presented as means of the R_2 values of the cell pellets ± standard error of the means.

4.3.5 Western Blot Analysis

T-PER Tissue Protein Extraction Reagent (Thermo Fisher Scientific) was used for the extraction of total protein from the tumor tissue. For details about the Western blot protocol, please refer to the methods section of Chapter 2, subsection 2.3.6 *Western Blot Analysis*.

4.3.6 H&E and Prussian Blue Staining

Immediately after the rats were scanned for the final time, the rats were euthanized with CO_2. Whole tumors were excised and submerged in an embedding matrix called Tissue-Tek™ CRYO-OCT Compound (Fisher Scientific, Suwanee, GA, USA). The compound was solidified and the tissue was snap frozen on dry ice. The tissues samples were then sectioned (8 μm) and fixed with ice-cold acetone. The tissue sections were then either stained with hematoxylin–eosin (H&E) or with Prussian blue. In the latter case, a Prussian blue staining kit (Ocean NanoTech, Springdale, AR, USA) was used and the manufacturer's instructions were followed. The tissue slices were examined under an Olympus BX51 inverted microscope.

4.3.7 Statistics

Statistical analyses were performed in Microsoft Excel 2010. An unpaired, two-tailed Student's t-test was used to calculate a *p*-value. A *p*-value of less than 0.05 was considered to be statistically significant.

4.4 Results

RNU rats were tumor inoculated with 1×10^6, 2×10^6, or 5×10^6 cells on each side of the flank, with 9L cells on one side and 9L4S cells on the other. The cells were allowed to grow for three weeks before being imaged in a 9.4 T MRI scanner. The relaxation rates of the tumors were measured and averaged (Figure 16). The average relaxation rates of the tumors decreased as the number of cells used to inoculate the RNU rats increased. Because of the iron, we had expected the R_2 value of the tumors composed of *mms6*-positive cells, which we will refer to as 9L4S tumors, to be larger than the R_2 value of tumors composed of the control cells, which we will refer to as the 9L tumors. Out of the three cell numbers, only rats that were inoculated with 1×10^6 cells had 9L4S tumor with larger R_2 values than the 9L tumors.

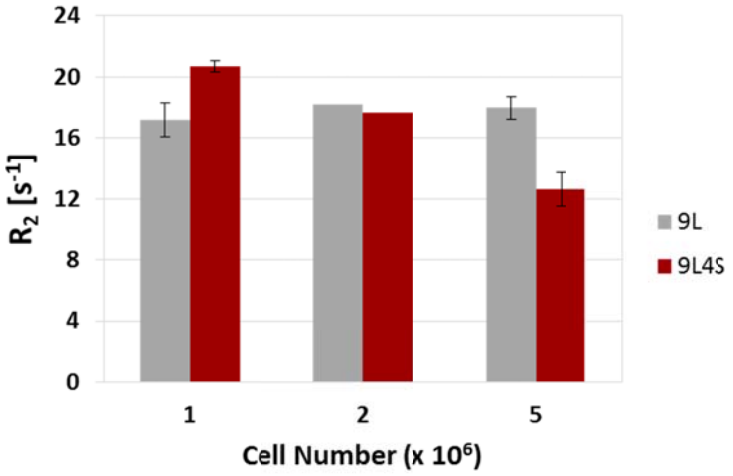

Figure 16: Relaxation rates (R_2) of flank tumors measured 3 weeks after tumor inoculations with varying numbers of cells. RNU rats were tumor inoculated bilaterally with 1×10^6, 2×10^6, or 5×10^6 9L cells and 9L4S cells in the flank. The tumors were imaged *in situ* three weeks later in a 9.4 T MRI scanner. Error bars indicate ± standard error of the means. N = 3.

RNU rats were once again tumor inoculated, but this time, all the rats were inoculated with 2×10^6 cells. The tumors were given two weeks to grown, and then they were imaged in a 9.4 T MRI scanner once a week for three weeks. The relaxation rates of the tumors were measured and averaged (Figure 17). The average R_2 values of both the 9L4S and 9L tumors decreased with every passing week. The same general trend was found when the same experiment was repeated using 1×10^6 and 5×10^6 cells to tumor inoculate RNU rats (data not shown). The R_2 values of the 9L4S tumors were smaller than the R_2 values of the 9L tumors. These results did not support our hypothesis that 9L4S tumors would have faster relaxation rates than 9L tumors.

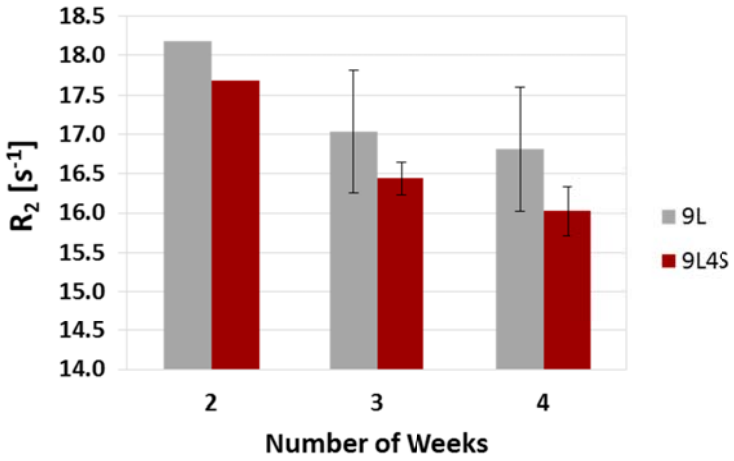

Figure 17: Relaxation rates (R_2) of flank tumors measured over a period of three weeks after tumor inoculations with 2×10^6 cells. RNU rats were tumor inoculated bilaterally with 2×10^6 9L cells and 9L4S cells in the flank. The tumors were imaged *in situ* two, three, and four weeks later in a 9.4 T MRI scanner. Error bars indicate ± standard error of the means. N = 3.

Like before, an additional 5 RNU rats were tumor inoculated with 1×10^6 cells, with 9L cells on one side of the flank and 9L4S cells on the other; however, the rats were imaged in a 9.4 T MRI scanner twice, 2 and 3 weeks after tumor inoculations, instead of once,

after 3 weeks. The relaxation rates of the tumors were measured and averaged (Figure 18g). Like before, the average R_2 value of the 9L4S tumors was larger than the average R_2 value of the control tumors at three weeks ($p = 0.031$). At two weeks, the average R_2 value of the 9L4S tumors were also larger ($p = 0.0004$). An R_2 map of one of the rats was also generated to observe the R_2 values across a single slice of the tumor (Figure 18a-f). The relaxation rates at the border of the tumor tended to be faster than the relaxation rates in the center of the tumor.

To determine whether similar results would be obtained if a different strain of rat was used to create a tumor animal model, the same experiment was repeated with F344 rats. The relaxation rates of the tumors were measured and averaged (Figure 19g). The average R_2 value of the 9L4S tumors was also greater than the R_2 values of the 9L tumors at both 2 and 3 weeks after tumor inoculations (both with $p < 0.0001$). These results support our hypothesis that 9L4S tumors have faster relaxation rates than 9L tumors. An R_2 map of one of the rats was also generated (Figure 19a-f). As in the RNU rats, the relaxation rates at the border of the tumor were generally faster than the relaxation rates in the center of the tumor.

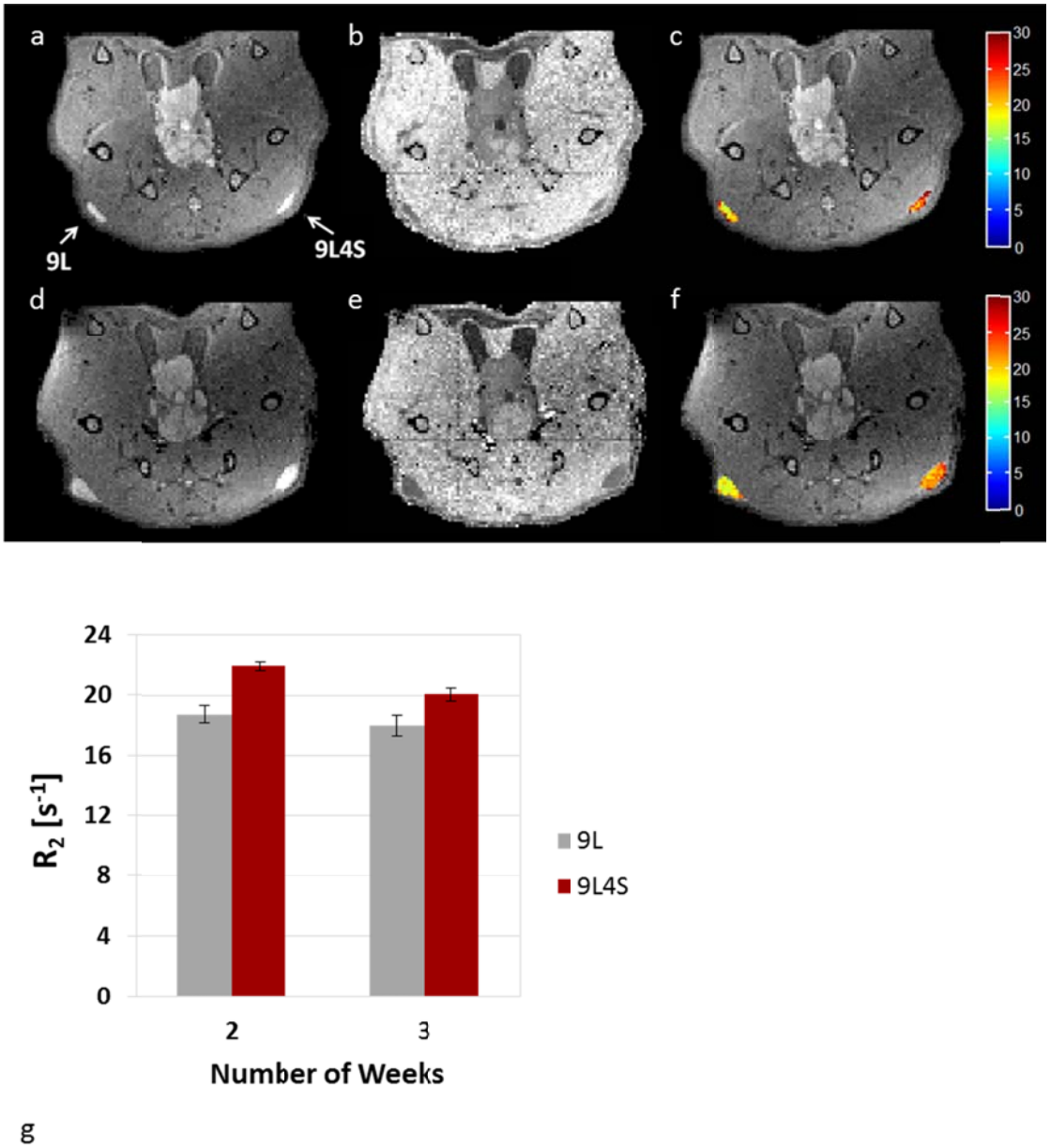

Figure 18: Relaxation rates (R_2) of flank tumors in RNU rats measured 2 and 3 weeks after tumor inoculations with 1×10^6 cells. RNU rats were tumor inoculated bilaterally with 1×10^6 9L cells and 9L4S cells in the flank, as indicated by the arrows in (a). The tumors were imaged *in situ* three weeks later in a 9.4 T MRI scanner. (a, b, c) Transverse MRI images of a single representative RNU rat two weeks post tumor inoculation. (d, e, f) Transverse MRI images of the same representative RNU rat three weeks post tumor inoculation. (a, d) Anatomical maps. (b, e) Transverse relaxation rate (R_2) maps. (c, f) R_2 maps of flank tumors overlaid on anatomical images. Color bar indicates R_2 values in the range of 0 to 30 s^{-1}. (g) Graph of R_2 measurements of flank tumors 2 and 3 weeks after tumors inoculation. N = 8. Error bars indicate ± standard error of the means.

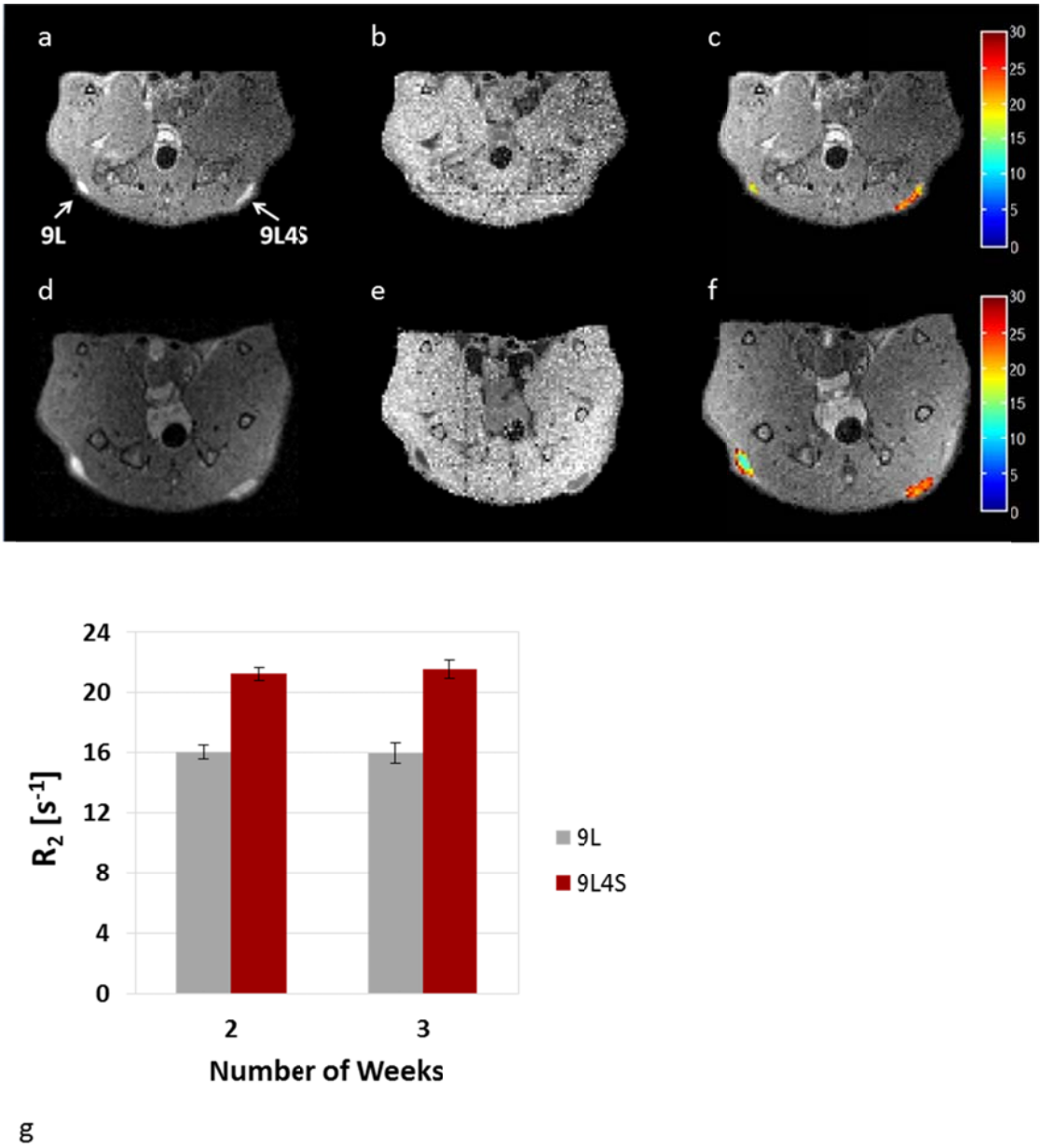

Figure 19: Relaxation rates (R_2) of flank tumors in F344 rats measured 2 and 3 weeks after tumor inoculations with 1×10^6 cells. Nude rats were tumor inoculated bilaterally with 1×10^6 9L cells and 9L4S cells in the flank, as indicated by the arrows in (a). The tumors were imaged *in situ* three weeks later in a 9.4 T MRI scanner. (a, b, c) Transverse MRI images of a single representative F344 rat two weeks post tumor inoculation. (d, e, f) Transverse MRI images of the same representative F344 rat three weeks post tumor inoculation. (a, d) Anatomical maps. (b, e) Transverse relaxation rate (R_2) maps. (c, f) R_2 maps of flank tumors overlaid on anatomical images. Color bar indicates R_2 values in the range of 0 to 30 s^{-1}. (g) Graph of R_2 measurements of flank tumors 2 and 3 weeks after tumors inoculation. N = 9. Error bars indicate ± standard error of the means.

After three weeks, immediately after the end of the imaging session, the tumors were excised and prepared for analysis. Western blot analysis confirmed that the 9L4S tumors were expressing the *mms6* gene as well as the Mms6 protein (Figure 20).

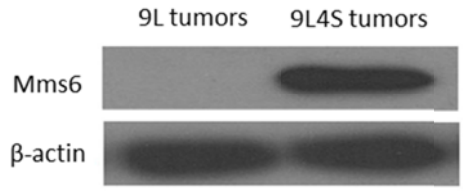

Figure 20: Analysis of Mms6 expression in 9L4S and 9L tumors. Western blot analysis of Mms6 protein expression in tumors that grew from tumor inoculations of 9L cells and 9L4S cells. A dark band indicates the presence of Mms6 or β-actin. β-actin was used as a loading control.

Staining fixed, whole cells with an H&E stain revealed no noticeable differences in cell morphology nor any signs of pathology (Figure 21a). To determine whether the 9L4S tumors contained more intracellular iron than 9L tumors, fixed, whole cells were stained with Prussian blue. The 9L4S tumor cells had more blue deposits, an indication of the presence of iron, than the 9L tumor cells (Figure 21b). In the RNU rats, tumors derived from inoculations with 5×10^6 cells were also prepared for histological analysis. After Prussian blue staining, no difference was observed between the number of blue deposits in 9L tumor cells and the number of blue deposits in 9L4S tumor cells (images not shown). Together, the imaging results of tumors derived from tumor inoculations with 1×10^6 cells and the Prussian blue staining results were consistent with the hypothesis that 9L4S tumors take up more iron and have faster relaxation rates than 9L4S tumors.

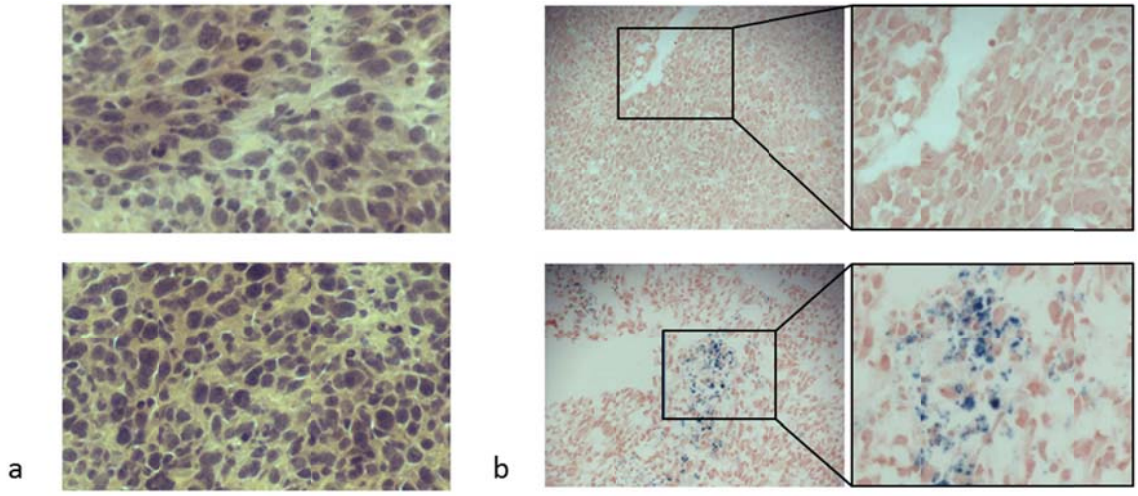

Figure 21: Histological analysis of 9L and 9L4S tumors. F344 rats were tumor inoculated bilaterally with 9L cells and 9L4S cells in the flank. The tumors were given time to grow before being excised. (a) Histologic sections stained with H&E showing the morphology of tumors collected 3 weeks after tumor inoculations. (c) Prussian blue staining showing the iron accumulation in tumor tissue collected at three weeks. The color blue indicates the presence of iron. 20X magnification.

To determine whether giving the rats iron supplementation would increase the difference in relaxation rates of the 9L and 9L4S tumors, F344 rats were injected with iron for five consecutive days. The rats were then imaged once a day for the next four days. Although the average R_2 values of the 9L4S tumors were greater than the average R_2 values of the 9L tumors, there was no statistical difference between the relaxation rates of the tumors on any of the four days (Figure 22). The iron does seem to have increased the relaxation rates of both tumors; the relaxation rates of the 9L and 9L4S tumors increased significantly compared to their relaxation rates when no iron supplementation was administered.

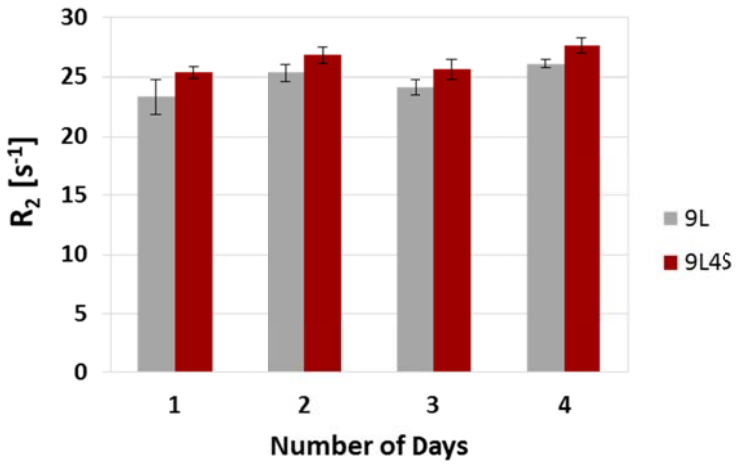

Figure 22: Relaxation rates (R_2) of flank tumors in rats that received i.p. iron injections. F344 rats were tumor inoculated bilaterally with 1×10^6 9L cells and 9L4S cells in the flank. The tumors were imaged *in situ* two weeks later in a 9.4 T MRI scanner. For five consecutive days prior to the first day of imaging, the rats received i.p. iron injections. The number of days following the final iron injection is graphed on the *y*-axis axis. N = 4. Error bars indicate ± standard error of the means.

In the *in vitro* experiments on 9L and 9L4S cells described in Chapter 3, culture media containing a given concentration of iron was added to the cell culture plates when the cells were first seeded. Afterwards, the media was not replaced nor was more iron added to it. In contrast, in the body of a rat, the iron in the blood and tissues to which the 9L4S and 9L tumors are exposed is replenished each time the animal feeds. To determine whether the relaxation rates of the cells would change if the cell culture media was replaced periodically with fresh culture media containing the same concentration of iron as the original media, cells were incubated for three days with media that was replaced every 12 hr. For comparison, cells were also incubated for three days with media that was not replaced. Because the iron concentration in blood and tissues of a rat is lower than 50 μM (64, 65), cells were cultured with a fraction of the iron used in almost all of the previous *in vitro* experiments. After the three days had passed, the relaxation rates of the cell pellets were measured and averaged (Figure 23). When cultured in media containing

40 μM of iron, the average relaxation rate of 9L4S cells was 10.3% greater than the average relaxation rate of 9L cells (p = 0.0043). When cultured in media containing 40 μM of iron that was replaced every 12 hr, the average relaxation rate of 9L4S cells was 20.0% greater than the average relaxation rate of 9L cells (p = 0.0002). On average, replenishing the iron every 12 hr increased the relaxation rates of 9L cells by 1.9% (p = 0.37) and increased the relaxation rates of 9L4S cells by 10.9% (p = 0.0008). These results are consistent with the hypothesis that at low iron concentrations, 9L4S cells are able to take up more iron if the concentration of iron in the extracellular iron pool is replenished periodically than if it is not replenished.

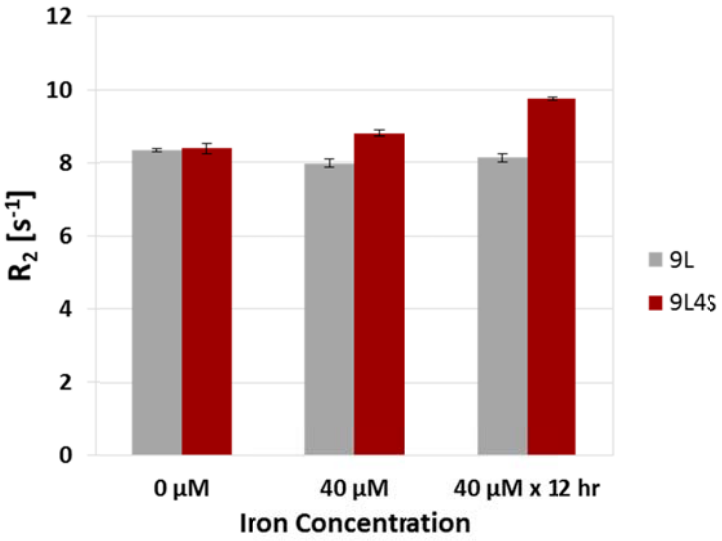

Figure 23: Relaxation rates (R_2) of cell pellets incubated with media that was replenished every 12 hours. 9L and 9L4S cells were imaged at 3 T after being cultured for three days. Fresh culture media containing either 0 or 40 μM of iron was added to the cells when they were first seeded. During the three days that followed, the media was either never replaced or was replaced every 12 hr with media containing the same concentration of iron as the media contained when the cells were seeded. N = 3. Error bars indicate ± standard error of the means.

4.5 Discussion & Conclusion

9L and 9L4S cells were used to tumor inoculate rats in the flank, with 9L cells injected into the right flank and 9L4S cells injected into the right flank. After allowing the cells to replicate for two weeks, the resulting tumors were imaged with MRI at 9.4 T and their relaxation rates were calculated. They were also imaged three and four weeks after tumor inoculations. When RNU rats were tumor inoculated with 1×10^6, 2×10^6, or 5×10^6 cells on each side of the flank; in any given week, rats that had been inoculated with more cells not only had tumors with slower relaxation rates, they also had larger flank tumors. For any of the three cell numbers used for tumor inoculation, with every passing week, the relaxation rates of the tumors also decreased. With every passing week, the tumors also got larger. Based on these results, we concluded that as tumors got larger, their relaxation rates decreased.

We had hypothesized that 9L4S tumors would have faster relaxation rates than 9L tumors because 9L4S cells had faster relaxation rates than 9L cells *in vitro*. Interestingly, only RNU rats that had been inoculated with 1×10^6 cells had 9L4S tumors with faster relaxation rates than 9L tumors. This was the case at both 2 and 3 weeks after tumor inoculations. RNU rats are immunodeficient, so the tumors were able to grow larger in a shorter period of time. When we discovered that the relaxation rates were affected by tumor size and that 9L4S tumors only had faster relaxation rates than 9L tumors when they were small, we chose to work with a different rat strain. We chose to work with F344 rats because another group of researchers had successfully used F344 rats to establish flank tumor models (61). When we injected the F344 rats with 1×10^6 cells, at 2 and 3 weeks, like the RNU rats, the 9L4S tumors had faster relaxation rates than 9L tumors. Furthermore, the difference between the average relaxation rate of the 9L4S

tumors and the average relaxation rate of the 9L tumors in the F344 rats was larger than the difference between the two average relaxation rates in the RNU rats.

In the case of the F344 rats that had been inoculated with 1×10^6 cells, Western blot analysis confirmed that 9L4S tumors expressed *mms6* and verified that 9L tumors did not express *mms6*. Prussian blue staining of tumors from the same rats showed that 9L4S tumors had more iron than 9L tumors. In contrast, after Prussian blue staining, we did not detect a difference in the levels of intracellular iron between the 9L tumors and the 9L4S tumors of RNU rats that had been inoculated with 2×10^6 cells These results support our hypothesis that 9L4S tumors have faster relaxation rates and more intracellular iron than 9L tumors, although the results suggest that this is only true when the tumors are small.

Though small 9L4S tumors had a faster relaxation rate than 9L tumors, we wondered whether giving the rats an iron supplement would increase the difference between the average relaxation rate of the 9L4S cell and the average relaxation rate of the 9L cells. We considered that in the body of the rat the serum blood iron concentration is less than 50 μM (64, 65), whereas *in vitro*, the biggest difference between the relaxation rate of 9L and 9L4S cells occurred at 200 μM. We hypothesized that that the 9L4S cells would be able to take up more iron if the iron in the local endogenous iron pools was increased. To test this hypothesis, the rats were given iron injections; however no difference in the relaxation rates of the 9L and 9L4S tumors were detected. We propose that when the animals were given iron, too much iron was administered and both the 9L and 9L4S tumors were saturated with iron, so much so that no difference in relaxation rates could be detected.

When the cells were imaged at 3 T *in vitro* for three days with 50 μM of iron, the difference between the average relaxation rate of the 9L cells and the average relaxation

rate of the 9L4S cells was only 15.5%. At 9.4 T, when the cell were imaged *in vitro* for three days with only 40 μM of iron, the difference between the average relaxation rates dropped to 10.3%. In contrast, the largest difference between the average relaxation rate of the 9L4S tumors and the average relaxation rate of the 9L tumors was 16.9% in the RNU rats and 34.9% in the F344 rat. The differences between the *in vitro* and *in vivo* results are most likely due to differences in how and where the cells grew over the course of the experiment. During the *in vitro* experiments, the clonal cells grew in a monolayer for three days with media that had been supplemented with iron but that was not replenished over the course of the three days. In contrast, *in vivo*, the cells grew into a tumor, which is 3D, for at least a couple of weeks; and each time the animal fed, the iron in its body was replenished. Unlike cells growing in cell culture dishes, the tumors became less homogenous over time because tumors activate an immune response as well as angiogenesis, evidence of which we found when we excised the tumors and saw the blood vessels that supplied the tumors with serum iron. As tumors grow, they also begin to necrotize. The heterogeneity of the cells was apparent on the MRI images. The imaging results showed that both the 9L and 9L4S tumors had hypointense and hyperintense regions visible on the same slice.

Out of all these differences between the *in vitro* and *in vivo* growth conditions, we tested whether replenishing the 40 μM of iron in the growth media would affect the relaxation rates of the cells. When we replaced the growth media every 12 hours, the difference between the average relaxation rate of the 9L4S cells and the average relaxation rate of the 9L cells was 19.9% compared to a difference of only 10.3% when the media was not replenished. This suggests that replenishing the iron in the pool from which the cells take up iron increases the difference between the relaxation rates of the 9L and 9L4S cells. Interestingly, the average relaxation rate of the 9L cells was almost completely unaffected by replenishing the media. Based on the imaging studies and intracellular iron

measurements presented in Chapter 3, these results suggest that when 9L4S cells have access to iron that is replenished periodically, the 9L4S cells can take up more iron and thus have faster relaxation rates than 9L cells. Though we did not examine this line of study any further, perhaps there is a concentration of iron that is high enough so that even if it was replenished, 9L4S cells would not be able to take up any more iron and so its relaxation rate would not change.

After imaging the animals and looking at the R_2 maps, we noticed a trend: the relaxation rates on the edge of the tumor tended to be faster than the relaxation rates in the central part of the tumor (Figure 19f). This suggests that the cells do not take up iron uniformly. Perhaps the iron is not taken up uniformly because the intercellular iron pool is not evenly distributed throughout the tumor. This is likely considering tumors often have neither uniform vasculature nor equal perfusion of intercellular fluid (83-85). To compare the relaxation rates of heterogeneous tumors, we had to assume that on average, 9L and 9L4S tumors developed similar vasculature and intercellular perfusion. If both tumors have the same degree of inhomogeneity, then the average relaxation rate of the 9L4S tumor is comparable to the average relaxation rate of the 9L tumor.

CHAPTER 5

CONCLUSION AND FUTURE DIRECTIONS

The project described in this dissertation is in the field of molecular imaging with MRI. Since we wanted to study MRI reporter genes, the project began by looking for genes that expressed a protein whose function might lead to the production of contrast in an MRI image. A literature review revealed that several genes had already been tested *in vivo*, *in vitro*, or both and thus might be good candidates for our molecular imaging project. These genes include β-galactosidase, tyrosinase, LRP, ferritin, and *magA* (5, 9, 10, 49, 86-88). *magA*, a gene native to magnetotactic bacteria, was the first gene we selected for our research because we were interested in continuing the work pioneered in our lab, work which produced evidence that *magA* could be used in an imaging study requiring an MRI reporter gene. The *magA* protein, MagA, was considered a putative iron transporter. Due to the unique magnetic properties of magnetotactic bacteria, we then considered other genes native to magnetotactic bacteria. In the end, we selected two magnetotactic bacterial genes for use in our research, *magA* and *mms6*. We originally chose *mms6* for our studies for two reasons. First, since previous studies of Mms6 showed that the protein could bind iron in the bacteria, we knew that mammalian cells transfected with *mms6* would express a recombinant protein that might be able to bind iron in the foreign intracellular environment of the mammalian cell. Based on the knowledge, we hypothesized that Mms6 would enhance the cells' iron storing abilities. Second, if Mms6 could increase the amount of intracellular iron, then we could co-transfect a cell line with both *magA* and *mms6*. In those cells, we hypothesized, MagA would transport iron into the cells, and Mms6 would bind the iron as it was being taken up by the cells. With the proteins working synergistically, cells expressing both genes would contain an even

greater amount of intracellular iron, more than the host cells and more than any cell line transfected with just one of the two genes. Importantly, we expected any increase in intracellular iron to correlate with an increase in MRI contrast.

The principle objective of the work described in this dissertation was to determine if cells transfected with the genes *mms6* or *magA* have more MRI image contrast than the wild-type cells. To compare the image contrast of the cells, we measured their relaxation rates. We hypothesized that *mms6*-positive and *magA*-positive clones would have faster relaxation rates than wild-type cells. First, we engineered several dozen *mms6*-positive and *magA*-positive single cell clones. After we measured the contrast produced by the clones *in vitro*, we found that the difference between the relaxation rates of *magA*-positive clones and wild-type cells was not statistically significant. In contrast, *mms6*-positive clones had faster relaxation rates than wild-type cells, but only when the cells were cultured with iron supplemented cell culture media. The clone that was able to produce the most image contrast, an *mms6*-positive clone named 9L4S, was selected for further study (Aim 1, Chapter 2). Because iron is a negative contrast agent and because we knew Mms6 binds iron in magnetotactic bacteria, we then hypothesized that the enhanced contrast produced by 9L4S cells might be due to an increase in intracellular iron uptake. Prussian blue staining, electron microscopy, and optical emission spectrometry provided evidence to support our hypothesis (Aim 2, Chapter 3). Because 9L4S cells had faster relaxation rates than 9L cells *in vitro*, we hypothesized that 9L4S cells would have a faster relaxation rate than 9L cells *in vivo*. Rats were tumor inoculated with 9L cells on the right flank and 9L4S cells on the right flank. Without requiring any exogenous iron supplement, MRI imaging showed that small but not large 9L4S tumors had faster relaxation rates than 9L tumors at both two and three weeks after tumor inoculations and in both RNU and F344 rats. Because of the increased intracellular iron found in 9L4S cells cultured with iron supplemented media *in vitro*, we hypothesized that

9L4S tumors would also have more intracellular iron than 9L tumors. Supporting our hypothesis, Prussian blue staining of the tumors showed that 9L4S tumors, which had the faster relaxation rates, had more iron deposits than the 9L tumors, which had the slower relaxation rates (Aim 3, Chapter 4). Taken together, the results obtained in the experiments described in Chapters 2-4 support the hypothesis that 9L4S cells are able to take up more iron because they express *mms6* and because of the iron, 9L4S cells have a faster average relaxation rate.

In molecular biology, recombinant DNA technology comprises a variety of laboratory techniques each used to manipulate DNA (89). Using these standard techniques, cells can be engineered to express any gene of one's choosing. A cell is engineered to express a gene of interest in the hopes of giving that cell a novel trait or phenotype that it does not naturally possess. In the work presented in this dissertation, *magA* and *mms6* were the genes whose putative functions in the magnetotactic bacteria made us consider them as potential iron-based MRI reporter genes (Figure 24). Even though the intracellular environment of the bacteria is distinct from that of the mammalian cell, 9L4S cell still gained a new phenotype, the ability to store more iron. Because it is a negative contrast agent, the iron altered the magnetization of the 9L4S cells such that they stood out from among the surrounding tissue on a T_2-weighted MRI image.

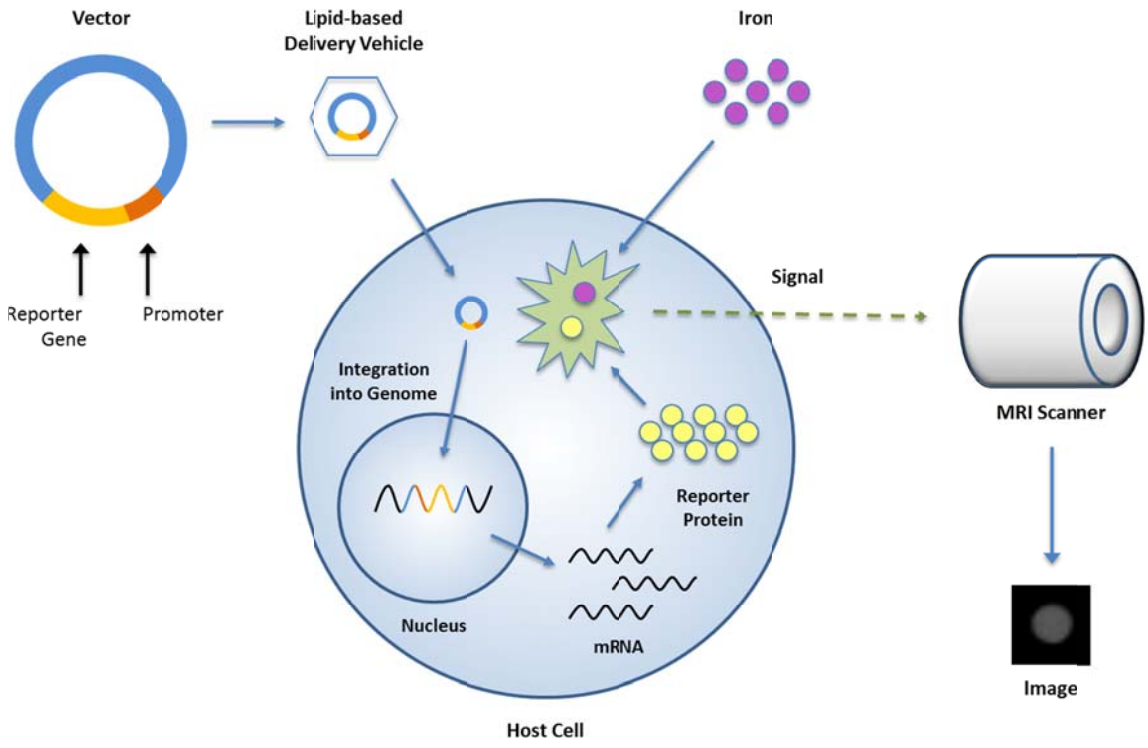

Figure 24: Schematic of molecular cloning and gene expression of an iron-based MRI reporter gene followed by imaging with MRI. The DNA reporter gene construct, which consists of the MRI reporter gene and its regulatory sequences, is inserted in a vector. A lipid-based delivery method is used to transfect a host cell with the gene. The gene is transcribed into mRNA, and mRNA is translated into the reporter protein. In the case of Mms6, though the mechanism is not known, host cells expressing the protein Mms6 contain increased levels of intracellular iron. Because iron is a negative contrast agent, it acts as the reporter probe. During an MRI scan, the presence of the reporter probe affects the NMR signal emitted by nearby protons in such a way that the image contrast of a group of cells expressing the MRI reporter gene is enhanced.

Showing that 9L4S tumors had a faster average relaxation rate than 9L tumors is evidence that *mms6* encodes a protein capable of enhancing the MRI image contrast of cells expressing *mms6 in vivo*. It thus follows that the work presented in this dissertation has established that *mms6* is an MRI reporter gene. In addition to *magA*, whose function as an MRI reporter gene is now questionable, as far as we know, *mms6* is the second MRI reporter gene native only to bacteria and not to rodents or humans. This is noteworthy

because being a bacterial gene gives *mms6* an advantage over other reporter genes because reporter genes work best if they are not naturally expressed in the organism being studied.

Even though we have labeled *mms6* as an MRI reporter gene based solely on the fact that cells expressing *mms6* have faster relaxation rates than wild type cells, *mms6* should be evaluated to gauge how useful it will be in more sophisticated studies. In the studies presented in this research, the 9L4S cells were always expressing *mms6* and we knew exactly where to find them. To evaluate whether it can significantly increase the relaxation rates of cells when *mms6* is not constitutively expressed, *mms6* expression should be made dependent on the presence or absence of a particular molecular event. To detect a very specific molecular change, the experimental design would have to be sophisticated (6), which might prove to be a challenge; however, a sophisticated study that resulted in *mms6* decreasing the relaxation rates of cells would substantiate the claim that *mms6* is an MRI reporter gene. In addition, *mms6* can be tested in a system where the cells of interest migrate to determine whether *mms6* expression in migrating cells allows for the visualization of those cells. This last example may turn out to be a challenge because visualization of a small number of cells with MRI is difficult. One thing is clear, the more negative contrast *mms6* is able to generate *in vivo*, the better a reporter gene it has the potential to be.

Even before a more sophisticated approach is used, a few other experiments could be executed that would shed light on some unknowns. For starters, using a constitutively active vector like we have done leaves room for doubt about whether it is actually *mms6* causing the changes in relaxation rates and intracellular iron levels that we observed. These changes could have also been caused by a mutation brought about by the random insertion of the gene into the host cell's genome. Because we created many clones which

all showed some change in relaxation rate, the chances that it was not *mms6* that brought about the chances we observed in our experiments is unlikely. Regardless, it would be nice to know with certainty. To confirm that *mms6* expression causes cells to uptake more iron and increases their relaxation rates, *mms6* could be cloned into an expression vector containing a simple inducible promoter. By turning off gene expression and observing that the changes in intracellular iron and relaxation rates no longer occur, the function of *mms6* as an MRI reporter gene would be validated. As another potential experiment, it would be interesting to determine whether recombinant protein Mms6 binds iron like Mms6 does in the magnetotactic bacteria. Immobilized Metal Affinity Chromatography could potentially be used to both isolate the recombinant protein (which contains a His-tag) and to examine whether Mms6 binds iron. As a final experiment, the animal studies could be repeated using a range of different cell numbers to try and determine how large the tumor must be before the relaxation rate of the 9L4S is slower than the relaxation rate of the 9L4S tumor.

As an iron-based MRI reporter gene, *mms6* comes with several limitations. Even though *mms6* altered the image contrast produced by subcutaneous *mms6*-positive tumors, it should be pointed out that *mms6*-positive cells would be less likely to stand out if they were located in an inhomogeneous tissue such as the abdomen. Even if *mms6*-positive cells were growing in a homogenous tissue, imaging of those cells using MRI signifies that detection of just a few cells may be difficult. We successfully detected differences in the MRI signal produced by *mms6*-positive cells, but the MRI signal was produced by a large grouping of cells that formed tumors that were at least 1.2 mm across in any dimension. Furthermore, our *in vivo* results suggest that there is also an upper threshold above which *mms6*-positive cells no longer have faster relaxation rates than control cells. In practice, perhaps this fact can somehow be used as an advantage. Regardless of the number of cells being imaged, *mms6*-positive cells need to have access to an iron pool in

order to function as an MRI reporter gene. In our animal studies, we saw evidence of angiogenesis in the dissected tumors, so we presume that the iron taken up by the tumor cells came from the blood supply. Our *in vitro* data leads us to believe that the iron pool would require a minimum amount of iron per unit volume in order to decrease the relaxation rate of the local *mms6*-positive cell population. Our *in vivo* data leads us to believe that the iron pool would not need to be highly concentrated with iron as long as the iron was periodically replenished. Once the cells were ready to be imaged, the detection of iron using MRI is usually limited to T2/T2*-weighted MRI imaging. In short, an *mms6*-based MRI reporter is best suited for the study of a group of cells growing in homogenous tissue with access to an iron supply.

Though today MRI is mostly used in the clinical setting to detect and locate tumors, MRI may one day help visualize the expression and activity of various molecules, cells, and biological processes (90). Although still in the early stages of research and development, MRI reporter genes have the potential to become invaluable tools, capable of modulating NMR signal in response to biological events at the molecular level. We hope our research contributes to the field of molecular MRI by getting us one step closer to discovering a valuable and versatile MRI reporter gene.

APPENDIX

A.1. Biosafety

Because we worked with mammalian cell lines, which can potentially carry bloodborne pathogens, the research protocols presented in this dissertation were reviewed and approved by the Emory Health and Safety Office (EHSO) before any work with recombinant genes and proteins commenced. The experiments were conducted in a biosafety level II laboratory at Emory University and universal biosafety precautions were used.

A.2. Animal Use

Because we worked with animals, the research protocols presented in this dissertation were reviewed and approved by Emory University's Institutional Animal Care and Use Committee (IACUC) before any work with the animals began. The experiments were conducted in an animal biosafety level II procedure room in an Emory University animal facility. As part of the IACUC approval process, we reduced the number of animal that were used in our research as much as possible and refined the proposed methods to limit any foreseeable discomfort, distress, pain, and injury experienced by the animals.

REFERENCES

1. Kircher MF, Gambhir SS, Grimm J. Noninvasive Cell-Tracking Methods. Nature Reviews Clinical Oncology. 2011;8(11):677-88.

2. Kang JH, Chung J-K. Molecular-Genetic Imaging Based on Reporter Gene Expression. Journal of Nuclear Medicine. 2008;49(Supplement 2):164S-79S.

3. Lee S-W, Lee S-H, Biswal S. Magnetic Resonance Reporter Gene Imaging. Theranostics. 2012;2(4):403-12.

4. Gilad AA, Jr. PTW, Zijl PCMv, Bulte JWM. Developing MR Reporter Genes: Promises and Pitfalls. NMR in Biomedicine. 2007;20(3):275-90.

5. Gilad AA, McMahon MT, Walczak P, Jr. PTW, Raman V, Laarhoven HWMv, et al. Artificial Reporter Gene Providing MRI Contrast Based on Proton Exchange. Nature Biotechnology. 2007;25(2):217-9.

6. Hoehn M, Himmelreich U, Kruttwig K, Wiedermann D. Molecular and Cellular MR Imaging: Potentials and Challenges for Neurological Applications. Journal of Magnetic Resonance Imaging. 2008;27(5):941-54.

7. Velde GV, Baekelandt V, Dresselaers T, Himmelreich U. Magnetic Resonance Imaging and Spectroscopy Methods for Molecular Imaging. The Quarterly Journal of Nuclear Medicine and Molecular Imaging. 2009;53(6):565-85.

8. Himmelreich U, Dresselaers T. Cell Labeling and Tracking for Experimental Models Using Magnetic Resonance Imaging. Methods. 2009;48(2):112-24.

9. Louie AY, Hüber MM, Ahrens ET, Rothbächer U, Moats R, Jacobs RE, et al. In Vivo Visualization of Gene Expression Using Magnetic Resonance Imaging. Nature Biotechnology. 2000;18(3):321-5.

10. Cohen B, Dafni H, Meir G, Harmeliny A, Neeman M. Ferritin as an Endogenous MRI Reporter for Noninvasive Imaging of Gene Expression in C6 Glioma Tumors. Neoplasia. 2005;7(2):109-17.

11. Gore JC, Manning HC, Quarles CC, Waddell KW, Yankeelov TE. Magnetic Resonance in the Era of Molecular Imaging of Cancer. Magnetic Resonance Imaging. 2011;29(5):587-600.

12. Moser E, Stadlbauer A, Windischberger C, Quick HH, Ladd ME. Magnetic Resonance Imaging Methodology. European Journal of Nuclear Medicine and Molecular Imaging. 2009;36(Supplement 1):S30-S41.

13. Haacke EM, Brown RW, Thompson MR, Venkatesan R. Magnetic Resonance Imaging: Physical Principles and Sequence Design. New York: John Wiley & Sons; 1999. 914 p.

14. Hornak JP. The Basics of MRI [Online hypertextbook]. Henietta, NY: Interactive Learning Software; 1996-2013 [cited 2013 December]. Available from: http://www.cis.rit.edu/htbooks/mri/.

15. Higgins DM. ReviseMRI.com: RF pulses 2003-2014 [cited 2014 January]. Available from: http://www.revisemri.com/questions/creating_an_image/rf_pulse.

16. Hoult DI. The Origins and Present Status of the Radio Wave Controversy in NMR. Concepts Magn Reson Part A. 2009;34A(4):193-216.

17. Hoult DI, Bhakar B. NMR signal reception: Virtual photons and coherent spontaneous emission. Concepts in Magnetic Resonance. 1997;9(5):277-97.

18. Bradley WG. Fundamentals of MRI: Part I 2001 [cited 2013 December]. Available from: http://e-edcredits.com/xraycredits/article.asp?TestID=1.

19. Hesselink JR. Basic Principles of MR Imaging n.d. [cited 2013 December]. Available from: http://spinwarp.ucsd.edu/neuroweb/Text/br-100.htm#anchor174623.

20. Miles JS, Wolf CR. Principles of DNA Cloning. British Medical Journal. 1989;299(6706):1019-22.

21. Mason MM. A comparison of the maximal growth rates of various bacteria under optimal conditions. Journal of Bacteriology. 1935;29(2):103-10.

22. The MJ. Human Insulin - DNA Technology's 1st Drug. American Journal of Hospital Pharmacy. 1989;46(11):S9-S11.

23. Anderson JC, Clarke EJ, Arkin AP, Voigt CA. Environmentally controlled invasion of cancer cells by engineered bacteria. Journal of Molecular Biology. 2006;355(4):619-27.

24. Kamle S, Ali S. Genetically modified crops: Detection strategies and biosafety issues. Gene. 2013;522(2):123-32.

25. Billinton N, Knight AW. Seeing the wood through the trees: A review of techniques for distinguishing green fluorescent protein from endogenous autofluorescence. Analytical Biochemistry. 2001;291(2):175-97.

26. Welch M, Villalobos A, Gustafsson C, Minshull J. You're one in a googol: optimizing genes for protein expression. Journal of the Royal Society Interface. 2009;6.

27. Cheng AA, Lu TK. Synthetic Biology: An Emerging Engineering Discipline. In: Yarmush ML, editor. Annual Review of Biomedical Engineering, Vol 142012. p. 155-78.

28. Alberts B, Johnson A, Lewis J, Raff M, Roberts K, Walter P. How Genetic Switches Work. Molecular Biology of the Cell. 4 ed. New York: Garland Science; 2002. p. 395-435.

29. Blakemore R. Magnetotactic Bacteria. Science. 1975;190(4212):377-9.

30. Blakemore R. Magnetotactic Bacteria. Annual Review of Microbiology. 1982;36:217-38.

31. Faivre D, Schüler D. Magnetotactic Bacteria and Magnetosomes. Chemical Reviews. 2008;108(11):4875-98.

32. Gorby YA, Beveridge TJ, Blakemore RP. Characterization of the Bacterial Magnetosome Membrane. Journal of Bacteriology. 1988;170(2):834-41.

33. Matsunaga T, Nakamura C, Burgess JG, Sode K. Gene Transfer in Magnetic Bacteria: Transposon Mutagenesis and Cloning of Genomic DNA Fragments Required for Magnetosome Synthesis. Journal of Bacteriology. 1992;174(9):2748-53.

34. Nakamura C, Burgess JG, Sode K, Matsunaga T. An Iron-regulated Gene, MagA, Encoding an Iron Transport Protein of Magnetospirillum sp. Strain AMB-1. The Journal of Biological Chemistry. 1995;270(47):28392-6.

35. Nakamura C, Kikuchi T, Burgess JG, Matsunaga T. Iron-Regulated Expression and Membrane Localization of the MagA Protein in Magnetospirillum Sp. Strain AMB-1. The Journal of Biochemistry. 1995;118(1):23-7.

36. Tanaka M, Okamura Y, Arakaki A, Tanaka T, Takeyama H, Matsunaga T. Origin of Magnetosome Membrane: Proteomic Analysis of Magnetosome Membrane and Comparison with Cytoplasmic Membrane. Proteomics. 2006;6(19):5234–47.

37. René Uebe, and VH, Schüler D. The MagA Protein of Magnetospirilla Is Not Involved in Bacterial Magnetite Biomineralization. Journal of Bacteriology. 2012;194(5):1018-23.

38. Richter M, Kube M, Bazylinski DA, Lombardot T, Glöckner FO, Reinhardt R, et al. Comparative Genome Analysis of Four Magnetotactic Bacteria Reveals a Complex Set of Group-Specific Genes Implicated in Magnetosome Biomineralization and Function. Journal of Bacteriology. 2007;189(13):4899-910.

39. Arakaki A, Webb J, Matsunaga T. A Novel Protein Tightly Bound to Bacterial Magnetic Particles in Magnetospirillum magneticum Strain AMB-1. The Journal of Biological Chemistry. 2003;278(10):8745-50.

40. Prozorov T, Mallapragada SK, Narasimhan B, Wang L, Palo P, Nilsen-Hamilton M, et al. Protein-Mediated Synthesis of Uniform Superparamagnetic Magnetite Nanocrystals. Advanced Functional Materials. 2007;17(6):951-7.

41. Tanaka M, Mazuyama E, Arakaki A, Matsunaga T. MMS6 Protein Regulates Crystal Morphology During Nano-Sized Magnetite Biomineralization In Vivo. The Journal of Biological Chemistry 2011;286(8):6386–92.

42. McGowan JC. Basic Principles of Magnetic Resonance Imaging. Neuroimaging Clinics of North America. 2008;18(4):623–36.

43. Gibby WA. Basic Principles of Magnetic Resonance Imaging. Neurosurgery Clinics of North America. 2005;16(1):1-64.

44. Invitrogen. pBudCE4.1 User Manual. July 7, 2010.

45. Felgner PL, Gadek TR, Holm M, Roman R, Chan HW, Wenz M, et al. Lipofection: A Highly Efficient, Lipid-Mediated DNA-Transfection Procedure. Proceedings of the National Academy of Sciences of the United States of America. 1987;84(21):7413-7.

46. Felgner JH, Kumar R, Sridhar CN, Wheeler CJ, Tsai YJ, Border R, et al. Enhanced Gene Delivery and Mechanism Studies with a Novel Series of Cationic Lipid Formulations. Journal of Biological Chemistry. 1994;269(4):2550-61.

47. Friend DS, Papahadjopoulos D, Debs RJ. Endocytosis and Intracellular Processing Accompanying Transfection Mediated by Cationic Liposomes. Biochimica et Biophysica Acta. 1996;1278(1):41-50.

48. Alberts B, Johnson A, Lewis J, Raff M, Roberts K, Walter P. The Global Structure of Chromosomes. Molecular Biology of the Cell. 4 ed. New York: Garland Science; 2002. p. 216-33.

49. Zurkiya O, Chan AWS, Hu X. MagA is Sufficient for Producing Magnetic Nanoparticles in Mammalian Cells, Making it an MRI Reporter. Magnetic Resonance in Medicine. 2008;59(6):1225-31.

50. Matsunaga T, Okamura Y, Fukuda Y, Wahyudi AT, Murase Y, Takeyama H. Complete Genome Sequence of the Facultative Anaerobic Magnetotactic Bacterium Magnetospirillum sp. strain AMB-1 DNA Research. 2005;12(3):157-66.

51. Papanikolaou G, Pantopoulos K. Iron Metabolism and Toxicity. Toxicology and Applied Pharmacology. 2005;202(2):199-211.

52. Goldhawk DE, Lemaire C, McCreary CR, McGirr R, Dhanvantari S, Thompson RT, et al. Magnetic Resonance Imaging of Cells Overexpressing MagA, an Endogenous Contrast Agent for Live Cell Imaging. Molecular Imaging. 2009;8(3):129-39.

53. Maitra A, Arking DE, Shivapurkar N, Ikeda M, Stastny V, Kassauei K, et al. Genomic Alterations in Cultured Human Embryonic Stem Cells. Nature Genetics. 2005;37(10):1099-103.

54. Petrovick MS, Nargi FE, Towle T, Hogan K, Bohane M, Wright DJ. Improving the Long-Term Storage of a Mammalian Biosensor Cell Line Via Genetic Engineering. Biotechnology and Bioengineering. 2010;106(3):474-81.

55. Hanson C, Caisander G. Human Embryonic Stem Cells and Chromosome Stability. APMIS. 2005;113(11-12):751-5.

56. Lichtenberg U, Zock C, Doerfler W. Integration of Foreign DNA into Mammalian Genome can be Associated with Hypomethylation at Site of Insertion. Virus Research. 1988;11(4):335-42.

57. Voigt K, Izsvák Z, Ivics Z. Targeted Gene Insertion for Molecular Medicine. Journal of Molecular Medicine. 2008;86(11):1205-19.

58. Vasquez KM, Marburger K, Intody Z, Wilson JH. Manipulating the Mammalian Genome by Homologous Recombination. Proceedings of the National Academy of Sciences of the United States of America. 2001;98(15):8403-10.

59. Emery DW. The Use of Chromatin Insulators to Improve the Expression and Safety of Integrating Gene Transfer Vectors. Human Gene Therapy. 2011;22(6):761-74.

60. Emerit J, Beaumont C, Trivin F. Iron Metabolism, Free Radicals, and Oxidative Injury. Biomedicine & Pharmacotherapy. 2001;56(6):333-9.

61. Stathopoulos A, Samuelson C, Milbouw G, Hermanne JP, Schijns V, Chen TC. Therapeutic vaccination against malignant gliomas based on allorecognition and syngeneic tumor antigens: Proof of principle in two strains of rat. Vaccine. 2008;26(14):1764-72.

62. Molecular Imaging with Reporter Genes. Cambridge: Cambridge University Press; 2010.

63. Laurent S, Boutry S, Mahieu I, Elst LV, Muller RN. Iron Oxide Based MR Contrast Agents: from Chemistry to Cell Labeling. Current Medicinal Chemistry. 2009;16(35):4712-27.

64. Chetty KN, Fantroy L, Landau G, Ivie GW. Lack of Dietary Calcium Effect on Chlordecone Increased White Blood Cell Count, Total Iron, and Iron-Binding Capacity in Serum of Rat. Ecotoxicology and Environmental Safety. 1996;33(3):268-70.

65. Elseweidy MM, El-Baky AEA. Effect of Dietary Iron Overload in Rat Brain-Oxidative Stress, Neurotransmitter Level and Serum Metal Ion in Relation to Neurogenerative Disorders. Indian Journal of Experimental Biology. 2008;46(12):855-8.

66. Smith S, Hafer LJ. Education Guide: Special Stains and H & E. Carpinteria, California: Dako North America; 2012.

67. Boss CB, Fredeen KJ. Concepts, Instrumentation and Techniques in Inductively Coupled Plasma Optical Emission Spectrometry: Perkin Elmer; 1997.

68. Hou X, Jones BT. Inductively Coupled Plasma - Optical Emission Spectrometry. In: Meyers RA, editor. Encyclopedia of Analytical Chemistry. Chichester: John Wiley & Sons Ltd.; 2008. p. 1-21.

69. Reimer L, Kohl H. Transmission Electron Microscopy: Physics of Image Formation. New York: Springer Series + Business Media, LLC; 2008.

70. Stoddart MJ. Cell Viability Assays: Introduction. 2011. In: Mammalian Cell Viability: Methods and Protocols [Internet]. Springer Science+Business Media, LLCMethods in Molecular Biology; [1-6].

71. Longo-Sorbello GSA, Sayam G, Banerjee D, Bertino JR. Cytotoxicity and Cell Growth Assays. 2006. In: Cell Biology: A Laboratory Handbook [Internet]. U.S.A.: Elsevier Science. 3. [315-24].

72. Meerloo Jv, Kaspers GJL, Cloos J. Cell Sensitivity Assays: The MTT Assay. 2011. In: Cancer Cell Culture: Methods and Protocols [Internet]. Science+Business Media, LLC. 2. Methods in Molecular Biology; [237-45].

73. Weizsaecker M, Deen DF, Rosenblum ML, Hoshino T, Gutin PH, Barker M. The 9L Rat Brain Tumor: Description and Application of an Animal Model. Journal of Neurology. 1981;224(3):183-92.

74. Brown KE, Mathahs MM, Broadhurst KA, Weydert J. Chronic iron overload stimulates hepatocyte proliferation and cyclin D1 expression in rodent liver. Translational Research. 2006;148(2):55-62.

75. Brown KE, Broadhurst KA, Mathahs MM, Weydert J. Differential expression of stress-inducible proteins in chronic hepatic iron overload. Toxicology and Applied Pharmacology. 2007;223(2):180-6.

76. Andreu GLP, Inada NM, Vercesi AE, Curti C. Uncoupling and oxidative stress in liver mitochondria isolated from rats with acute iron overload. Archives of Toxicology. 2009;83(1):47-53.

77. Pelot D, Zhou XJ, Carpenter P, Vaziri ND. Effects of experimental hemosiderosis on pancreatic tissue iron content and structure. Digestive Diseases and Sciences. 1998;43(11):2411-4.

78. Zhou XJ, Laszik Z, Wang XQ, Silva FG, Vaziri ND. Association of renal injury with increased oxygen free radical activity and altered nitric oxide metabolism in chronic experimental hemosiderosis. Laboratory Investigation. 2000;80(12):1905-14.

79. Zhou XJ, Vaziri ND, Pandian D, Wang ZQ, Mazowiecki M, Liao SY, et al. Urinary concentrating defect in experimental hemochromatosis. Journal of the American Society of Nephrology. 1996;7(1):128 -34.

80. Cardoso LM, Pedrosa ML, Silva ME, Moraes MFD, Colombari E, Chianca-Jr. DA. Baroreflex function in conscious rats submitted to iron overload. Brazilian Journal of Medical and Biological Research 2005;38(2):205-14.

81. Tipnis UR, He G-Y, Khan MF. Differential induction of polyamine oxidase activity in liver and heart of iron-overloaded rats. Journal of Toxicology and Environmental Health 1997;51(3):235 -44.

82. Shapiro EM, Skrtic S, Koretsky AP. Sizing It Up: Cellular MRI Using Micron-Sized Iron Oxide Particles. Magnetic Resonance in Medicine. 2005;53(2):329-38.

83. Walker-Samuel S, Burrell J, Ramasawmy R, Johnson P, Wells J, Siow B, et al., editors. Imaging the Relationship Between Tumour Interstitial Fluid Velocity and Microvascular Perfusion with Convection MRI. International Society for Magnetic Resonance in Medicine 20th Annual Meeting and Exhibition; 2012; Melbourne, Australia.

84. Benjaminsen IC, Graff BA, Brurberg KG, Rofstad EK. Assessment of Tumor Blood Perfusion by High-Resolution Dynamic Contrast-Enhanced MRI: A Preclinical Study of Human Melanoma Xenografts. Magnetic Resonance in Medicine. 2004;52(2):269-76.

85. Graff B, Kvinnsland Y, Skretting A, Rofstad E. Intratumour Heterogeneity in the Uptake of Macromolecular Therapeutic Agents in Human Melanoma Xenografts. British Journal of Cancer. 2003;88(2):291-7.

86. Alfke H, Stöppler H, Nocken F, Heverhagen JT, Kleb B, Czubayko F, et al. In Vitro MR Imaging of Regulated Gene Expression. Radiology. 2003;228(2):488-92.

87. Weissleder R, Simonova M, Bogdanova A, Bredow S, Enochs WS, Bogdanov A. MR Imaging and Scintigraphy of Gene Expression Through Melanin Induction. Radiology. 1997;204(2):425-9.

88. Genove G, DeMarco U, Xu H, Goins WF, Ahrens ET. A New Transgene Reporter for In Vivo Magnetic Resonance Imaging. Nature Medicine. 2005;11(4):450-4.

89. Alberts B, Johnson A, Lewis J, Raff M, Roberts K, Walter P. Manipulating Proteins, DNA, and RNA. Molecular Biology of the Cell. 4 ed. New York: Garland Science; 2002. p. 469-546.

90. Weissleder R, Pittet MJ. Imaging in the Era of Molecular Oncology. Nature. 2008;452(7187):580-9.